PL-TR-94-2017

AD-A276 729

‖‖‖‖‖‖‖‖‖‖‖‖‖‖‖‖‖

# REGIONAL SEISMIC STUDIES
IN CENTRAL ASIA

Keith Priestley

University of Nevada, Reno
Seismology Laboratory
Reno, NV 98557

DTIC
ELECTE
S FEB 24 1994 **D**
B

17 January 1994
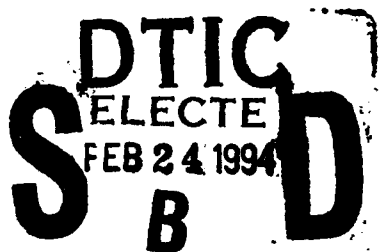
Final Report
10 August 1990-15 August 1993

94-06028

‖‖‖‖‖‖‖‖‖‖‖‖‖‖‖‖‖

DTIC QUALITY INSPECTED 2

94 2 23 265

Best Available Copy

The views and conclusions contained in this document are those of the authors and should not be interpreted as representing the official policies, either express or implied, of the Air Force or the U.S. Government.

This technical report has been reviewed and is approved for publication.
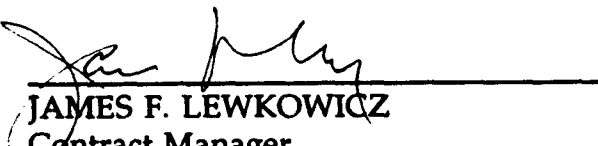
JAMES F. LEWKOWICZ
Contract Manager
Solid Earth Geophysics Branch
Earth Sciences Division
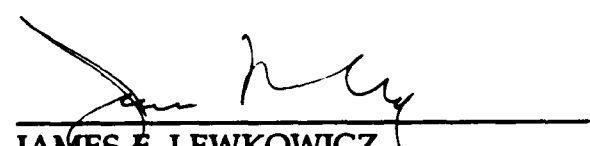
JAMES F. LEWKOWICZ
Branch Chief
Solid Earth Geophysics Branch
Earth Sciences Division
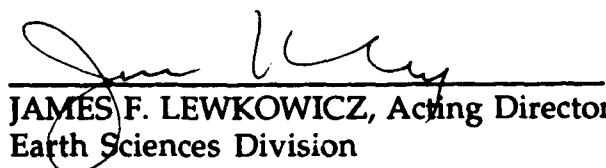
JAMES F. LEWKOWICZ, Acting Director
Earth Sciences Division

REPORT DOCUMENTATION PAGE

1. AGENCY USE ONLY (Leave blank)	2. REPORT DATE	3. REPORT TYPE AND DATES COVERED
	January 17, 1994	Final (10 Aug 1990 – 15 Aug 1993)

4. TITLE AND SUBTITLE

Regional Seismic Studies in Central Asia

5. FUNDING NUMBERS

PE 62101F
PR 7600   TA 09   WU AX

Contract F19628-90-K-0046

6. AUTHOR(S)

Keith Priestley

7. PERFORMING ORGANIZATION NAME(S) AND ADDRESS(ES)

University of Nevada, Reno
Seismology Laboratory
Reno, NV 89557

8. PERFORMING ORGANIZATION REPORT NUMBER

9. SPONSORING/MONITORING AGENCY NAME(S) AND ADDRESS(ES)

Phillips Laboratory
29 Randolph Road
Hanscom AFB, MA 01731-3010

Contract Manager: James Lewkowicz/GPEH

10. SPONSORING/MONITORING AGENCY REPORT NUMBER

PL-TR-94-2017

11. SUPPLEMENTARY NOTES

12a. DISTRIBUTION/AVAILABILITY STATEMENT

Approved for public release; distribution unlimited

12b. DISTRIBUTION CODE

13. ABSTRACT (Maximum 200 words)

This report describes two related research efforts performed under contract F19628-90-K-0046. Section A discusses strike-slip faulting within the Zagros Mountains of Iran. Mechanisms for six earthquakes along the Kazerun line show right-lateral strike-slip motion within this compressional environment, indicating the line is the surface expression of a buried strike-slip fault. Slip vectors in these earthquakes are different from neighbouring reverse-faulting earthquakes suggesting that the Kazerun line accommodates some of the shortening between Arabia and central Iran by an elongation of the Zagros parellel to strike. Section B presents a new velocity model for the continental upper mantle beneath central Siberia based on observations of the 1982 "Rift" DSS profile. The major features of the model are: (1) a sharp increase in velocity gradient between 210 and 235 km depth; (2) a broad high-gradient zone from 400 to 435 km depth; and (3) a narrow high-gradient zone between 655 and 659 km depth.

14. SUBJECT TERMS		15. NUMBER OF PAGES
Zagros Mts. Upper mantle velocity		78
Iran central Siberia		**16. PRICE CODE**
Deep seismic sounding		

17. SECURITY CLASSIFICATION OF REPORT	18. SECURITY CLASSIFICATION OF THIS PAGE	19. SECURITY CLASSIFICATION OF ABSTRACT	20. LIMITATION OF ABSTRACT
Unclassified	Unclassified	Unclassified	SAR

iii

Accession For	
NTIS GRA&I	☑
DTIC TAB	☐
Unannounced	☐
Justification	
By	
Distribution/	
Availability Codes	
Dist	Avail and/or Special
A-1	

EARTHQUAKES ON THE KAZERUN LINE IN THE ZAGROS MOUNTAINS OF IRAN: STRIKE-SLIP FAULTING WITHIN A FOLD-AND-THRUST BELT

Calum Baker, James Jackson and Keith Priestley.

Bullard Laboratories, Madingley Rise, Cambridge, CB3 0EZ

1. Introduction

Convergence between continental plates often leads to the formation of fold-and-thrust belts. Of the many such belts that are forming today, the Zagros mountains of SW Iran is one of the simplest and most seismically active. Its formation is related to the convergence between the Arabian plate in the SW and the central plateau of Iran to the NE. At the surface, the Zagros consists of long, linear anticlinal ridges that form a series of ranges from eastern Turkey in the NW to the Strait of Hormuz in the SE, a distance of about 1200 km. The width of the belt is 200–300 km. Most of the larger earthquakes in the Zagros have fault plane solutions that involve high-angle reverse faulting on planes that strike parallel to the local trend of the fold axes at the surface. In this respect, the deformation of the Zagros mountains is approximately two-dimensional, involving predominantly shortening perpendicular to strike and crustal thickening (e.g. Jackson & McKenzie 1984).

The anticlinal ridges that dominate the morphology of the Zagros are not continuous for the entire length of the belt. They are typically no longer than 100 km, and die out along strike at each end. There are several places where the ends of the anticlinal axes apparently line up, to produce sinuous valleys that are oblique to the strike of the belt, and across which the anticline axes are not continuous. The best known of these is the Kazerun Line (or Flexure), in the central Zagros (Plate 1; Figs. 1 and 2), which is the subject of this paper. At its northern end it is a clear fault which can be mapped on the surface and is usually referred to as the Kazerun Fault (Manuel Berberian, *pers. comm.*). The Kazerun Line crosses the Zagros with a N-S trend, which is common also in the structures of Oman on the SW side of the Persian Gulf (Falcon 1969; Stöcklin 1974; Haynes & McQuillan 1974). Fold axes do not cross the Kazerun Line, and are generally thought to be offset in a right-lateral sense, partly because that is to be expected on a structure that is oblique in this way to the NE SW direction of shortening (Falcon 1969; Haynes & McQuillan 1974, Colmann-Sadd 1978). The Kazerun Line seems to have influenced sedimentation in the Zagros since at least the Middle Jurassic (Koop & Stoneley 1982), which suggests that it may be related to a basement structure. Basement faults of proterozoic age in Arabia have a similar trend and are important in controlling the geometry of the hydrocarbon structures found there.

Structures that are transverse or oblique to the strike of fold-and-thrust belts, and which offset the fold axes, are not especially rare. Dahlstrom (1970) and Boyer & Elliott (1982) describe transverse structures in the Appalachians and Canadian Rocky Mountains that are interpreted as lateral ramps on thrust faults which are contained within the deforming sedimentary cover. The deformation (which is no longer active) in these cases is thought to be 'thin-skinned', and does not involve the shortening of the basement beneath the sedimentary cover. In the Tien Shan mountains of central Asia, large strike-slip faults cross the range at an oblique angle to the strike. The strike-slip faults there are active today. They are visible at the surface and in satellite images, clearly truncating and offsetting fold axes, and several have moved in strike-slip faulting earthquakes this century (Tapponnier & Molnar 1979; Molnar & Deng 1984; Nelson *et al.* 1987). Some of the transverse structures

1

in the Tien Shan cross the entire range, and are clearly basement features. The Lesser Himalaya also contains a number of strike-slip faults oblique to the strike of the belt (Valdiya 1976). These trend NNE and NNW, with a trend similar to the sub-surface ridges and faults seen in the adjacent Indian shield. This similarity suggests that the transverse faults are related to the structural features of the underthrusting Indian Shield (Ni and Barazangi 1984). The seismically active fold-and-thrust belt of NW Greece and Albania contains structures that are similar to the Kazerun Line; they appear as transverse valleys almost perpendicular to regional strike, across which fold axes are not continuous. These have been interpreted as strike-slip faults (I.F.P. 1966), but have had no recent large earthquakes associated with them.

This study was motivated by the occurrence of seven moderate-sized (m_b 5.1–5.7) earthquakes in 1986–90 that occurred on or very near the Kazerun Line in the Zagros. Prior to these earthquakes, there had been almost no seismicity on the Kazerun Line that could be studied by teleseismic methods. In this paper we obtain the source parameters of these and other nearby earthquakes. This information will allow us to address the following questions: *(i)* is the Kazerun Line the surface expression of basement faulting?; *(ii)* is it associated with right-lateral strike-slip faulting, and therefore different from the high-angle reverse faulting nearby?; *(iii)* if so, is the direction of slip on the Kazerun Line different from that of the nearby reverse faults? The answers to these questions will help establish the nature of this transverse feature, and its role in the accommodation of shortening between Arabia and Iran. In particular, the slip vectors near the Kazerun Line should indicate whether it behaves as a transform feature (in which slip vector is preserved), or as a structure that requires movement of material parallel to the strike of the belt, thus modifying earlier views that the deformation of the Zagros is two-dimensional. An understanding of the Kazerun Line may help in the interpretation of similar structures in other fold belts that are either inactive, or have had no recent seismicity that reveals their nature.

2. Geology and seismicity of the Zagros Mountains

The Zagros mountains contain a thick, almost continuous, sequence of shelf sediments from Paleozoic to Late Tertiary age, deposited over the Infra-Cambrian Hormuz Salt Formation, which itself may be a km or more thick (e.g. Ala 1974; Berberian & King 1981). This sequence is distinct from the rocks of central Iran, and is separated from them by a structure called the Zagros Thrust Line (Fig 1. also known as Main Zagros Reverse Fault) that marks the NE boundary of the Zagros (Stöcklin 1968). In the Late Cretaceous, ophiolitic-like rocks were emplaced along the NE margin of the Zagros, indicating that some shortening occurred then (Stoneley 1976). However, most of the width of the Zagros is occupied by what is known as the 'Simple Folded Belt', which contains the thick Paleozoic–Mesozoic–Tertiary shelf deposits that were warped into elongate, open folds in the Miocene onwards (Falcon 1969). There is substantial evidence, summarized by Stöcklin (1968, 1974), Stoneley (1976), Koop & Stoneley (1982) among others, that what is now the Simple Folded Belt of the Zagros was a subsiding passive continental margin on the NE edge of the Arabian shield in the Mesozoic and Tertiary. The sedimentary sequence contains thick evaporite horizons of Infra-Cambrian, Jurassic and Tertiary age that are known to decouple structures above and below them, and make it unlikely that there is any direct correlation between the structures in the basement and those at the surface (Lees 1952; Falcon 1969). The basement itself is not exposed, and is known only from exotic blocks of metamorphic rocks brought to the surface in salt plugs (Haynes & McQuillan 1974). The

2

total thickness of sediments above this basement is not known precisely: it is estimated to be around 8–10 km, but might reach greater thicknesses locally, such as in the Dezful embayment near 32°N 49°E (see Morris 1977, Jackson & Fitch 1981).

The Kazerun Line itself is the most prominent of a number of N–S lineations that cross the Simple Folded Belt (Plate 1; Figs. 1 & 2). It runs north from the Persian Gulf for about 250 km at longitude 51.5°E. A similar feature occurs near Qir, 200 km SE of Kazerun (Fig. 1). Most of these transverse features do not outcrop as discrete strike-slip faults at the surface, though they are sometimes associated with a deflection of nearby structures into the valleys that suggests a right-lateral component of motion on them (e.g. McQuillan 1973). Such deflection can be clearly seen on a *Landsat 4* image of the Kazerun Line (Plate 1). Falcon (1969) suggests that the Arabian shield (of which the Zagros basement is thought to be a part) is divided into a number of blocks by basement faults of this N–S trend.

Earthquakes occur throughout the 200–300 km width of the Zagros mountains, with an abrupt cutoff in the NE, along the Zagros Thrust Line (Fig. 1). However, except in the NW of the belt, most of the larger ($m_b \geq 5.0$) earthquakes in the Zagros occur along its SW front, between the coast of the Persian Gulf and the 1500m topographic contour (Jackson & McKenzie 1984; Ni & Barazangi 1986). Except for smaller earthquakes, the highest elevations of the Zagros, which reach 3,000–4,000m, are relatively aseismic. Most of the larger earthquakes have fault plane solutions that show high-angle (30–60° dip) reverse faulting on planes parallel to the local strike of the belt (see Jackson & McKenzie 1984). These fault plane solutions are based primarily on P wave first motion polarities, and their strikes are thus constrained mostly by polarities at regional stations. In this study we use teleseismic P and SH waveforms to obtain source parameters. SH waveforms are particularly useful for constraining the strike of high-angle reverse fault mechanisms. Only two fault plane solutions are so far available for earthquakes near the Kazerun Line. The first occurred on 23.6.1968 and had first motion polarities at regional stations that suggested a different source orientation from the majority of Zagros earthquakes. The solution published for this event by Jackson & Fitch (1981) involved reverse faulting on a strike parallel to the Kazerun Line. The second event occurred on 6.4.71. First motion readings published by Jackson & McKenzie (1984) allowed either a thrust or strike-slip solution. We will re-examine both events using P and SH waveforms.

Various people have studied the depths of the larger Zagros earthquakes using teleseismic P waveforms (e.g. Jackson & Fitch 1981; Kadinsky-Cade & Barazangi 1982; Ni & Barazangi 1986). The hypocentres are mostly in the range 8–14 km. These depths are obtained from long-period waveforms of the World Wide Standard Seismograph Network (WWSSN) and are thus centroid depths: they represent the finite earthquake source by a point, which is the weighted centre of moment release. Since the earthquakes are of magnitude (M_s) ~6.0, they will have involved motion on faults of around 10 km in dimension. It is therefore safe to assume that the faulting extended to greater depths than the hypocentres and almost certainly into what can be regarded as 'basement' beneath the Hormuz Salt Formation. These studies therefore conclude that the larger earthquakes probably occur on faults in the uppermost basement beneath the sedimentary cover. Such basement faults would be unlikely to propagate to the surface through the several thick evaporite horizons within the sedimentary cover, and this is usually taken as the explanation for the remarkable lack of surface faulting following Zagros earthquakes even as large as M_w 6.7 (e.g. Berberian 1976a, 1977; Berberian & Papastamatiou 1978; Jackson & Fitch 1981; Ambraseys & Melville 1982).

The occurrence of widespread high-angle reverse faulting within the basement led Jackson (1980) to suggest that reverse motion was occurring on reactivated old normal faults

3

that were responsible for the extension and subsidence of the continental margin in the Mesozoic. Such reactivation has since been demonstrated elsewhere (e.g. Stoneley 1982; Badley, Price & Backshall 1989; Roberts 1989; Letouzey 1990), but in the Zagros remains just a plausible speculation and cannot be proved.

In this paper we will use long period teleseismic P and SH waveforms to determine the source parameters of 9 earthquakes that occurred on or near the Kazerun Line. We will also consider the centroid moment tensor (CMT) solutions published by Harvard for 4 events where the data were insufficient for us to model using our technique.

3. Determination of source parameters

We used first motion polarities and P and SH waveforms to constrain the earthquake source parameters. First motions were taken from long period vertical instruments of the WWSSN, and the onset times of these first motions were checked, when possible, with the arrival times recorded on the short period instrument. When the long period instrument was unavailable, we read the polarity on short period instruments only when the onset was recognizable as the instrument response to a delta function, and at an arrival time with a small travel time residual (see Jackson & McKenzie 1984). We did not read first motion polarities from the narrow band instruments of the SRO or ASRO networks, which have too emergent a response for this purpose. The first motions for the events we studied here are shown in Fig. 3.

For P and SH waveform analysis we used McCaffrey & Abers's (1988) version of Nábělek's (1984) inversion procedure, which minimizes, in a least squares sense, the misfit between observed and synthetic seismograms. This procedure is now too routine to justify detailed description. The reader is referred to McCaffrey & Nábělek (1987), Nelson, McCaffrey & Molnar (1987), Fredrich, McCaffrey & Denham (1988) for details. The procedure assumes that the source can be represented as a point (the centroid) in space, but not in time. The time history of displacement on the fault is represented by a source time function made up of a series of overlapping isosceles triangles. The seismograms are formed by the addition of direct P or SH waves with the surface reflections pP, sP and sS and near source multiples. Amplitudes are corrected for geometrical spreading, and for anelastic attenuation using a Futterman (1962) Q operator with a value for t^* of 1.0s for P and 4.0s for SH waves. Uncertainties in t^* lead to uncertainties in source duration and seismic moment, but have only a small effect on centroid depth and source orientation. To avoid upper mantle triplications and interference from core phases, P waveforms are used in the distance range 30–90°, and SH waves in the range 30–75°.

The inversion procedure adjusts the relative amplitudes of the source time function elements, the centroid depth, the seismic moment, and the source orientation (strike, dip, rake) to minimize the misfit between observed and synthetic seismograms. We refer to this solution as the 'minimum misfit solution'. The covariance matrix associated with this solution usually underestimates, sometimes seriously, the true uncertainties associated with the source parameters (see McCaffrey & Nábělek 1987). A better estimate of the real errors is found by fixing some of the source parameters at values close to but different from those of the minimum misfit solution, and seeing whether the match of observed to synthetic seismograms deteriorates (see McCaffrey & Nábělek 1987; Nelson, McCaffrey & Molnar 1987; Fredrich, McCaffrey & Denham 1988; Molnar & Lyon-Caen 1989). We use this procedure to estimate errors here.

Uncertainties in seismic moment and centroid depth arise from errors in the source

velocity model. Realistic velocity models are not known in the Zagros. We therefore tried various different models, within a range that we considered likely, to examine their influence on these parameters. In general, we used a velocity model with an average P velocity of 6.0 km/s above the source and 6.8 km/s below the source. In the next section we will discuss one earthquake in detail to illustrate the procedures we adopted. The other earthquakes are discussed more briefly in the Appendix.

Hypocentral parameters of the earthquakes we studied are listed in Table 1. Their epicentres are plotted in Fig. 1, and are likely to be in error by up to 15 km (Ambraseys 1978; Berberian 1979).

4. The earthquake of 6 December 1988.

This earthquake, of m_b 5.5, is typical of the group of events that occurred near the Kazerun Line between 1986 and 1990 (Fig. 1 and Table 1) in that P amplitudes were small, and in particular, much smaller than SH amplitudes. Very few first motions were large enough to be read on long period WWSSN instruments, and first motions alone are unable to constrain the fault plane solution effectively (Fig. 3): the few compressional polarities that are available are consistent with both right-lateral strike-slip faulting on a N-S fault and with high-angle reverse faulting striking NW-SE.

Observed waveforms for this earthquake are shown in Fig. 4. SH waveforms are well distributed in azimuth and are of large amplitude. P amplitudes are at least a factor of 3 smaller. The minimum misfit solution returned by the inversion procedure is a strike-slip mechanism, consistent with right-lateral faulting on a N-S fault. At first glance, it would appear that the main constraint on this solution is provided by the large and abundant SH waveforms, rather than the P waveforms. The observed SH waveforms are obviously well matched by the minimum misfit solution. However, the SH radiation pattern, whose nodal planes are arranged in cross oriented NE-SW and NW-SE, is consistent with either N-S right-lateral strike-slip faulting (as in Fig. 4) or with high-angle reverse faulting striking NW-SE. Both mechanisms are also allowed by first motion polarities (Fig. 3), and these are the two possibilities that are most likely and which we wish to distinguish. (Recall that previous authors had inferred a N-S right-lateral strike-slip nature to the Kazerun Line, and that most of the existing fault plane solutions in the Zagros show reverse faulting with a NW-SE strike.) We must therefore address whether the waveform data are able to distinguish these two mechanisms.

In Fig. 5 we compare selected P and SH waveforms of our minimum misfit solution (top line), with those for an inversion (bottom line) in which the fault orientation was that of a reverse fault striking NW-SE with an SH radiation pattern similar to that of the minimum misfit solution. To obtain the solution in line C we computed the thrust solution with the same SH radiation pattern as the strike-slip fault in line A and used this as the starting point for the inversion. We then allowed all parameters to vary in the inversion. Unlike the minimum misfit solution in the top line, the solution in the bottom line is unable to fit the amplitudes of both the P and SH waveforms simultaneously. The P amplitudes predicted by the reverse fault mechanism are much too large relative to the SH amplitudes. The reason for this is clear: in the strike-slip solution (top line) the station positions on the focal sphere are all close to the nodal planes of the P radiation pattern, and are consequently of small amplitude. For the reverse fault solution, these stations are in the middle of the compressional P quadrant, and have much larger amplitude. In other words, the smallness of the P waveforms is in itself important information, which is consistent with

the strike-slip but not with the reverse fault solution.

A centroid moment tensor (CMT) solution, obtained by Harvard University, was also published for this event in the Preliminary Determination of Epicentres (PDE) issued by the USGS. The orientation of the CMT solution differs only by 20° in rake from that of our minimum misfit solution. In the middle line of Fig. 5 we show the waveforms for an inversion in which the strike, dip and rake were held at the values given by the CMT solution, and only the source time function, centroid depth and moment were allowed to be free. The synthetic waveforms in the top and middle lines are little different; the fit to some of the observed seismograms at stations marked by arrows in the middle row is perhaps marginally worse than in the top row. This procedure illustrates how we estimate uncertainties in source orientation. For example, to examine rake, we would fix the rake at a value different from that of the minimum misfit solution and allow all other parameters to be free in the inversion. If the resultant fit of observed and synthetic seismograms was significantly poorer than the fit for the minimum misfit solution, we would conclude that the value of rake chosen was outside the acceptable range. In this way we estimated the uncertainties for this earthquake to be ±10° in strike, -10/+5° in dip, ±15° in rake, and ±2 km in depth.

We also investigated the effect of a likely range of source velocity models on the inversion. Fig. 6 shows selected waveforms at a number of stations for inversions carried out in the different velocity models listed in Table 2. The fit of synthetic and observed waveforms is barely different in each case. The source orientations are only a few degrees different from that of the minimum misfit solution (row D): differences that are anyway less than the uncertainty we estimated for each of these parameters. The main effect of changing velocity structure is to change centroid depth, by up to 3 km in this case, and seismic moment, by up to 20%. Small changes are also observed in the source time function. Thus we are confident that reasonable changes to the source velocity structure will not affect our estimate of the source orientation (the principal interest of this paper) to a greater extent than the errors we would anyway estimate from our other tests.

We investigated eight other earthquakes in the manner outlined for this event. Each one is discussed is the Appendix. In particular, the observation that the P waveforms were much smaller in amplitude than the SH waveforms (as discussed in Fig. 4) was an important indication that several of the earthquakes had strike-slip mechanisms.

5. Results

From an analysis of long period P and SH body waves we were able to estimate source parameters, and their uncertainties, for nine earthquakes in the vicinity of the Kazerun Line. The fault plane solutions for these earthquakes are shown in Fig. 7. We also include in Fig. 7 the fault plane solutions for four additional earthquakes, for which Harvard CMT solutions are available, but whose body waves were too small for us to analyse by the technique illustrated above. The source parameters for these earthquakes are listed in Table 3.

6. Discussion

Of the nine earthquakes whose body waveforms we analysed, the five whose epicentres lie close to the Kazerun Line (events F, G, H, I, K) all have strike-slip mechanisms (Fig. 7) and lie within a small area. The fact that the ISC locations appear to form a line perpendicular to the trend of the Kazerun Line is not significant. The probable errors in the locations of these

epicentres are in the region of 15 km (Ambraseys 1978; Berberian 1979), and thus they could all have occurred on the Kazerun Line itself. The Kazerun Line is visible as a N-S striking fault on the surface in the vicinity of these events and although none of these earthquakes were associated with a surface break the fault shows evidence of past right-lateral motion. Each of the fault plane solutions for these five earthquakes contains a nodal plane that is parallel to the Kazerun Line in their epicentral regions, and if these nodal planes were the fault planes, the sense of motion on each would be right-lateral strike-slip . This has always been inferred, from geological evidence, to be the sense of motion associated with the Kazerun Line and other similar structures that cross the Zagros (e.g. Stöcklin 1968; Falcon 1969, McQuillan 1973). Furthermore the known macroseismic areas for these events lie on the line of the fault and are orientated N-S (see appendix, event F). Such macroseismic locations are likely to be more accurate than the instrumental locations for earthquakes of this size. We therefore conclude that the Kazerun Line and the Kazerun Fault trace represent the surface expression of a buried right-lateral strike-slip fault with a N-S strike (the average strike of the N-S nodal planes in events F,G,H,I,K is $356 \pm 9°$).

Our modelling suggests that event B (6.4.71) also has a strike-slip solution. This is discussed further in the appendix. The ISC location for this event was around 30 km southeast of the cluster of strike-slip events at the northern end of the Kazerun Line and about 50 km NW of the northern end of the Karehbas Fault, a NW striking transverse feature with no earthquakes in recent times. Using a master event technique (Jackson & Fitch, 1979) we relocated this event relative to one of those occurring in this cluster. We used 881206 (event K) as the master as this had the largest number of reporting stations in the ISC bulletin for the events studied. The result indicated that event B really was about 25 km SE of the main cluster of events on the Kazerun Line.

The centroid depths of the five earthquakes on the Kazerun Line vary from 4 to 10 km with typical uncertainties of ± 3 km. These depths are those of the conceptual point sources that represent the weighted average position of seismic moment release. To a first approximation we can think of them as points in the centre of the fault planes that moved in each earthquake. These earthquakes were not large, the biggest being only M_w 5.8. We can estimate the approximate size of the fault planes in the following way. The seismic moment, M_0, is given by $M_0 = \mu A u$, where μ is the rigidity ($\sim 3 \times 10^{10} \, \text{Nm}^{-2}$), A is the fault area, and u is the average displacement. Let us assume that the fault is roughly circular in area with diameter L, and that the ratio u/L is $\sim 5 \times 10^{-5}$ (see e.g. Scholz et al. 1986). For a seismic moment of 5×10^{17} Nm (Table 3), we would then calculate L to be 8 km. In other words, since the faults are sub-vertical rupture in earthquakes of this size would extend about 4 km beneath the centroid depth. The depth to the basement in this area, by which we mean the crystalline metamorphic rocks beneath the overlying sedimentary cover, is not well known. Morris (1977) estimates the depth to magnetic 'basement', based on aeromagnetic surveys, to be about 8 km. We believe it likely that these earthquakes on the Kazerun Line involved faulting in the basement for two reasons: *(i)* the centroid depths and source dimensions of the earthquakes make faulting at basement depths probable (to the extent that basement depths are known), and *(ii)* we do not believe that faults with dimensions of 8 km can be contained within a sedimentary column of comparable thickness that contains at least three separate and thick evaporite sequences (at infra-Cambrian, Jurassic and Miocene levels) without involving surface rupture. In other words, if the faults are required to cut through the evaporite horizons to achieve the area necessary for their seismic moment, why do they not also cut through to the surface, as earthquakes of similar size do elsewhere in Iran (see e.g. Ambraseys & Melville 1982)? We think it more probable that the earthquake faulting

is predominantly beneath the Hormuz Salt, whose ductility prevents rupture reaching the surface. The Kazerun Line then represents the surface distortion of the folded, deformed sedimentary cover that is decoupled from the motions in the basement.

What is then the significance of the Kazerun Line in the deformation of the Zagros, which must accommodate the convergence between Arabia and central Iran? In Fig. 8 we show the horizontal projections of the slip vectors for the earthquakes in Fig. 7. For the strike-slip earthquakes we studied on the Kazerun Line (F,G,H,I,K) and for events J and L, for which there is only a Harvard CMT solution, we chose the N-S nodal planes as the fault planes. The average slip vector azimuth for events F,G,H,I,K is $354 \pm 5°$. If we also consider event B in this group then the average slip vector azimuth is $350°$. For the three earthquakes we studied that involved high-angle reverse faulting (A,C,D), we cannot identify the probable fault plane: however they are all nearly pure reverse faults, and the two possible slip vectors in each earthquake do not differ by more than $16°$. The average azimuth of all 6 slip vectors for these earthquakes (two per event) is $036 \pm 22°$. The dispersion of the slip vectors in these reverse faulting events is partly related to the curvature of the arc made by the southern Zagros in this region: the anticlines in the NW of Figs. 2 and 7 trend $\sim165°$, whereas in the SE, near event C, the anticlines trend $\sim140°$. Thus events A,C and D involved faulting with a strike roughly parallel to the local trend of the anticlines. The two thrusts for which CMT solutions are available (events E & M) also follow this pattern.

Thus the strike-slip faulting on the Kazerun Line involves slip that is in a different direction from that associated with the reverse faulting and folding. There are two possible explanations for this discrepancy. The first is that the overall motion accommodated by the Kazerun Line is the same as that accommodated by the reverse faults, but that the Kazerun Line rotates about a vertical axis as it moves. This style of deformation is known from elsewhere, such as in Greece (e.g. McKenzie & Jackson 1986; Taymaz et al. 1991), but usually involves domains of several rotating sub-parallel faults. The Kazerun Line seems isolated, and also surrounded by reverse faults (e.g. events A,E and M). There may be other more subdued transverse structures in the Zagros (Berberian, 1976b), but none are as prominent as the Kazerun Line. We do not think this rotational explanation for the slip vector directions on the Kazerun Line is likely. The only other major transverse lineation in the Zagros which appears to be active is the Oman Line. This lies 700 km to the SE at the eastern end of the Zagros fold belt and marks an abrupt change in the pattern of seismicity, seperating the fold belt from the Makran subduction zone. It is characterised by thrust faulting and is thought to represent the underthrusting of the Arabian shelf beneath Iran or the indentation of Arabia as a promontory (Kadinsky-Cade & Barazangi 1982).

A second explanation for the discrepant slip direction on the Kazerun Line is that it takes up shortening perpendicular to the strike of the Zagros by a component of extension parallel to the strike of the belt, rather than by crustal thickening. This style of deformation is also known elsewhere, such as in eastern Turkey (e.g. McKenzie 1972) and in central Asia (e.g. Tapponnier & Molnar 1979). In Fig. 9 we show the P and T axes of the earthquakes in Fig. 7. For the earthquakes we studied, the azimuths of the P axes for the reverse faults (3 events, average $36 \pm 21°$) and the strike-slip faults (5 events, average $36 \pm 7°$) are the same. The average P axis azimuth for all nine earthquakes is $36 \pm 15°$, which is almost perpendicular to the average strike of the anticlines ($140-165°$). The T axes for the strike-slip events are sub-parallel to the strike of the fold belt. These observations, and the fact that the Kazerun Line appears as a structure on its own rather than as one of a series of parallel faults, suggests to us that this second explanation is the more likely of

8

the two. The strike-slip motion on the Kazerun Line implies that there is movement of material along strike of the Zagros, and that the deformation in this mountain belt is not strictly two-dimensional. It is not easy to assess the likely rate of elongation parallel to the strike of the Zagros that is caused by the Kazerun Line and similar structures. It is clear from the anticlines and reverse faulting earthquakes near the Kazerun Line that it does not accommodate all the shortening at its position within the belt. Regional elevations near the Kazerun Line are not noticeably different from those elsewhere in the Simple Folded Belt. These observations, combined with the modest level of recent and historical seismicity (Ambraseys & Melville 1982), suggest to us that the rate of motion on the Kazerun Line is relatively slow.

At the surface the Kazerun Line appears as an oblique interruption to the otherwise regular series of anticline ridges. The earthquakes we have studied demonstrate that this feature is not merely an instability in the folding of the sediments, but is the surface expression of a buried right-lateral strike-slip fault. Could this fault simply be a lateral ramp on one or a series of thrust faults, as envisaged in, for example, the Canadian Rockies or the Appalachians (e.g. Harris 1970; Dahlstrom 1970; Boyer & Elliott 1982)? We do not think the Kazerun Line (or fault) is such a lateral ramp, for two reasons: *(i)* the slip vectors on the Kazerun Line are different from those of the reverse faults, and *(ii)* the reverse faults that occur in the Zagros have, almost without exception, relatively steep dips in the range 30–60°. Moreover, the reverse faults are active across a considerable width of the range (Jackson & McKenzie 1984). We do not doubt that there is a decoupling between the metamorphic basement and the sedimentary cover above the Hormuz Salt, but if this takes the form of a low-angle thrust, it is evidently aseismic. The high-angle reverse faulting occurs in earthquakes that can be much larger than the strike-slip events we studied on the Kazerun Line (see e.g. event C in Table 3), and the same arguments about source dimensions that we made for the strike-slip earthquakes apply equally to the reverse faults: their source dimensions are too big, and their centroid depths are too great for it to be likely that such faults can be contained within the sedimentary cover without producing surface ruptures. In other words, we agree with Jackson (1980), Jackson & Fitch (1981) and Ni & Barazangi (1986) that the reverse faulting earthquakes probably occur within the metamorphic basement.

The Kazerun Line thus appears to be a fundamental structure in the Zagros, confirming previous inferences based on its influence on the sedimentary record. The Kazerun Line is a recognizable feature in the isopach and facies maps of the Zagros since at least the middle Jurassic (e.g. Setudehnia 1978; Koop & Stoneley 1982). It may, as Falcon (1969) implies, be one of a system of much older, inherited structures with a N–S strike within the Arabian shield. Its past sense of motion could therefore have been different from its present day activity, which is that of a right-lateral strike-slip fault oblique to the regional strike, causing some elongation of the Zagros perpendicular to the direction of shortening.

7. Conclusions

The Kazerun Line is a valley that obliquely crosses the regular trend of anticline axes in the Zagros mountains. At the surface, the anticline axes appear to die out, or bend, as they approach the valley and do not cross it. The earthquakes we have studied demonstrate that the Kazerun Line is the surface expression of a buried right-lateral strike-slip fault. The source dimensions of these earthquakes, and their centroid depths, suggest to us that this buried faulting affects the metamorphic basement and is not confined to within the sedimen-

9

tary cover. High-angle reverse faulting earthquakes also occur near the Kazerun Line. The reverse faults have slip vectors that are different from those of the strike-slip earthquakes on the Kazerun Line, though both types have similar P axis azimuths. We conclude that the right-lateral strike-slip motion on the Kazerun Line contributes to the shortening between Arabia and central Iran by introducing an elongation of the Zagros parallel to the strike of the belt, though the rate of such elongation is probably small compared with the rate of shortening.

Strike-slip faulting that achieves shortening within mountain belts by along-strike elongation is not particularly rare, and has been known for some time in Asia (e.g. Molnar & Tapponnier 1975; Tapponnier & Molnar 1979). Transverse interruptions to the otherwise regular fold axes in a mountain belt have also been described elsewhere, such as in the Canadian Rockies and the Appalachians (e.g. Harris 1970; Dahlstrom 1970; Boyer & Elliott 1982). The importance of this study is that it demonstrates that transverse irregularities in belts of folded sediments may be related to basement faulting, and not just to lateral ramps within the thrust sheets that deform the sedimentary cover.

Acknowledgments

REFERENCES

Ala, M., 1974. Salt diapirism in southern Iran, *Am. Assoc. Petroleum Geologists Bull.* , **58**, 1758 1770.

Ambraseys, N. N., 1978. The relocation of epicentres in Iran, *Geophys. J. R. astr. Soc.*, **53**, 117 121.

Ambraseys, N. N. & Melville, C. P., 1982. A history of Persian earthquakes, *Cambridge University Press*, 219 pp.

Badley, M.E., Price, J.D. & Backshall, L.C., 1989. Inversion, reactivated faults and related structures: seismic examples from the North Sea, in *Inversion Tectonics*, Cooper, M.A. & Williams, G.D. (eds), *Spec. Publ. Geol. Soc. Lond.*, **44**, 201–219.

Berberian, M., 1976a. Contributions to the seismotectonics of Iran (Part 2), *Rep. geol. Surv. Iran*, **39**, 516pp.

Berberian, M., 1976b. Generalized fault map of Iran, *Geological Survey of Iran*, 1 Map.

Berberian, M., 1977. Contributions to the seismotectonics of Iran (Part 3), *Rep. geol. Surv. Iran*, **40**, 279pp.

Berberian, M., 1979. Evaluation of the instrumental and relocated epicentres of Iranian earthquakes, *Geophys. J. R. astr. Soc.*, **58**, 625–630.

Berberian, M, & Papastamatiou, D., 1978. Khurgu (north Bandar Abbas, Iran) earthquake of March 21, 1977: a preliminary field report and seismotectonic discussion, *Bull. seism.*

Soc. Am., **68**, 411–428.

Berberian, M. & King, G., 1981. Towards a paleogeography and tectonic evolution of Iran, *Canad. J. Earth Sci.*, **18**, 210–265.

Boyer, S.E. & Elliott, D., 1982. Thrust Systems, *Am. Assoc. Petroleum Geologists Bull.*, **66**, 1196–1230.

Colmann-Sadd, S. P., 1978. Fold development in Zagros Simply Folded Belt, Southwest Iran, *Am. Assoc. Petroleum Geologists Bull.*, **62**, 984–1003.

Dahlstrom, C.D.A., 1970. Structural geology in the eastern margin of the Canadian Rocky Mountains, *Bull. Canad. Petrol. Geol.* , **18**, 332–406.

Dewey, J. W. & Grantz, A., 1973. The Ghir Earthquake of April 10, 1972 in the Zagros Mountains of Southern Iran: Seismotectonic aspects and some results of a field reconnaissance, *Bull. seism. Soc. Am.*, **63**, 2071–2090.

Dziewonski, A. M. & Woodhouse, J. H., 1983. An experiment in the systematic study of global seismicity: Centroid-moment tensor solutions for 201 moderate and large earthquakes of 1981, *J. geophys. Res.*, **88**, 3247–3271.

Dziewonski, A. M., Ekström, G., Franzen, J. E. & Woodhouse, J. H., 1987a. Centroid-moment tensor solutions for July - September 1986, *Phys. Earth planet. Int.*, **46**, 305–315.

Dziewonski, A. M., Ekström, G., Franzen, J. E. & Woodhouse, J. H., 1987b. Centroid-moment tensor solutions for October - December 1986, *Phys. Earth planet. Int.*, **48**, 5–17.

Falcon, N. L., 1969. Southern Iran: Zagros Mountains, in *Mesozoic-Cenozoic Orogenic Belts*, edited by A. Spencer, *Spec. Publ. Geol. Soc. Lond.*, **4**, 199–211.

Friedrich, J., McCaffrey , R. & Denham, D., 1988. Source Parameters of Seven Large Australian Earthquakes determined by Body Waveform Inversion, *J. geophys. Res.*, **95**, 1–13.

Futterman, W. I., 1962. Dispersive Body Waves, *J. geophys. Res.*, **67**, 5279–5291.

Harris, L. D., 1970. Details of Thin-Skinned Tectonics in Parts of Valley and Ridge and Cumberland Plateau Provinces of Southern Applachians, in *Studies of Appalachian Geology: Central and Southern*, Fisher, G.W., Pettijohn, F.J., Reed, J.C. & Weaver, K.N. (eds.), Interscience Publishers.

Haynes, S. J. & McQuillan , H., 1974. Evolution of the Zagros Suture Zone, Southern Iran, *Bull. geol. Soc. Am.*, **85**, 739–744.

I.F.P., 1966. *Etude géologique de l'Epire (Grèce nord- occidentale)*, two volumes. Paris, Editions Technip. (Institute of Geology and Mineral Exploration, Athens & Institut Français du Petrole)

Jackson, J. A., 1980. Reactivation of basement faults and crustal shortening in orogenic belts, *Nature*, **283**, 343–346.

Jackson, J. A. & Fitch, T., 1979. Seismotectonic implications of relocated aftershock sequences in Iran and Turkey, *Geophys. J. R. astr. Soc.*, **57**, 209–229.

Jackson, J. A. & Fitch, T., 1981. Basement faulting and the focal depths of the larger earthquakes in the Zagros mountains (Iran), *Geophys. J. R. astr. Soc.*, **64**, 561–586.

Jackson, J. A. & McKenzie , D. P., 1984. Active tectonics of the Alpine-Himalayan Belt between western Turkey and Pakistan, *Geophys. J. R. astr. Soc.*, **77**, 185–264.

Kadinsky-Cade, K. & Barazangi, M., 1982. Seismotectonics of southern Iran: the Oman Line, *Tectonics*, 1, 389–412.

Kashfi, M. S., 1976. Plate tectonics and the structural evolution of the Zagros geosyncline, southwest Iran, *Bull. geol. Soc. Am.*, **88**, 739–744.

11

Koop, W. J. & Stoneley, R., 1982. Subsidence history of the Middle East Zagros Basin, Permian to Recent, *Phil. Trans. Roy. Soc. Lond.*, **305**, 149–168.

Lees, G.M. 1952. Foreland folding, *Q. Jl. geol. Soc. Lond.*, **108**, 4–34.

Letouzey, J., 1990. Fault reactivation, inversion and fold-thrust belt, in *Petroleum and Tectonics in Mobile Belts*, Letouzey, J. (ed), *Editions Technip. Paris*, 101–128.

McCaffrey, R. & Nábělek, J., 1987. Earthquakes, gravity, and the origin of the Bali Basin: an example of a nascent continental fold-and-thrust belt, *J. geophys. Res.*, **92**, 441–460.

McCaffrey, R. & Abers, G., 1988. SYN3: A program for inversion of Teleseismic Body Wave Forms on Microcomputers, *Air Force Geophysics Laboratory Technical Report, GL-TR-88-0099*, Hanscom Air Force Base, MA, 50 pp. **ADA198940**

McKenzie, D., 1972. Active tectonics of the Mediterranean region. *Geophys. J. R. astr. Soc.*, **30**, 109–185.

McKenzie, D. & Jackson, J., 1986. A block model of distributed deformation by faulting. *J. Geol. Soc. Lond.*, **143**, 249–253.

McQuillan, H., 1973. A geological note on the Qir earthquake, SW Iran, April 1972, *Geol. Mag.*, **110**, 243–248.

Molnar, P. & Tapponnier, P., 1975. Cenozoic tectonics of Asia: effects of a continental collision, *Science*, **189**, 419–426.

Molnar, P. & Deng, Q. 1984. Faulting associated with large earthquakes and the average rate of deformation in central and eastern Asia, *J. geophys. Res.*, **89**, 6203–7227.

Molnar, P. & Lyon-Caen, H. 1989. Fault Plane Solutions of Earthquakes and Active Tectonics of the Tibetan Plateau and its margin, *Geophys. J. Int.*, **99**, 123–153.

Morris, P. 1977. Basement structure as suggested by aeromagnetic surveys in S.W. Iran. *Oil Service Company of Iran*, internal report.

Nábělek, J., 1984. Determination of Earthquake source Parameters from Inversion of Body Waves, **Ph.D. Thesis, M.I.T.**

Nelson, M.R., McCaffrey, R. & Molnar, P. 1987. Source parameters for 11 earthquakes in the Tien Shan, central Asia, determined by P and SH waveform inversion, *J. geophys. Res.*, **92**, 12,628–12,648.

Ni, J. & Barazangi, M. 1984. Seismotectonics of the Himalayan Collision Zone: Geometry of the Underthrusting Indian Plate Beneath the Himalaya, *JGR*, **89**, 1147–1163.

Ni, J. & Barazangi, M., 1986. Seismotectonics of the Zagros Continental Collision Zone and a Comparison With the Himalayas, *J. geophys. Res.*, **83**, 8205–8218.

Roberts, D.G. 1989. Basin inversion in and around the British Isles, in *Inversion Tectonics*, Cooper, M.A. & Williams, G.D. (eds), *Spec. Publ. Geol. Soc. Lond.*, **44**, 131–150.

Scholz, C.H., Aviles, C.A. & Wessnousky, S.G. 1986. Scaling differences between large interplate and intraplate earthquakes, *Bull. seism. Soc. Am.*, **76**, 65–70.

Sengor, A. M. C. & Kidd, W., 1979. Post-collisional tectonics of the Turkish-Iranian Plateau and a comparison with Tibet, *Tectonophys.*, **55**, 361–379.

Setudehnia, A. 1978. The Mesozoic sequence in South-East Iran and adjacent areas, *J. Petrol. Geol.*, **1**, 1, 3–42.

Stöcklin, J., 1968. Structural History and Tectonics of Iran: A review, *Am. Assoc. Petroleum Geologists Bull.*, **52**, 1229–1258.

Stöcklin, J. 1974. Possible ancient continental margins in Iran, in *The geology of continental margins*, Burk, C.A. & Drake, C.L. (eds), Springer, New York, 873–887.

Stoneley, R. 1976. On the origin of ophiolite complexes in the southern Tethys region, *Tectonophys.*, **25**, 303–322.

Stoneley, R. 1982. On the structural development of the Wessex basin, *J. Geol. Soc. Lond.*, **139**, 543–554.

Tapponnier, P. & Molnar, P. 1979. Active faulting and late Cenozoic tectonics of the Tien Shan, Mongolia and Baykal region. *J. geophys. Res.*, **84**, 3425–3459.

Taymaz, T., Jackson, J. & Westaway, R., 1990. Earthquake mechanisms in the Hellenic Trench near Crete, *Geophys. J. Int.*, **102**, 695–731.

Taymaz, T., Jackson, J. & McKenzie , D. 1991. Active tectonics of the north and central Aegean Sea, *Geophys. J. Int.*, **106**, 433–490.

Valdiya, K.S. 1976. Himalayan transverse faults and folds and their parallelism with sub-surface structures of north Indian plains, *Tectonophys.*, **32**, 353–386.

Appendix

23 June 1968 (event A)

This earthquake was studied by Jackson & Fitch (1981), who on the basis of first motion polarity data, thought that it had a fault plane solution with a strike significantly different from the majority of Zagros reverse faulting events. The first motion data are shown in Figs. 3 and A2. Jackson & Fitch's (1981) fault plane solution had a NE strike, and was constrained solely by the first motion polarities at the regional stations JER and KBL, which were clear and impulsive (Fig. A2). The P waveforms, which they also studied, were not sensitive to the strike of the reverse fault.

Our minimum misfit solution is shown in Fig. A1. P wave forms are abundant and clear, with the characteristic 'M' shape of a reverse fault mechanism at shallow depth. SH waveforms are also clear and of similar amplitude to P. The SH waveforms are not compatible with Jackson & Fitch's (1981) fault plane solution, which must be incorrect. This is demonstrated in Fig. A2, which shows the SH waveforms for both the minimum misfit and Jackson & Fitch's solution. Thus, although the first motions at JER and KBL are unambiguous, they are also misleading, and incompatible with the fault orientation that is required by teleseismic waveforms. This is not especially unusual. Distortion of ray paths to regional stations can lead to their being plotted in positions on the focal sphere that are slightly incorrect. This is usually only noticeable at stations that anyway lie close to nodal planes, as in this case (see also Taymaz *et al.* 1990, 1991).

The minimum misfit solution shows a simple source at a depth of 9 ± 3 km (Jackson & Fitch (1981) obtained a depth of 8 ± 4 km from P waveforms alone). The observed P waveform at NAI is apparently too small by a factor of two. We could find no independent evidence that the station gain was wrongly recorded on the WWSSN film chip, so we simply excluded this waveform from the inversion.

The SH waveforms at COL and NAI were excluded from the inversion as their signal to noise ratio was poor. However these two stations plot in areas of the focal sphere where there is little station coverage and we include them in this figure to show that their amplitudes are compatible with that of our solution.

We conclude that this earthquake did, after all, have a mechanism that is typical of reverse faulting events in the Zagros, with a NW strike that is parallel to the local trend of the anticlines. This fault orientation is compatible with the meisoseismal data collected in Khesht-Konar Takhteh region following this earthquake.

6 April 1971 (event B)

This was one of the smallest events (m_b 5.2) we were able to study. No P waveforms

were large enough to model, and only 6 stations gave suitable SII waveforms (Fig. A3). The first motion readings allow for either a reverse or strike-slip faulting mechanism. Our minimum misfit solution is based on SII waveforms alone, and as such is compatible with either a thrust or strike-slip solution. These two solutions are plotted in the upper part of Fig. A3. The thrust solution (shown as a dashed line) is inconsistent with the first motion reading at AAE which has a very small dilatational component. Moreover the small size of the P waveforms relative to SII suggests to us that the strike-slip solution is more likely. In Fig. A4 we compare the waveform fits of the two solutions for 3 stations where a P waveform was available. In each case we used the short period onset time to align the synthetic as the signal was barely above the noise level. We also compare the fits of three SII waveforms for the two solutions. This shows that while the SII waveforms fit either model adequately, if this event was a thrust as Jackson and McKenzie (1984) suggested then we would expect much larger P waveforms than observed. We therefore prefer the strike-slip solution. Nonetheless, this is our least well constrained solution, and and strike is uncertain by ±25°. Depth is also difficult to constrain without P waveforms, and has a larger uncertainty than for the other earthquakes we studied.

10 April 1972 (event C)

This earthquake occurred NE and NW of the town of Qir (sometimes spelt Ghir), and is one of the largest events to occur in the Zagros in recent times. Ground reconnaissance (e.g. McQuillan 1973; Dewey & Grantz 1973) found no evidence of surface rupture, although a number of minor surface fissures were noted (Berberian, 1976a). The aftershock zone extended over ~40 km (Jackson and Fitch 1981). McQuillan (1973) noted that a number of anticline axes are bent in a dextral sense near the town of Quir.

Our minimum misfit solution is shown in Fig. A5. The source time function for this earthquake was complex, and Fig. A5 shows synthetic waveforms calculated for a double event, with the second sub-event 13.7s after the first and with a different strike. The short period seismograms of this earthquake also an additional arrival of energy, presumably related to a second sub- event, at about 14 seconds after the first P arrival. Fig. A6 shows the improved match of synthetic to observed seismograms when a second sub-event is included. Line A shows a single source, which fails to match the second downswing observed in all P waveforms. A second sub-event (line B) improves the fit noticeably. Even two sub-events are insufficient to match some of the later SII waveforms, which show an additional pulse at between 17.5 and 20.8 seconds (e.g. COP, TOL, PTO and VAL); but these stations are all in the same part of the focal sphere, and this late SII pulse may be a path effect.

Although both sub-events involved high-angle reverse faulting, the source parameters of the second are less well constrained than the first. We achieved best results when the strike of the second sub-event was rotated about 34° clockwise from the first and had about half the seismic moment; but we have not attempted to estimate uncertainties in the parameters of the second sub-event. The centroid depth of 9 ± 3 km for the first sub-event is similar to the 12 ± 4 obtained by Jackson & Fitch (1981) from P waveforms alone.

22 April 1976 (event D)

This was a simple earthquake, whose source parameters are well constrained by abundant P and SII waveforms (Fig. A7). Our minimum misfit solution is inconsistent with compressional first motions at two regional stations to the NE; though both stations are close to a nodal plane (see also event A, above).

14

12 July 1986 (event F)

First motion polarities are not abundant for this earthquake (Fig. 3), and are consistent with either a strike-slip or reverse fault mechanism. The small amplitudes of the P waveforms are, however, consistent with the strike-slip mechanism of the minimum misfit solution in Fig. A8. SH waveforms are particularly abundant and clear.

In Fig. A9 we compare our minimum misfit solution with two other source models. In line B the source orientation (strike, dip, rake) was held fixed at that given by the Harvard CMT solution (Dziewonski et al. 1987a). This solution has a similar orientation to ours, but it gives a significantly poorer fit to SH waveforms at SNG, VAL and ESK. In line C we show a possible reverse faulting solution. This was obtained by starting from a reverse fault mechanism with the same SH radiation pattern as our minimum misfit solution and then inverting for all source parameters. Although the inversion routine returned a reverse fault solution, the fit to the P waves is noticeably poorer than for the strike-slip solution in line A. The SH fit is not much changed, though is marginally better at SNG. We are confident that the strike-slip solution is the correct one in this case. This agrees with observations of the meisoseismal region which lies on the Kazerun Fault and has a north-south orientation in line with this structure (M. Berberian, *pers. comm.*).

This earthquake had the shallowest centroid depth (4 -2/+4 km) of the ones we studied. Depth is mainly constrained by P waveforms, because of their higher frequency content. In this case P waveforms at WWSSN stations are sparse (only VAL, NAI), but nonetheless impulsive, and suggestive of this shallow depth. Most of the digital P waveforms are from SRO instruments, whose narrow band response makes them poor at resolving centroid depth. There is a suggestion that the gain at NAI was incorrectly marked on the vertical long period WWSSN record (Fig. A8), but we can find no independent confirmation of this. Therefore it has not been included in the inversion and is marked with a '*'.

20 December 1986 (event G)

P waveforms for this event were very small compared to SH amplitudes, suggestive of a strike-slip mechanism. Although not many SH records were available, there were sufficient, with a good distribution of polarities, to constrain the SH nodal planes quite well (Fig. A10). P waves were noisy, but useful in indicating a small amplitude.

The Harvard solution for this event gives a similar strike-slip mechanism (see inset Fig. A10). This solution lies wihin the errors we calculate for our result. The rake in particular is poorly constrained in one direction and it is possible to obtain a reasonable fit to the SH waveforms for a mechanism with a larger thrust component. However, as before, the amplitudes of the P waveforms become unacceptably large.

11 August 1988a 16:00 (event H)

This was the first of two events in this area occurring within the space of 5 minutes. It had a magnitude of only m_b 5.3, and generated few clear P waveforms. However, SH waveforms are abundant, and constrain those nodal planes well (Fig. A11).

In Fig. A12 we compare the minimum misfit solution of Fig. A11 (line A) with the Harvard CMT solution (line B) and with a reverse fault that has a similar SH radiation pattern to our minimum misfit solution (line C), as we did in Fig. A9. The Harvard CMT solution produces a worse fit to the waveforms at several stations than does the minimum misfit solution. The reverse fault solution produces a similar fit to the SH waveforms, but a worse fit to the P amplitude at LZH than the minimum misfit solution.

15

11 August 1988 16:04 (event I)

The second and larger of the two events on this day has an improved data coverage. Our minimum misfit solution is shown in Fig. A13. In Fig. A14 we compare, as before, our minimum misfit solution with the Harvard CMT solution (line B), and with a reverse fault mechanism with a similar SH radiation pattern (line C). The Harvard CMT solution is little different from our own, whereas the reverse fault mechanism greatly overestimates the amplitudes of the P waveforms at PTO and KBS.

6 December 1988 (event K)

This earthquake is discussed in the main text (Fig. 4).

Event	Year	Month	Day	Origin Time	Lat.	Long.	m_b
A	1968	06	23	09:16:18.6	29.81	51.16	5.2
B	1971	04	06	06:49:52.9	29.80	51.88	5.2
C	1972	04	10	02:06:53.2	28.43	52.82	6.1
D	1976	04	22	17:03:07.9	28.71	52.12	6.0
†E	1981	04	01	10:16:59.2	29.84	51.50	5.4
F	1986	07	12	07:54:26.8	29.96	51.58	5.7
G	1986	12	20	23:47:08.9	29.98	51.62	5.5
H	1988	08	11	16:00:07.5	29.97	51.57	5.3
I	1988	08	11	16:04:45.6	29.97	51.67	5.7
†J	1988	08	30	17:30:21.3	29.95	51.70	4.9
K	1988	12	06	13:20:41.0	29.94	51.65	5.5
†L	1989	05	03	09:13:20.0	29.96	51.65	5.1
†M	1990	12	16	22:18:50.0	29.05	51.31	5.3

'†' Events for which insufficient waveforms were available to model. Here the Harvard CMT solution is used.

Table 1 : List of earthquakes studied in this paper. Locations and origin times are taken from ISC listings prior to 1988. After this PDE locations are used. The event letters correspond to those used in the text.

Line	Layer	Depth	V_p	V_s	ρ
A	half space		6.5	3.5	2.7
B	half space		6.7	3.75	2.8
C	1	7	5.7	3.4	2.6
	half space		6.8	3.9	2.9
D	1	7	6.0	3.7	2.75
	half space		6.8	3.9	2.9

Table 2 : Velocity structures used in figure 6.

Event	Date	M_w	Solution					Errors			
			Strike	Dip	Rake	Depth	M_o $\times 10^{16}$	Strike	Dip	Rake	Depth
			(°)	(°)	(°)	(km)	(Nm)	(°)	(°)	(°)	(km)
A	23.6.68	5.5	136	45	88	9	22	-15/+10	-4/+5	-10/+15	±3
B	6.4.71	5.3	62	79	2	6	7.2	±25	-12/+10	-15/+20	-2/+6
C	10.4.72	6.6	288	49	99	9	844	±20	-8/+10	-15/+20	±3
	multiple	(6.7)	322	40	98	10	369				
D	22.4.76	5.7	312	52	80	7	38	-15/+10	-7/+10	±15	±3
†E	1.4.81	5.4	351	34	144	15*	7.8				
F	12.7.86	5.5	004	73	-159	4	26	-8/+10	±15	-15/+20	-2/+4
G	20.12.86	5.3	344	65	163	8	11	±10	-17/+10	-30/+10	±3
H	11.8.88a	5.5	003	69	-175	7	24	-18/+10	-15/+5	-18/+10	-4/+3
I	11.8.88b	5.8	350	82	-166	9	65	-16/+10	-10/+9	-12/+9	-3/+2
†J	30.8.88	5.1	337	83	-147	15*	6.1				
K	6.12.88	5.6	357	74	198	10	32	±10	-10/+5	±15	±2
†L	3.5.89	5.1	153	55	-166	15*	8.4				
†M	16.12.90	5.7	144	67	87	15*	41				

Table 3 : Minimum misfit solution and errors for events modelled in this study. The strike, dip and rake for events F,G,H,I,K are given for the nodal planes that we think are the fault planes. '†' indicates a Harvard CMT solution. The reported depths for these four events are fixed values so we indicate them with a '*'.

18

Figure Captions

Plate 1 : *Landsat 4* image of the region around the Kazerun Line. The main features and earthquake locations are shown in figure 1. Note how the anticline ridges do not cross the line and how they are apparently deflected as they approach it.

Figure 1 : Location Map showing the main faults and topography in the region of the Kazerun Flexure (or Kazerun Line). The valley that marks the Kazerun Line is indicated by a thin line. The epicentres of the earthquakes discussed in this study are marked by their date (year, month, day). Principal towns are marked as black squares. The inset shows the area in relation to the Persian Gulf, with the seismic belt defining the Zagros Mountains shaded. ZTL is the Zagros Thrust Line. The dashed line defines the area shown in the satellite image in Plate 1.

Figure 2 : Map showing the main geological features near the town of Kazerun (marked as K). The unshaded region corresponds to sediment of Quaternary age. The Agha Jari Formation is of Miocene to Pliocene age and consists primarily of continental conglomerates, sandstone, silt and mud. The Mishan and Gascharan formations are of Miocene age, consisting of limestones, marls and thick evaporites. The Asmari and Jahrum formations consist mainly of limestones of Palaeocene to Oligocene age. The Bangestan group contains limestones and shales of Cretaceous age.

Figure 3 : Lower hemisphere equal area projections of P wave first motion data. Station positions have been plotted using a velocity of 6.8 kms^{-1}, as used in the waveform synthesis. In each case the nodal planes are those of the minimum misfit solution obtained from waveform inversion. Filled circles are compressional first motions and open circles are dilatations. Large symbols are readings taken from WWSSN long period records. Nodal onsets are marked as crosses. P and T axes are marked by letters. The earthquake date (year, month, day) is above each focal sphere.

Figure 4 : The P and SH waveforms for the minimum misfit solution obtained for the event of 6 December, 1988 (Event J). The values beneath the event header give strike , dip, rake, depth and seismic moment (in units of Nm). The upper sphere shows the P wave radiation pattern and the lower sphere that for SH. Both are lower hemisphere projections. The station code by each waveform is accompanied by a letter corresponding to its position within the focal sphere. These are ordered clockwise by azimuth. A 'w' corresponds to WWSSN data and a 'd' to data from the GDSN network. The solid lines are the observed waveforms, the dashed lines are the synthetic waveforms. The inversion window is marked by solid bars at either end of the waveform. P and T axes within the sphere are represented by solid and open circles respectively. The source time function is shown below the P focal sphere, with the waveform time scale below this. Waveform amplitude scales are to the left of the focal sphere.

Figure 5 : Comparison of possible fault plane solutions for the event of 6 December 1988. Waveforms are shown at 6 representative stations. In line A, synthetic waveforms are from the minimum misfit solution. Line B shows synthetic waveforms for the orientation given by the Harvard moment tensor solution. Line C shows a thrust solution which gives a satisfactory fit to first motion readings and which is characteristic of thrust events seen in

the Zagros. In this, and in subsequent similar diagrams, an arrow signifies a poorer fit than the minimum misfit solution and an '*' an improvement in fit.

Figure 6 : Tests showing the influence of source velocity structure on the minimum misfit solution for the event of 6 December 1988. The velocity structure used in each line is given in Table 2. Each line shows the P and SH radiation patterns, the source time function and the resulting waveform fits for for 5 stations. Line D shows the structure which was used to obtain the minimum misfit solution in Fig. 4

Figure 7 : Summary map of the minimum misfit solutions for events studied in this paper. Fault plane solutions are shown as lower hemisphere projections joined to their epicentral locations. The letter beside each focal sphere identifies each event in Tables 1 and 3. The focal spheres with the striped shading (E and K) are Harvard CMT solutions.

Figure 8 : Map showing the horizontal projections of the slip vectors for the earthquakes discussed in this study. These are plotted so as to show motion of the south or west side relative to the north or east. Letters identify the events in Tables 1 and 3. Large filled circles are strike-slip events studied in this paper. Open circles are Harvard CMT solutions. Filled squares are reverse faulting events studied in this paper. The inset in the bottom left hand corner shows a stereographic projection of slip vectors for the 9 events whose waveforms we studied. Closed circles are strike-slip events, open circles are Harvard CMT solutions and filled squares are reverse faults.

Figure 9 : Lower hemisphere projection of the P and T axes for the events studied in this paper.

Figure A1: Minimum misfit solution for event A, on 23 June 1968. The display convention is the same as in Fig. 4. Stations marked with a '*' (eg NAI and COL) are not included in the inversion.

Figure A2 : Comparison of the minimum misfit solution in Fig. A1 (Line A) with that obtained by Jackson and Fitch (1981) (Line B). The focal spheres in the lower half of the diagram show the first motion readings for this event with these two solutions. The seismograms for the two stations with inconsistent first motions are shown.

Figure A3 : Minimum misfit solution for event B (6 April 1971). The display convention is the same as in Fig. 4.

Figure A4 : Comparison of thrust and strike-slip solutions for event B. While either solution provides an adequate fit to the SH waveforms, the small relative size of the P waveforms suggests the strike-slip solution is more likely.

Figure A5 : Minimum misfit solution for event C (10 April 1972). The display convention is the same as in Fig. 4. There are two sub-events in this case. The two mechanisms are printed under the header and the second source is represented as a dashed line within the focal sphere. The source time function shows two distinct ruptures, the second occurring some 13.7 seconds after the onset of the first.

Figure A6 : This figure shows the effect of each of the two sub-events in Fig. A5 on the

waveforms for the earthquake of 10 April 1972. Line A shows waveforms from the first sub-event only. Line B shows the modifications to the waveforms when both sub-events are included.

Figure A7 : Minimum misfit solution obtained for event D (22 April 1976). The display convention is the same as in Fig. 4.

Figure A8 : Minimum misfit solution obtained for event F (12 July 1986). The display convention is the same as in Fig. 4.

Figure A9 : Comparison of solutions for event F. Line A shows our minimum misfit solution. Line B shows the Harvard moment tensor solution. Line C is a reverse faulting solution with a similar SH radiation pattern to that in line A.

Figure A10 : Minimum misfit solution for event G (20 December 1986). The display convention is the same as in Fig. 4.

Figure A11 : Minimum misfit solution for event H (11 August 1988a). The display convention is the same as in Fig. 4.

Figure A12 : Comparison of models for event H. Line A shows the minimum misfit solution. Line B shows the Harvard moment tensor solution. Line C is a reverse faulting solution with a similar SH radiation pattern to that in line A.

Figure A13 : Minimum misfit solution for event I (11 August 1988b). The display convention is the same as in Fig. 4.

Figure A14 : Comparison of models for event I. Line A shows the minimum misfit solution. Line B shows the Harvard moment tensor solution. Line C is a reverse faulting solution with a similar SH radiation pattern to that in line A.

FIGURE 1

22

FIGURE 2

23

FIGURE 3

24

FIGURE 4

25
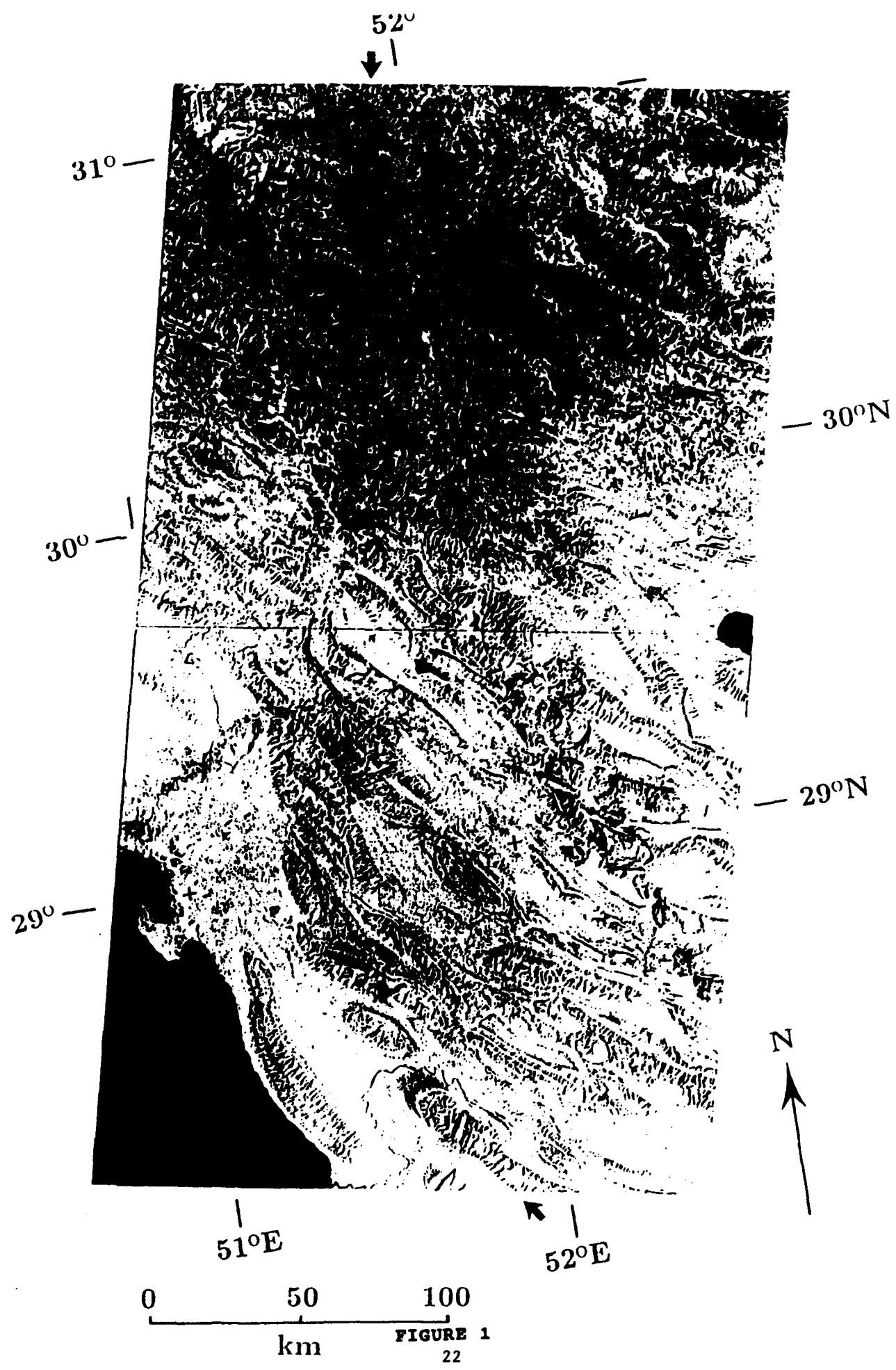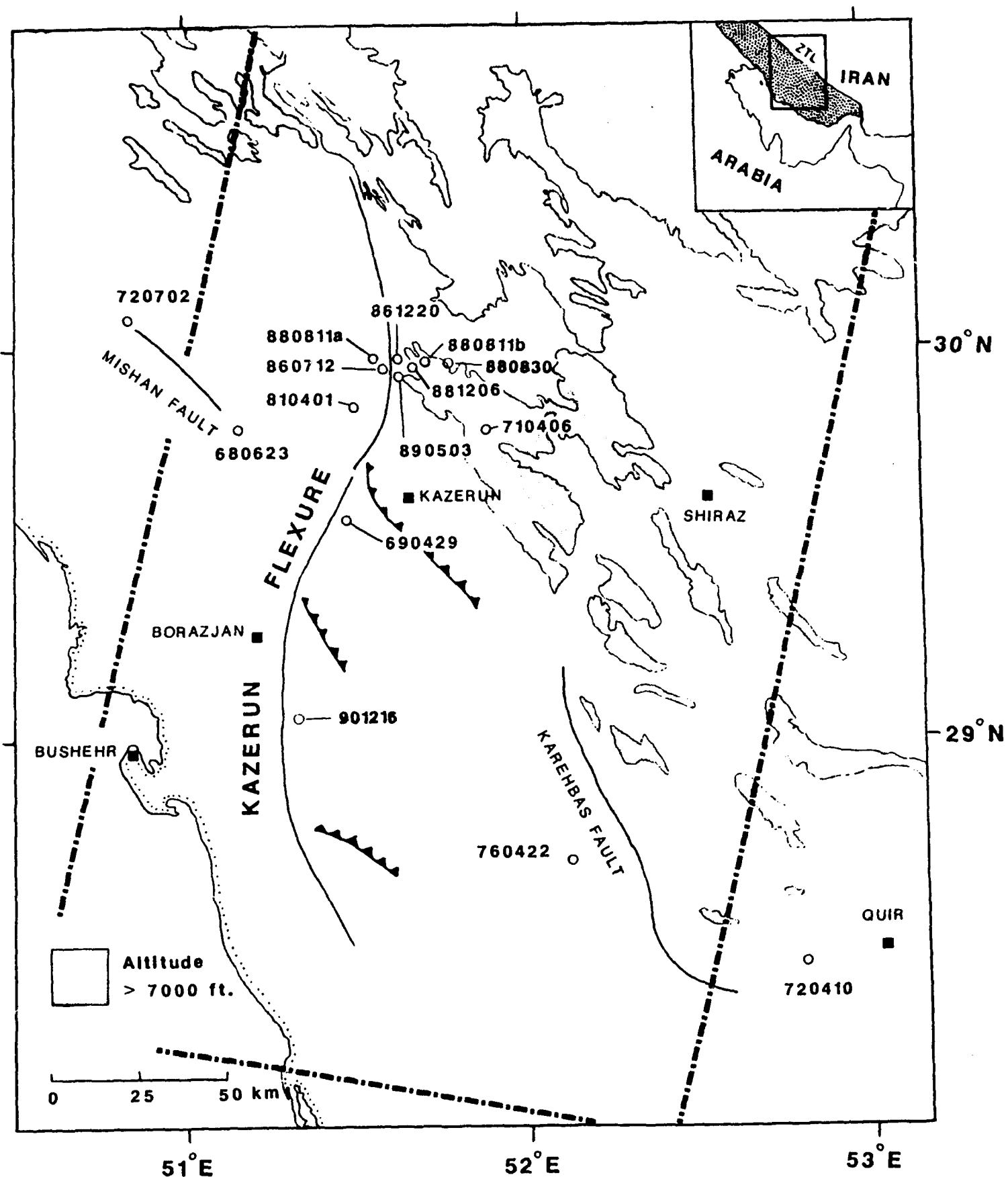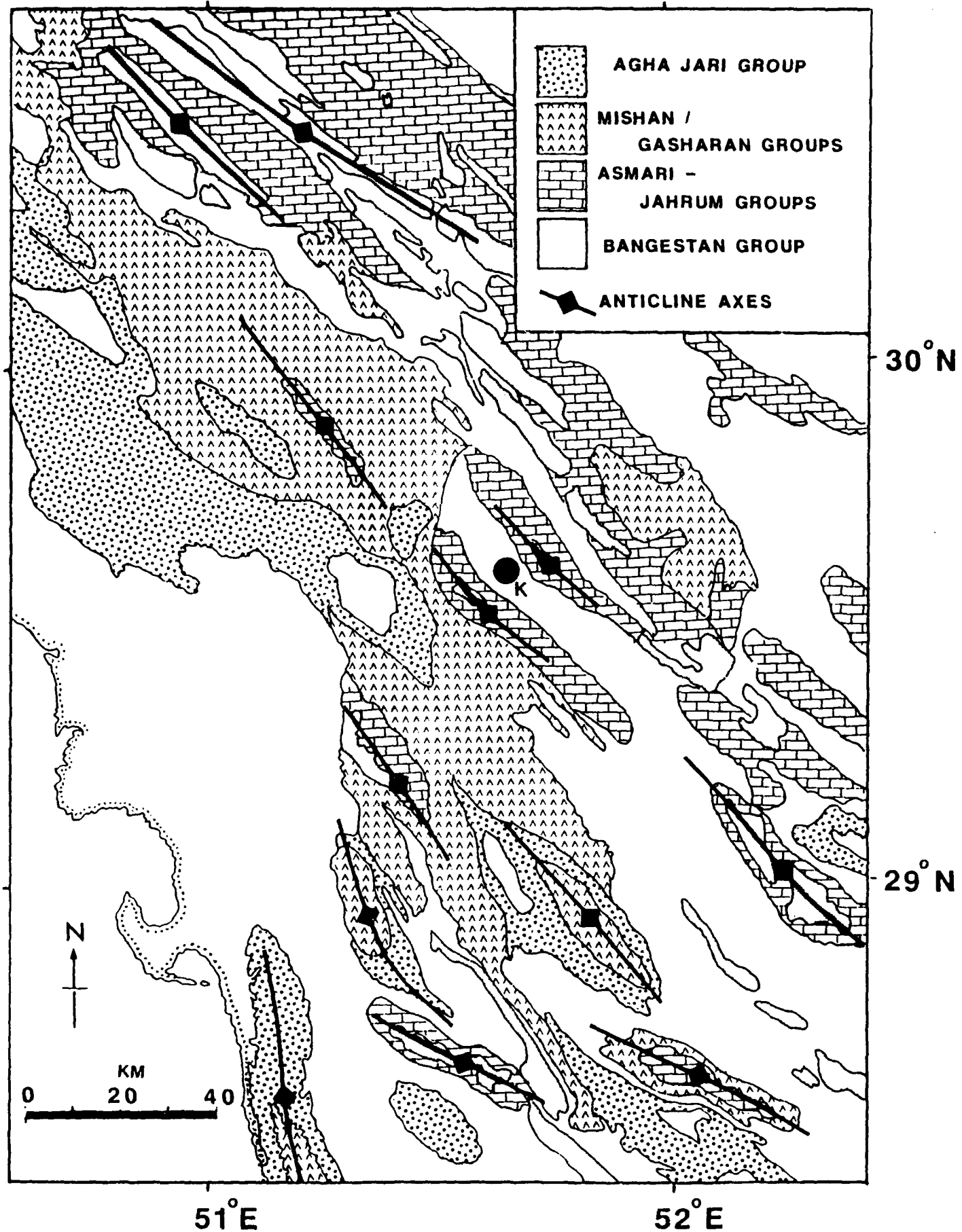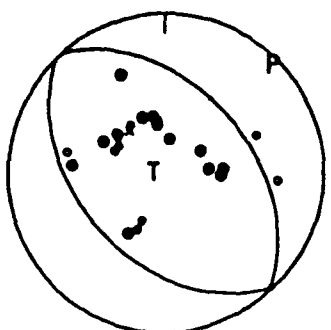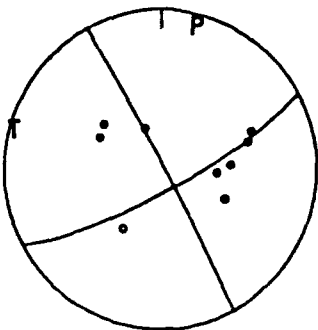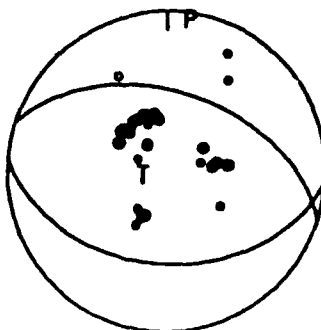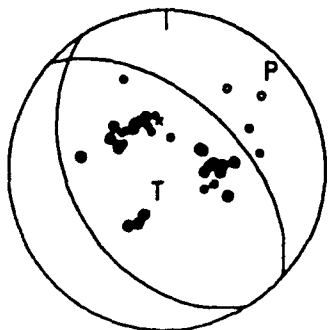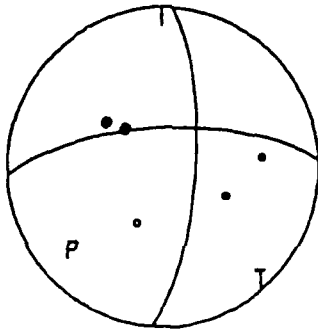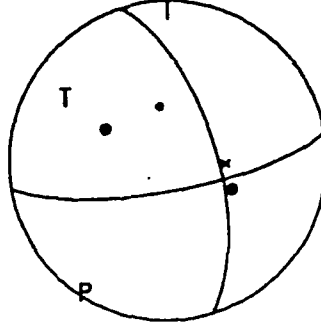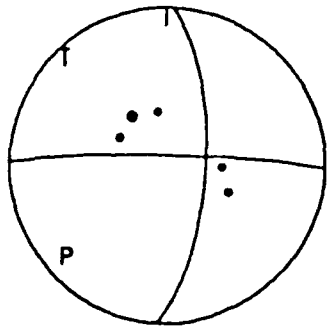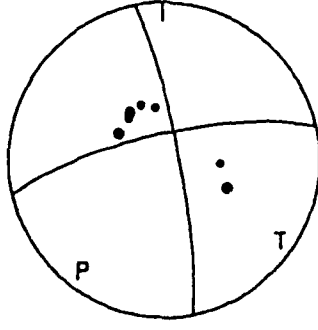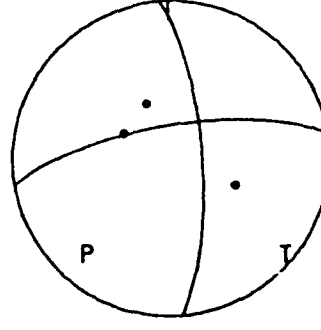
6 December 1988 mb:5.5
357/74/198/10/3.253E17

**FIGURE 5**

26
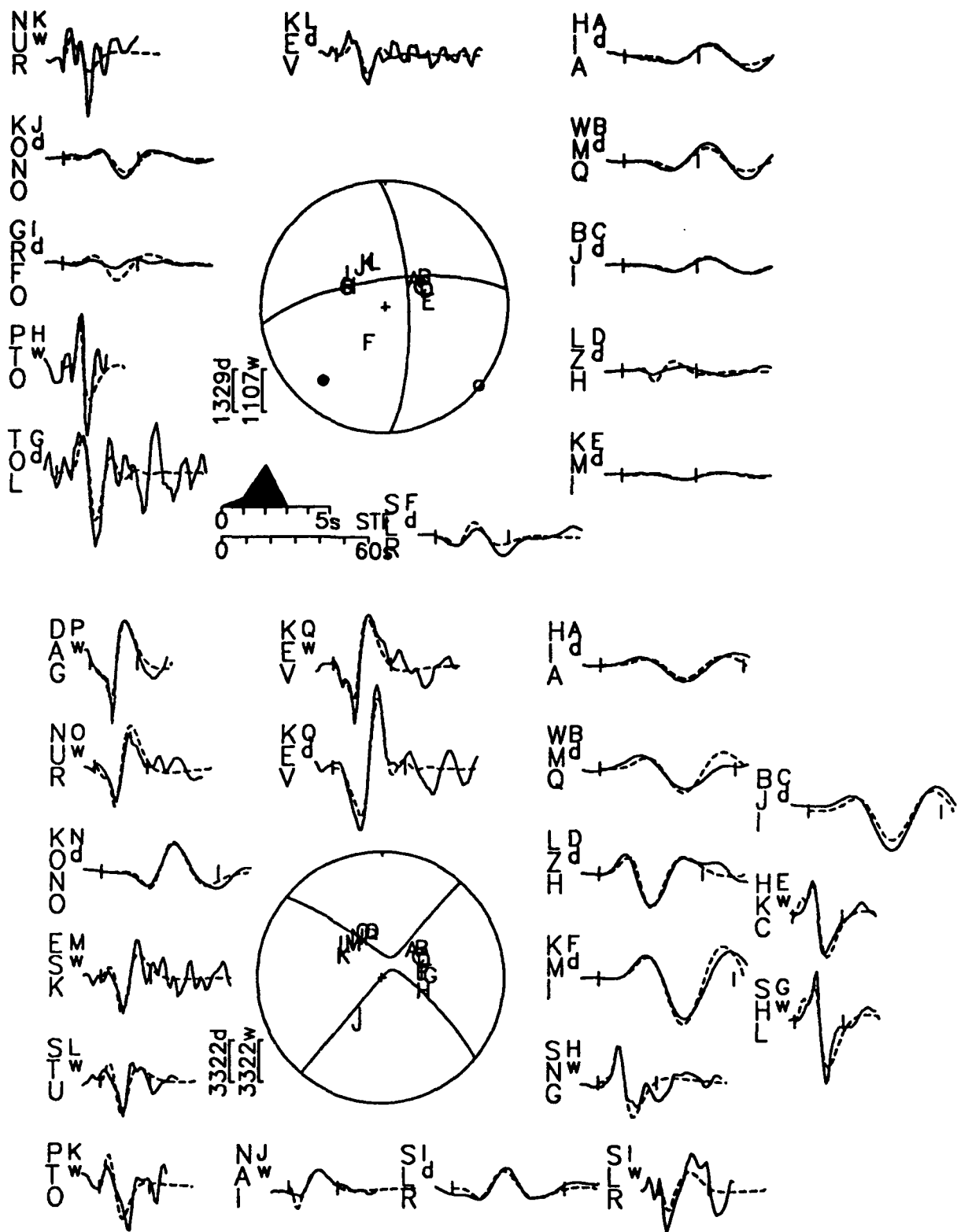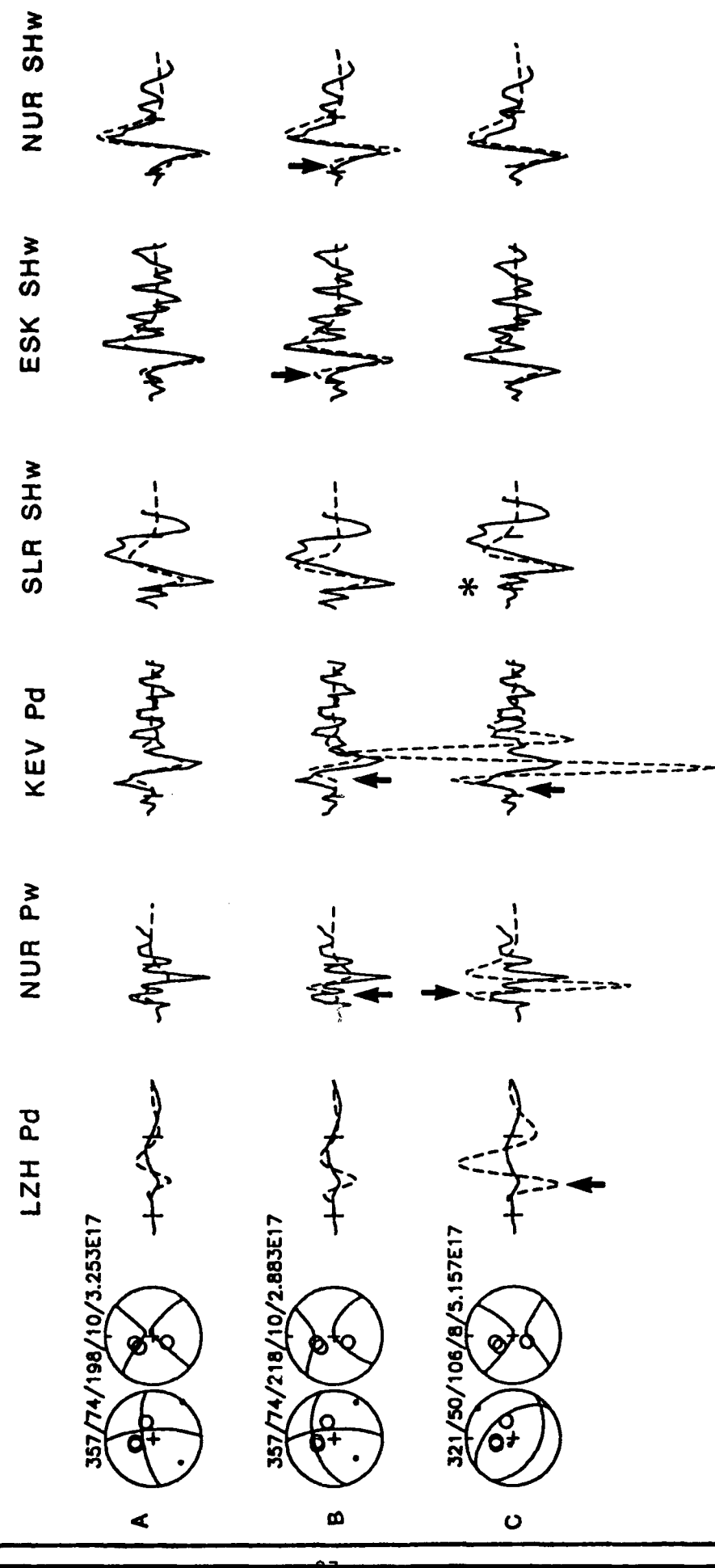
FIGURE 6

6 December 1988 – Effect of source structure variations.

FIGURE 6

28

FIGURE 7

29
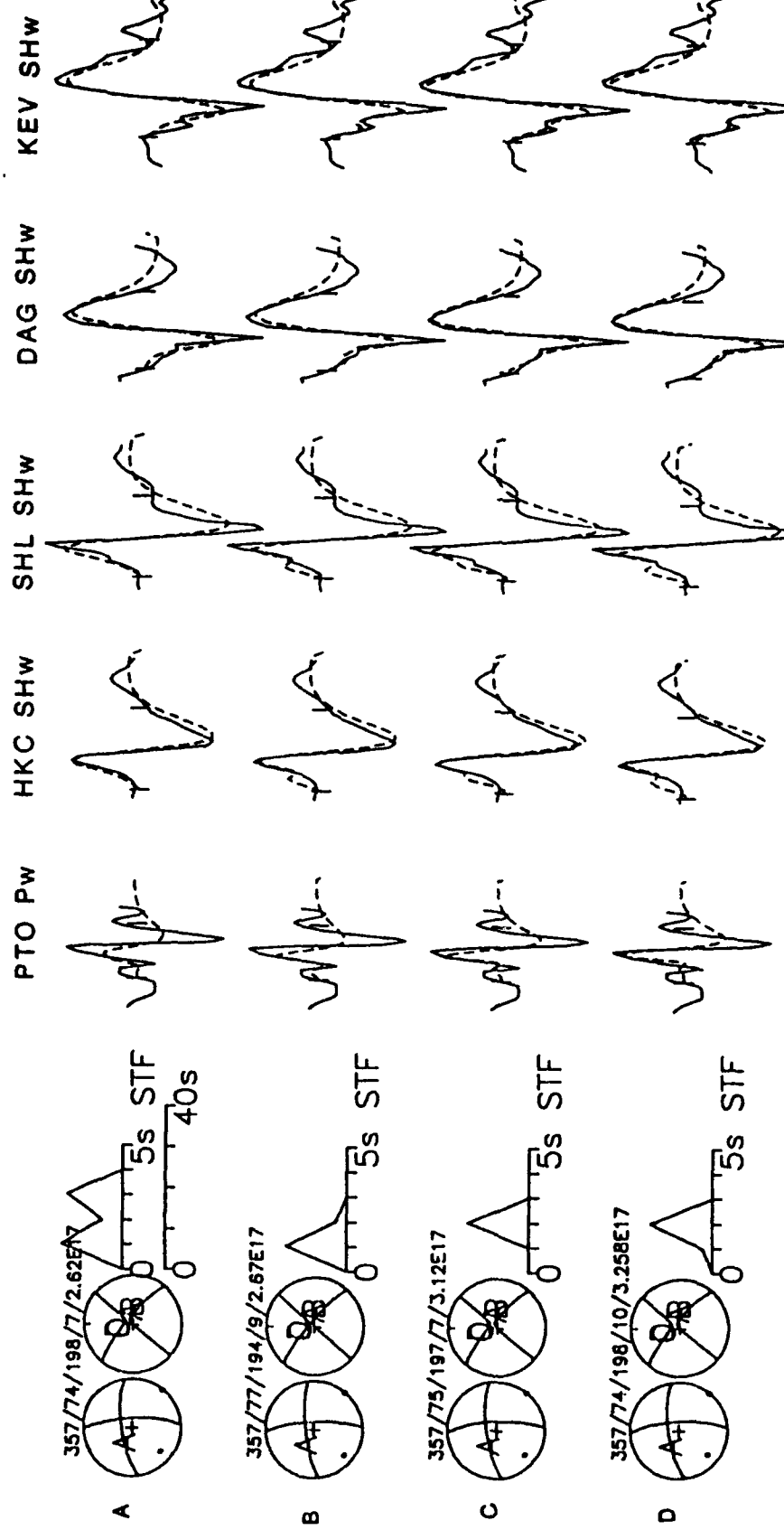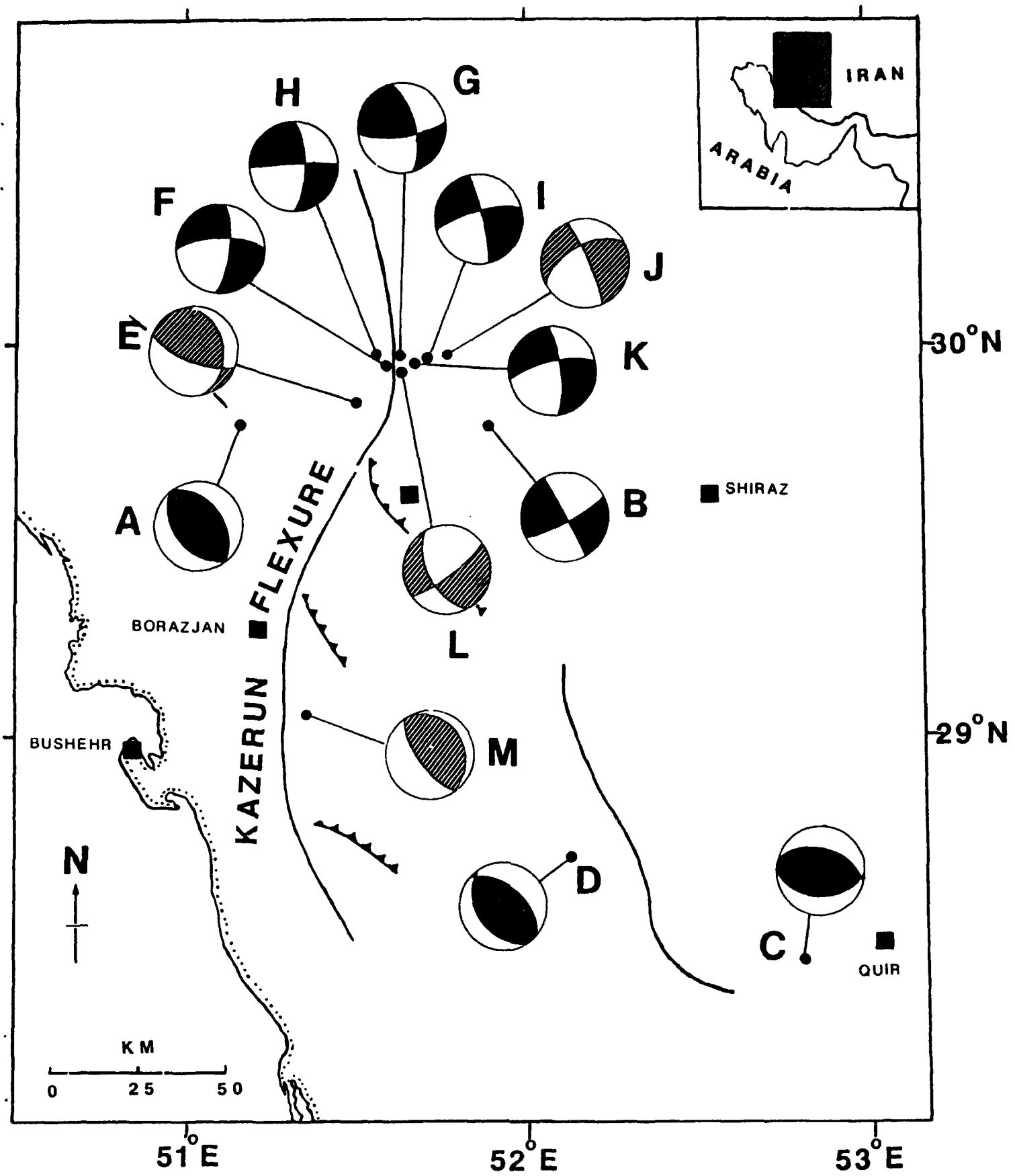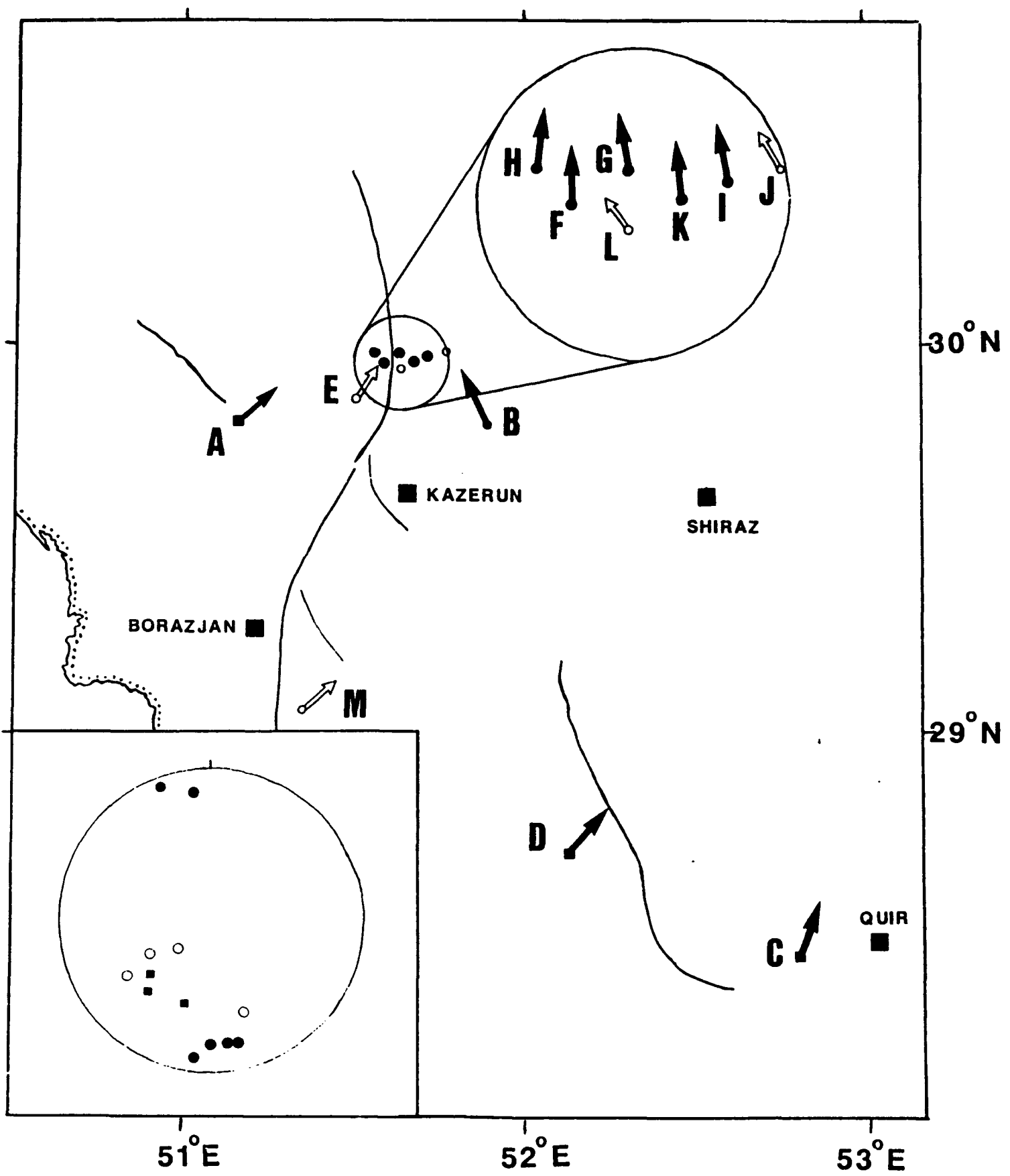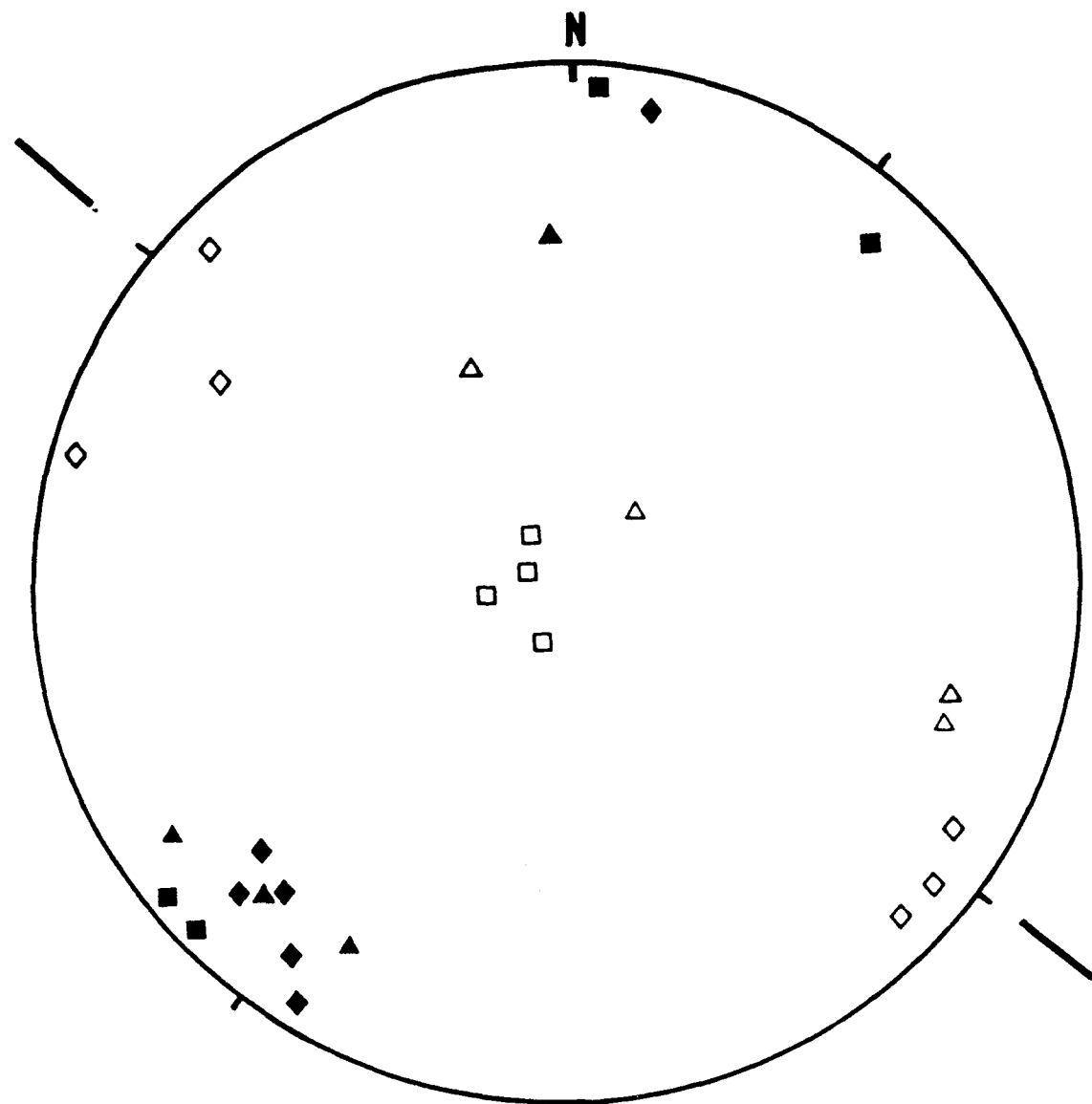
FIGURE 8

Principal axes of strain for events around Kazerun Line.

	T axes	P axes
Thrust Faults	□	■
Strike-slip Faults	◇	◆
CMT solutions	△	▲

Strike of Main Zagros Thrust. ▬▬▬▬   ▬▬▬▬

FIGURE 9
31

23 June 1968 mb:5.2
136/45/88/9/2.26E17
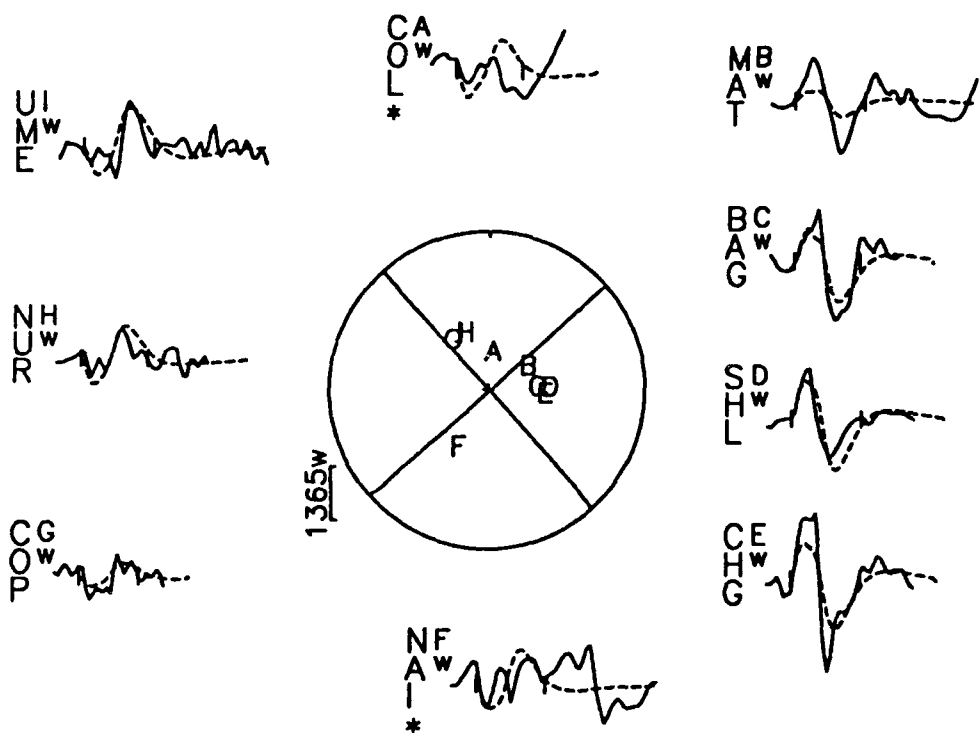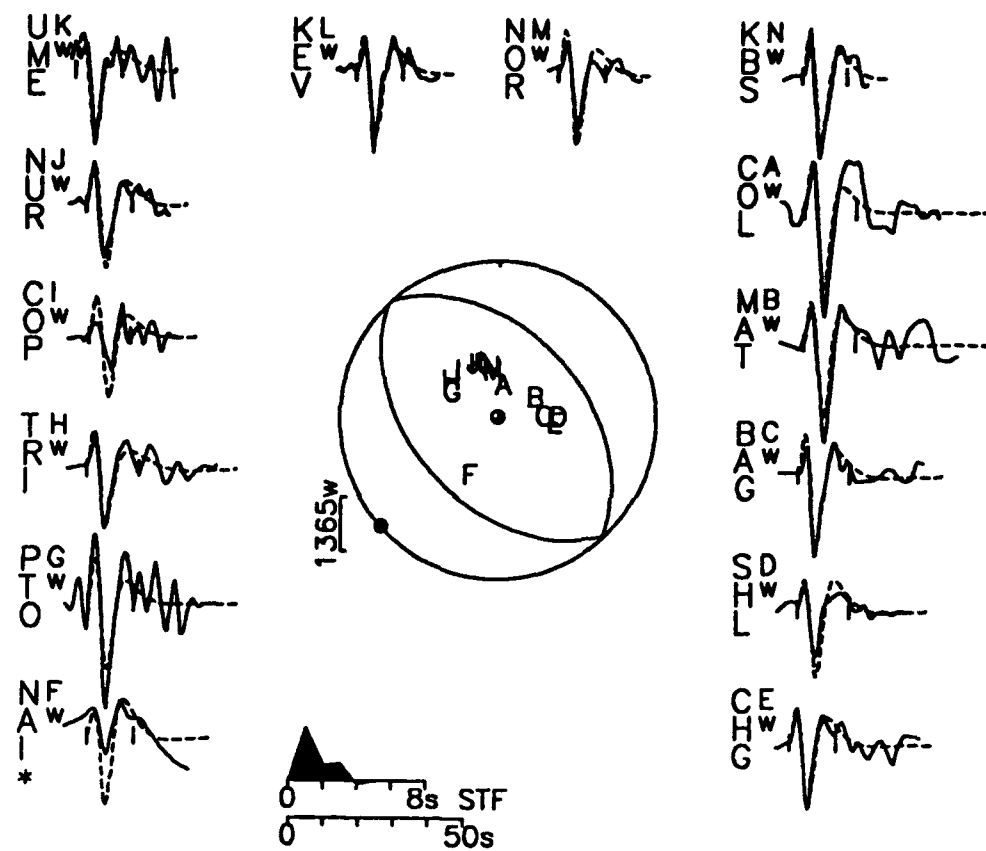
FIGURE A1
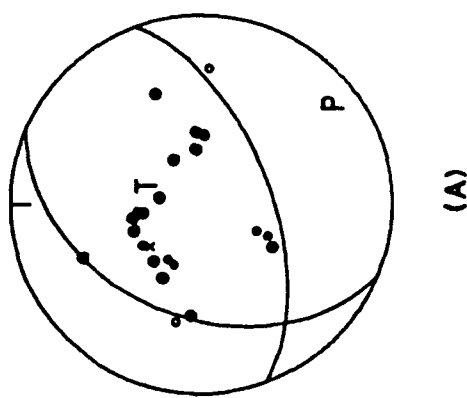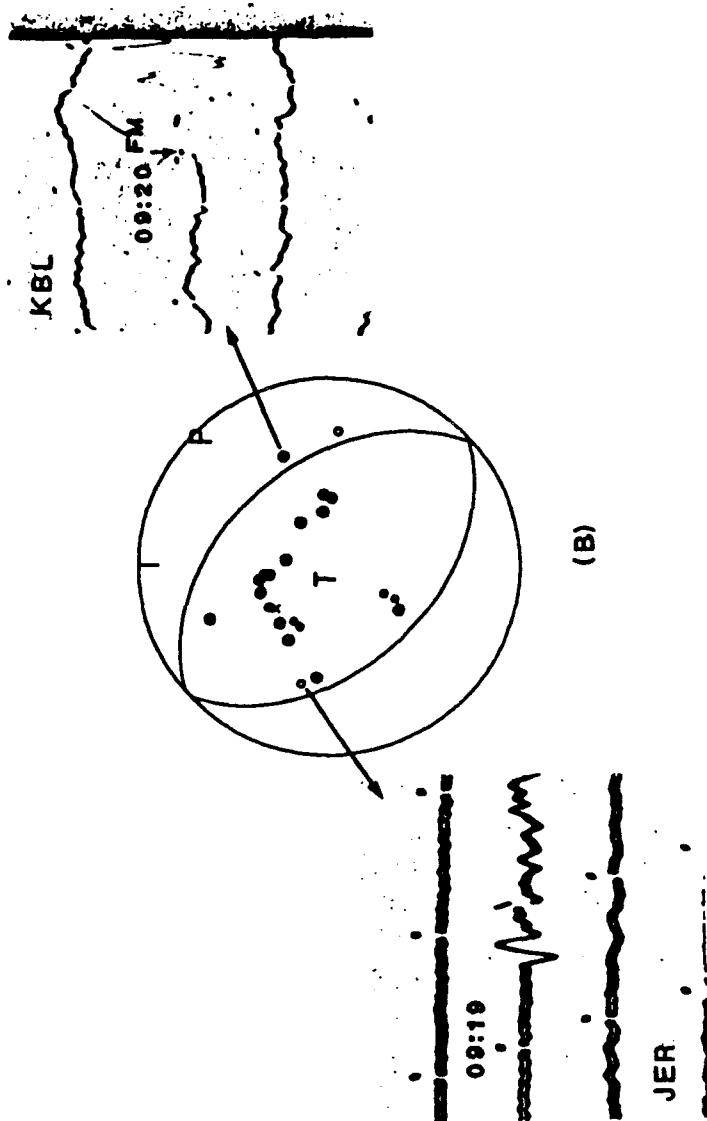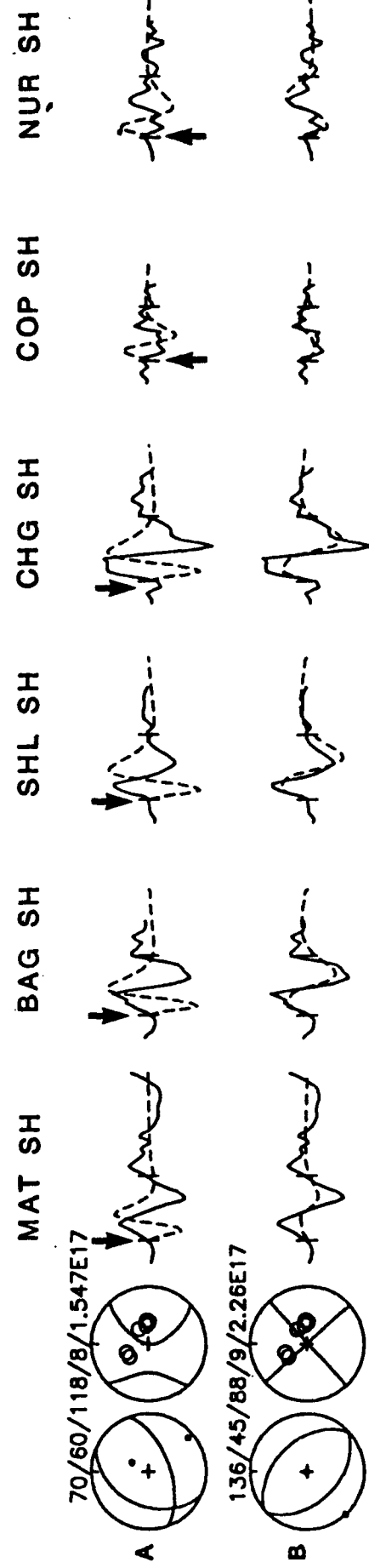
FIGURE A2

6 April 1971 mb:5.2
62/79/2/6/7.233E16
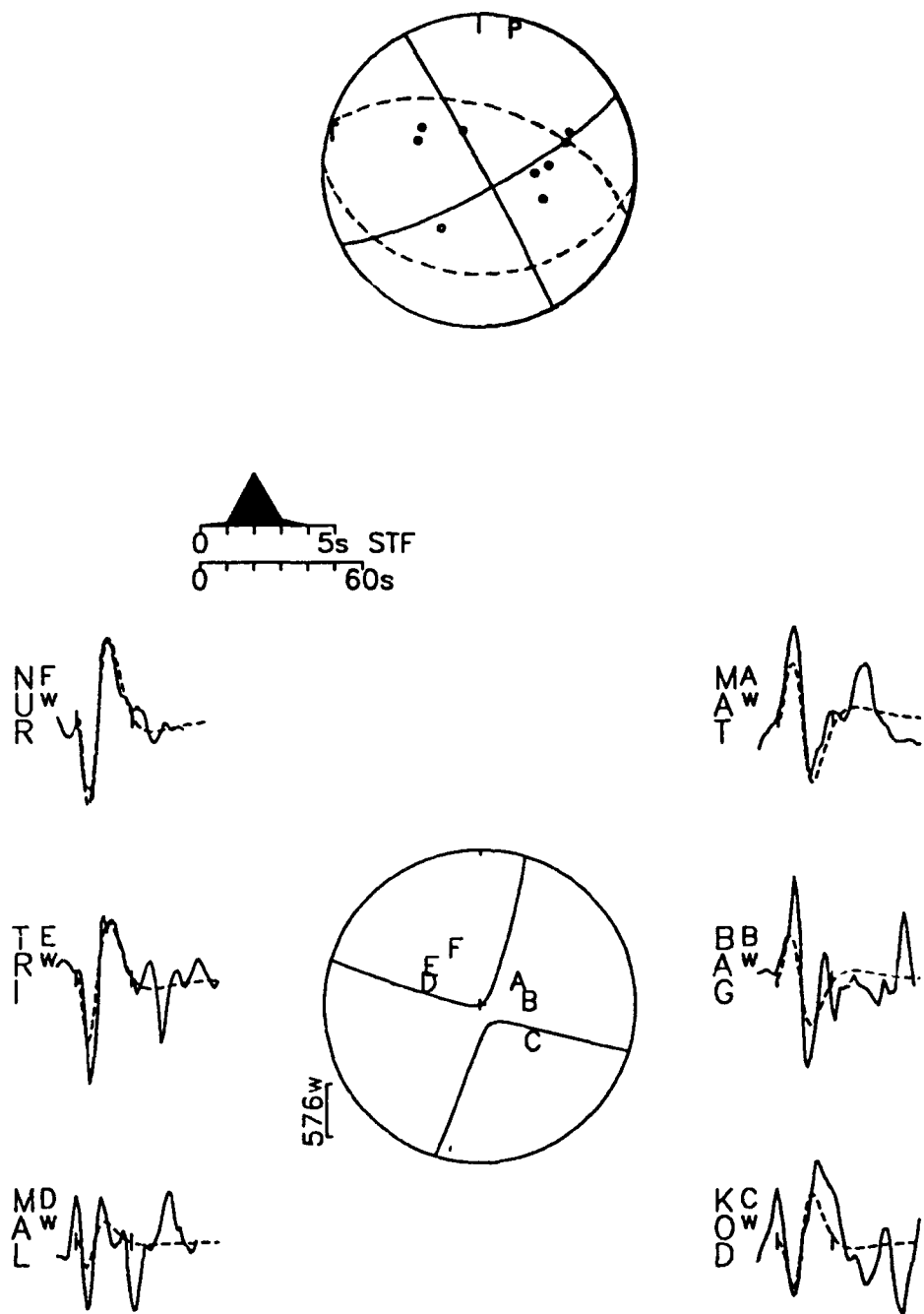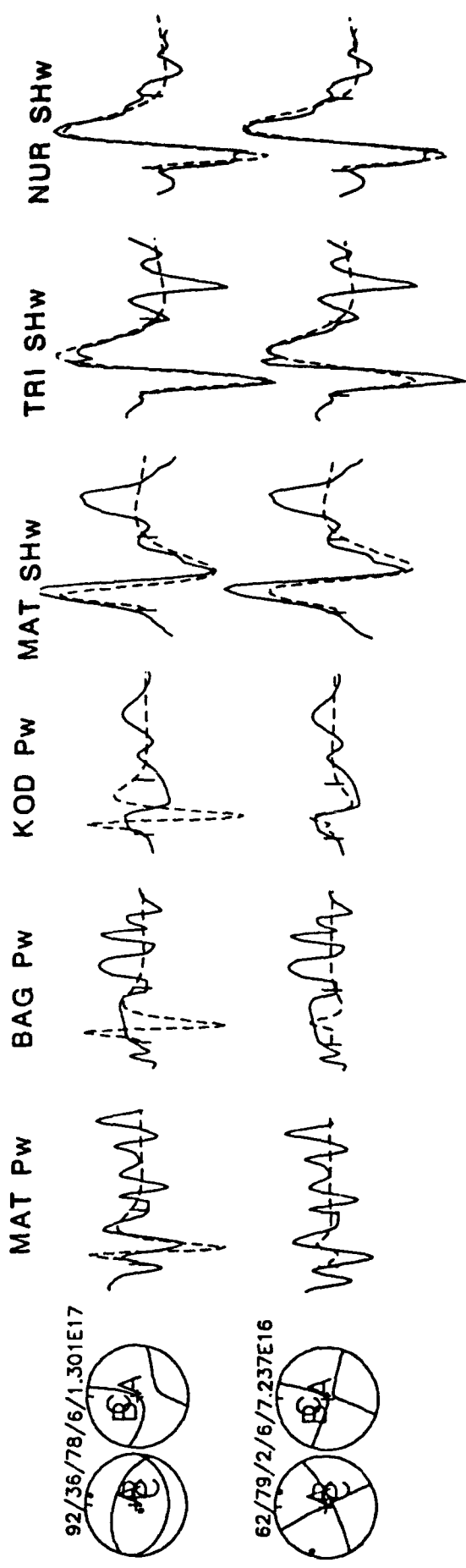
FIGURE A4

10 April 1972 mb:6.1
1:288/49/99/9/8.445E18
2:322/40/98/10/3.709E18
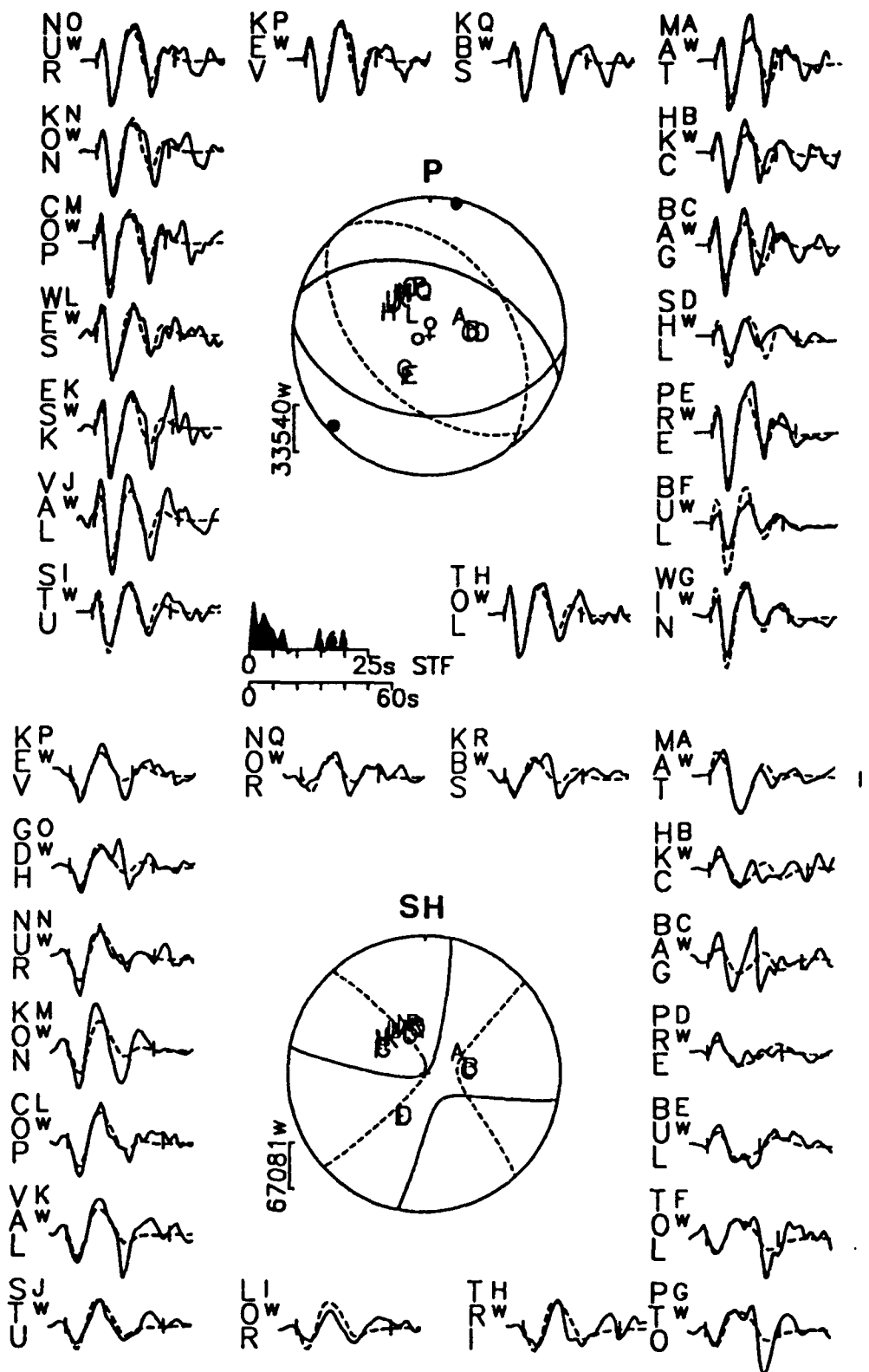
FIGURE A5
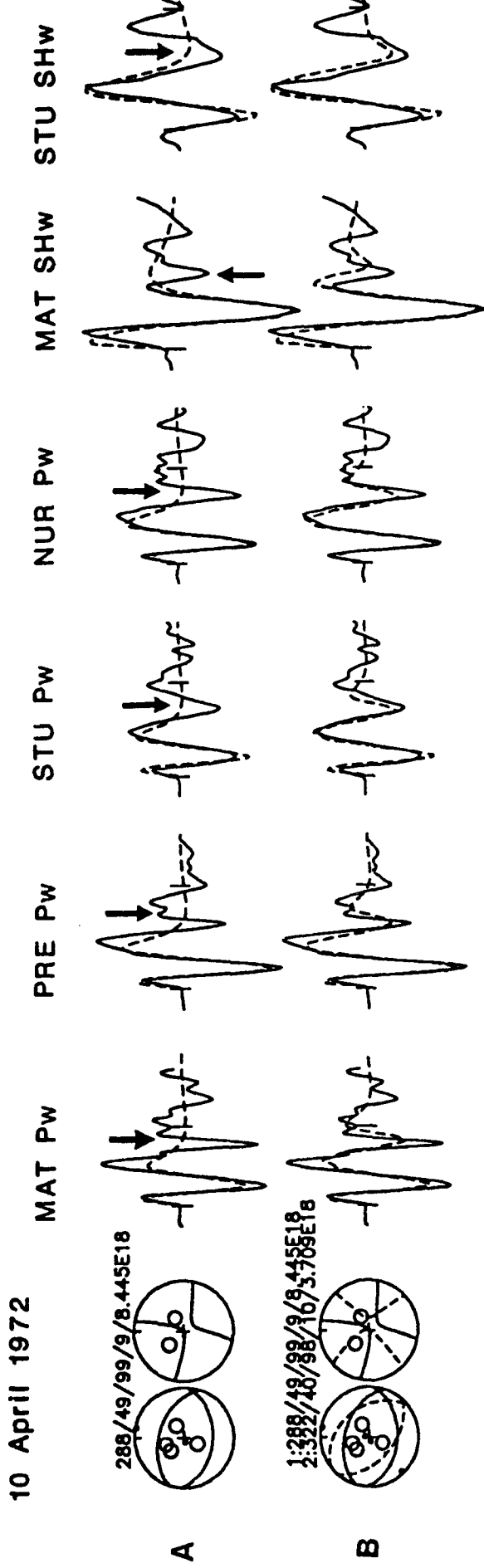
FIGURE A6

22 April 1976 mb:6.0
312/52/80/7/3.81E17
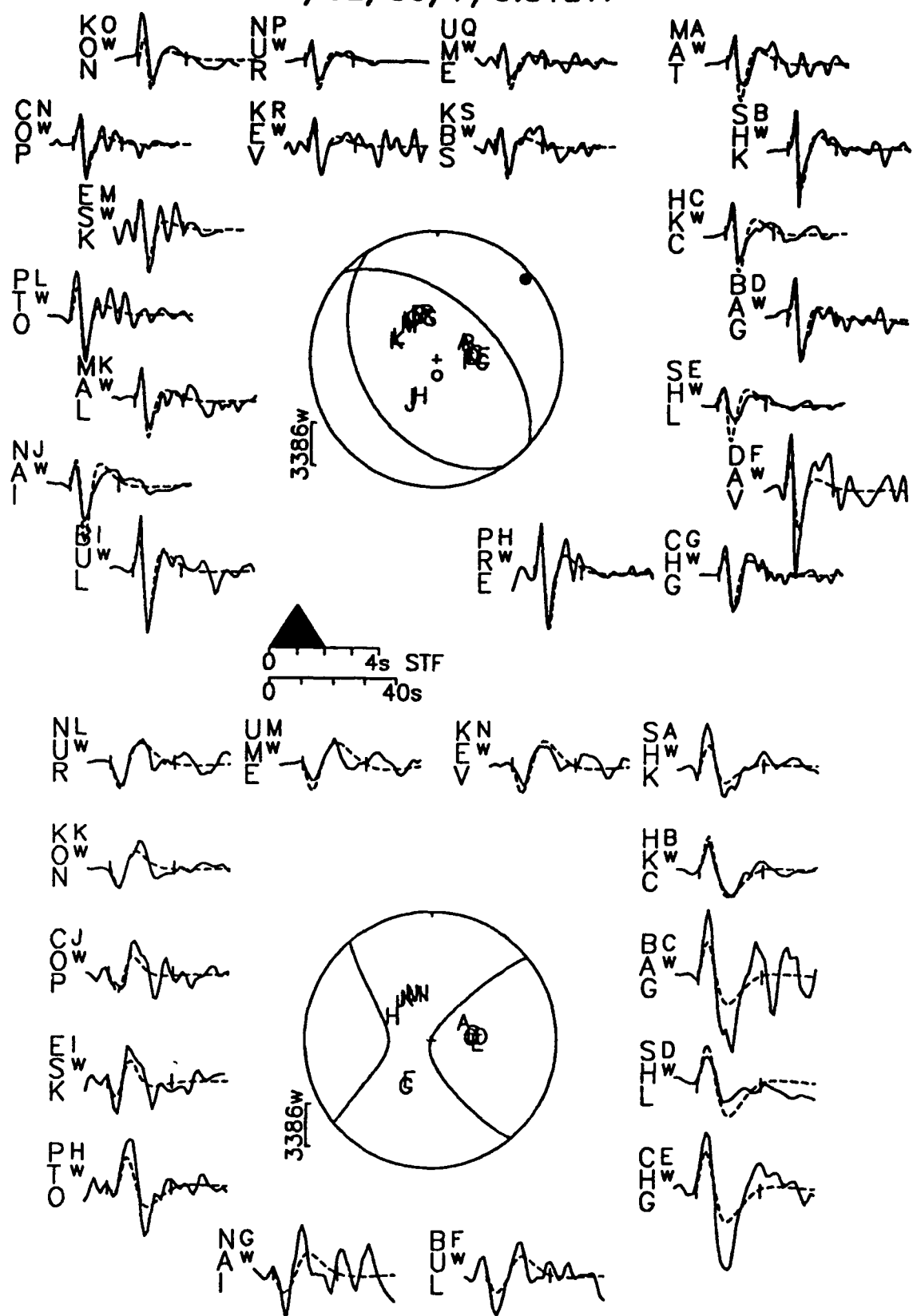
FIGURE A7

12 July 1986 mb:5.7
268/70/342/7/2.643E17

FIGURE A8

FIGURE A9

40
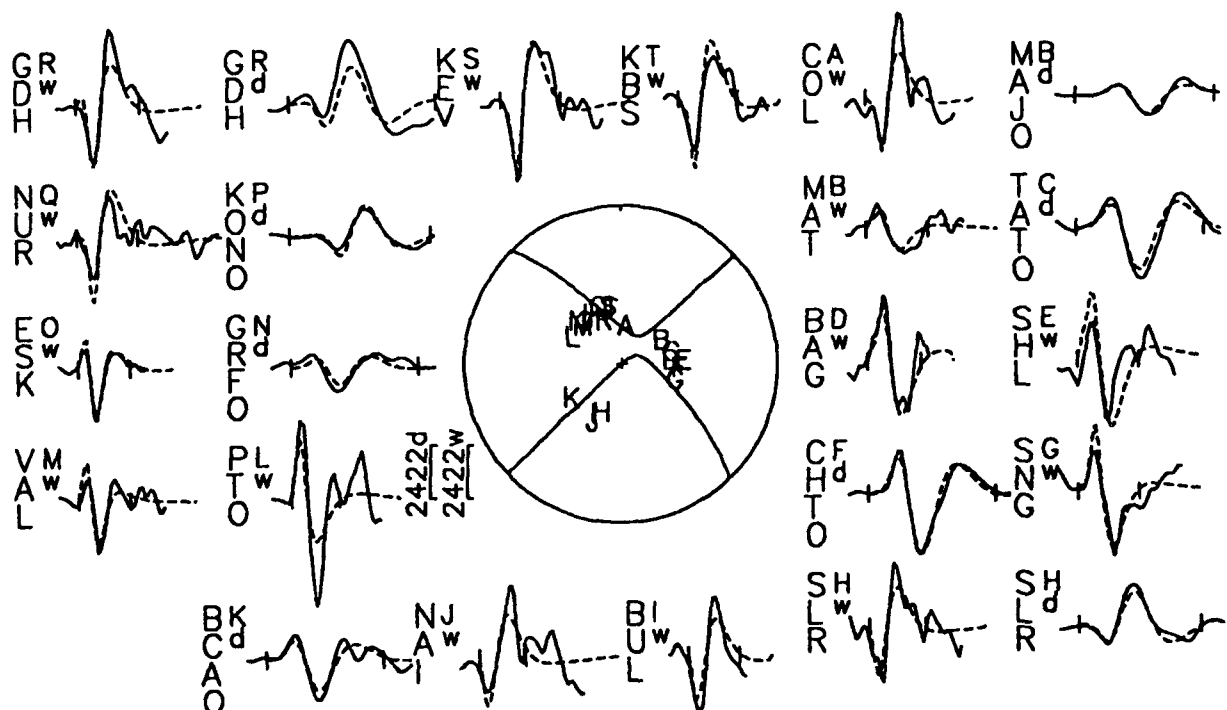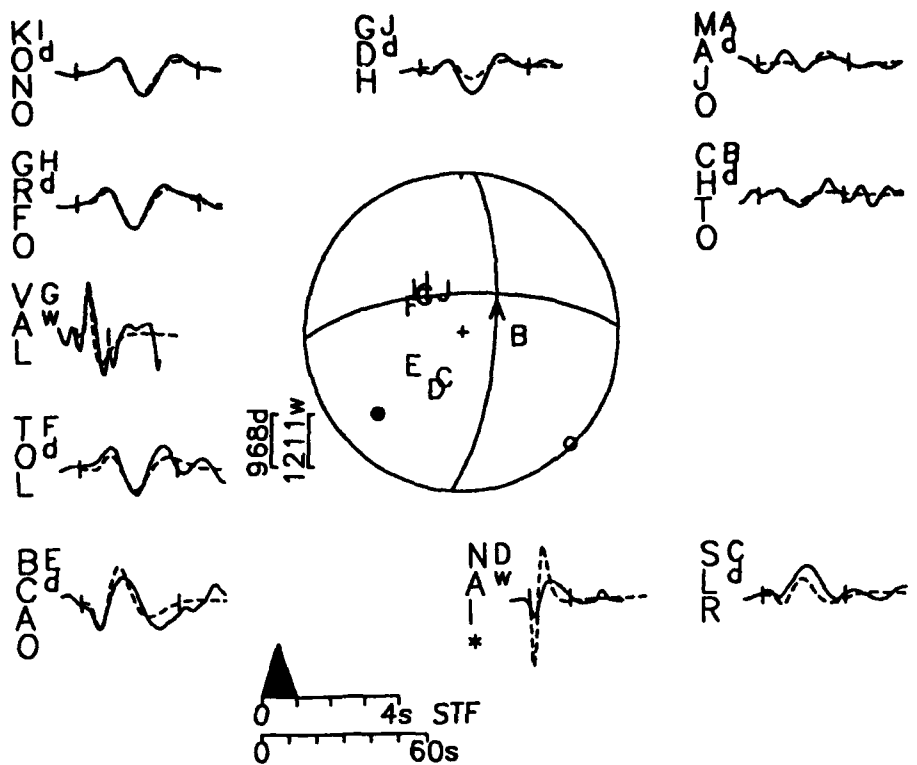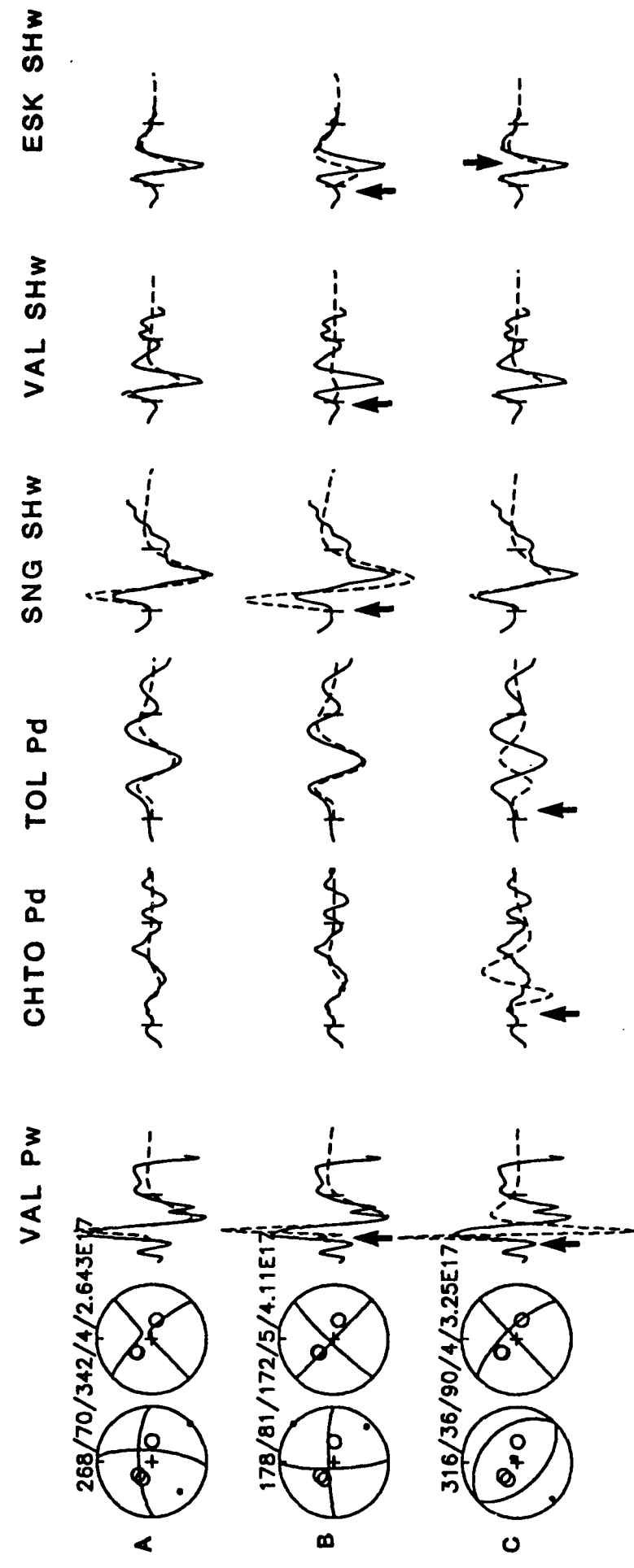
20 December 1986 mb:5.5
344/65/163/8/1.12E17
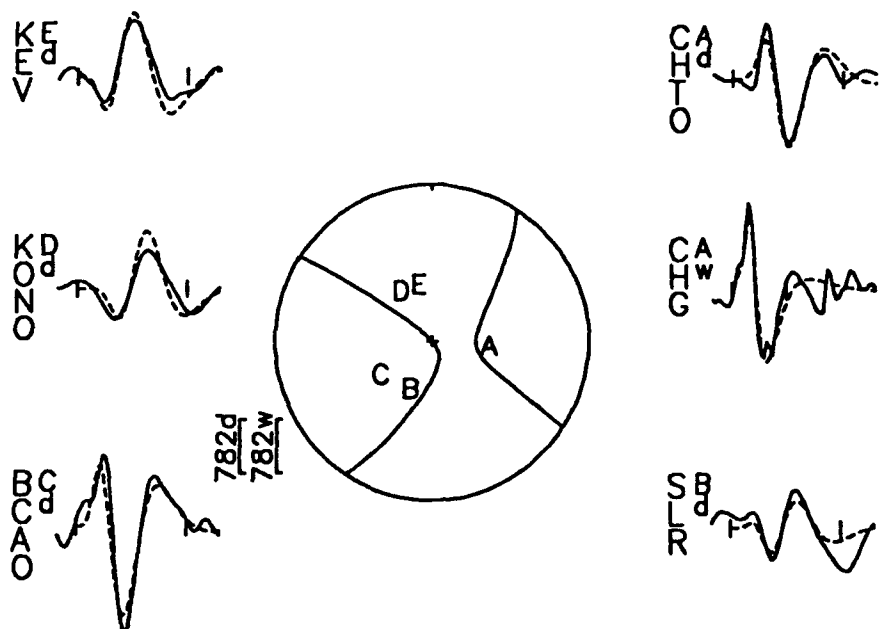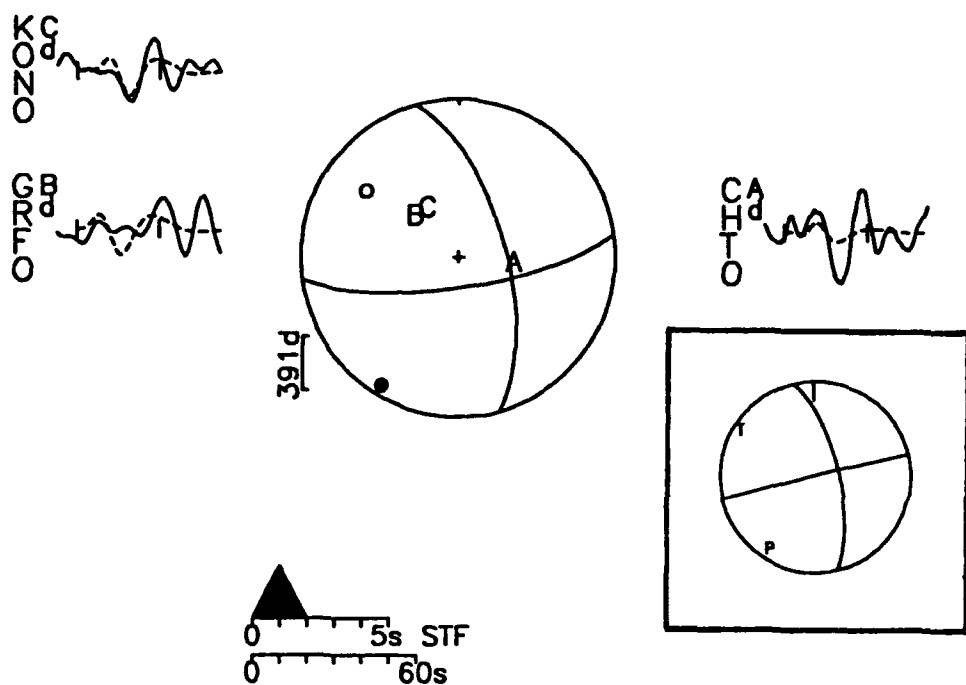
11 August 1988 16:00 mb:5.3
271/85/339/7/2.453E17
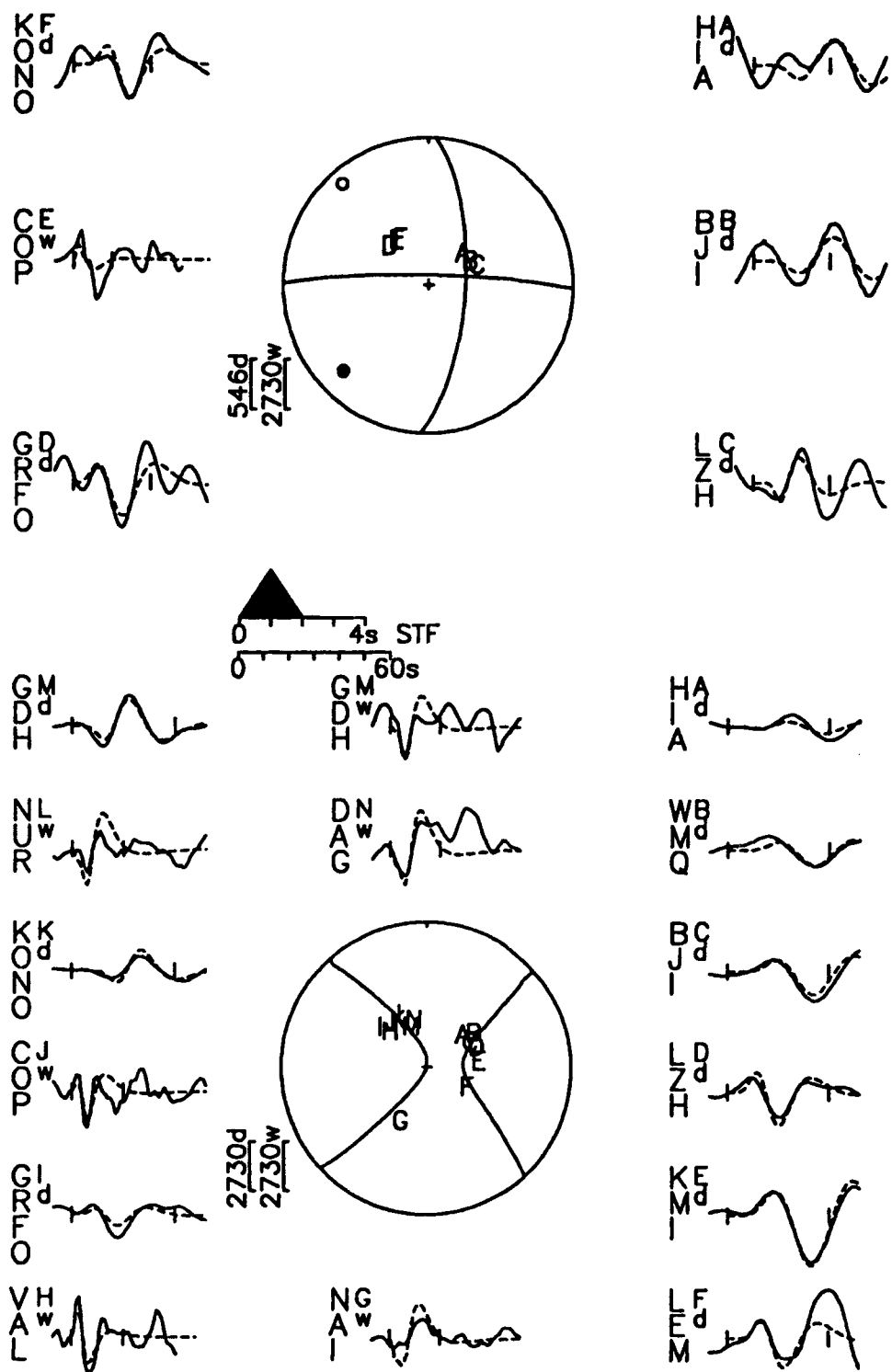
FIGURE A11

11 August 1988 16:00

LZH Pd   COP Pw   WMQ SHd   BJI SHd   COP SHw   GDH SHw

271/85/339/7/2.448E17

283/69/7/6/1.717E17

329/40/107/5/3.669E17

FIGURE A12

43
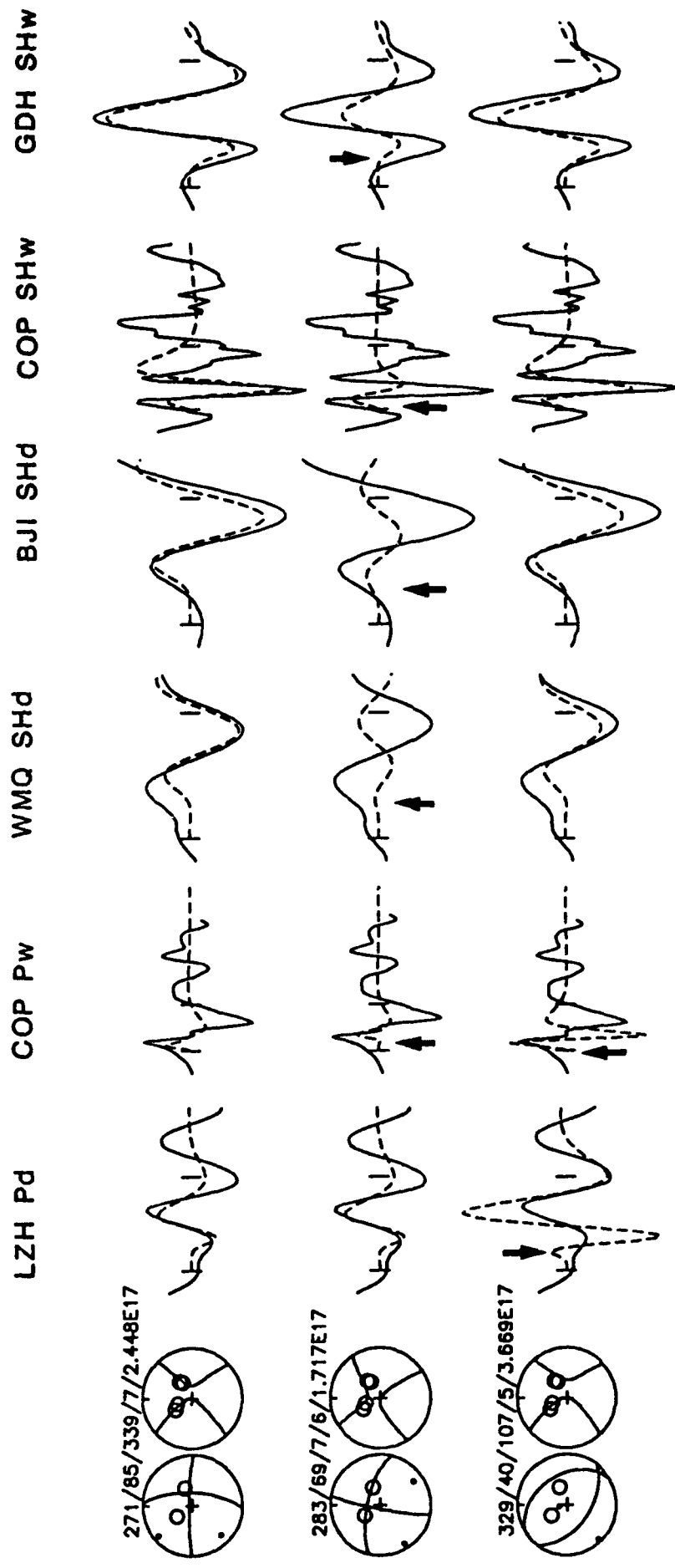
11 August 1988 16:04 mb:5.7
258/76/352/9/6.536E17

11 August 1988 16:04

BJI Pd   PTO Pw   GRFO Pd   KBS Pw   VAL SHw   GDH SHw

258/76/352/9/6.531E17

256/63/348/6/6.108E17

299/43/82/7/8.585E17

45
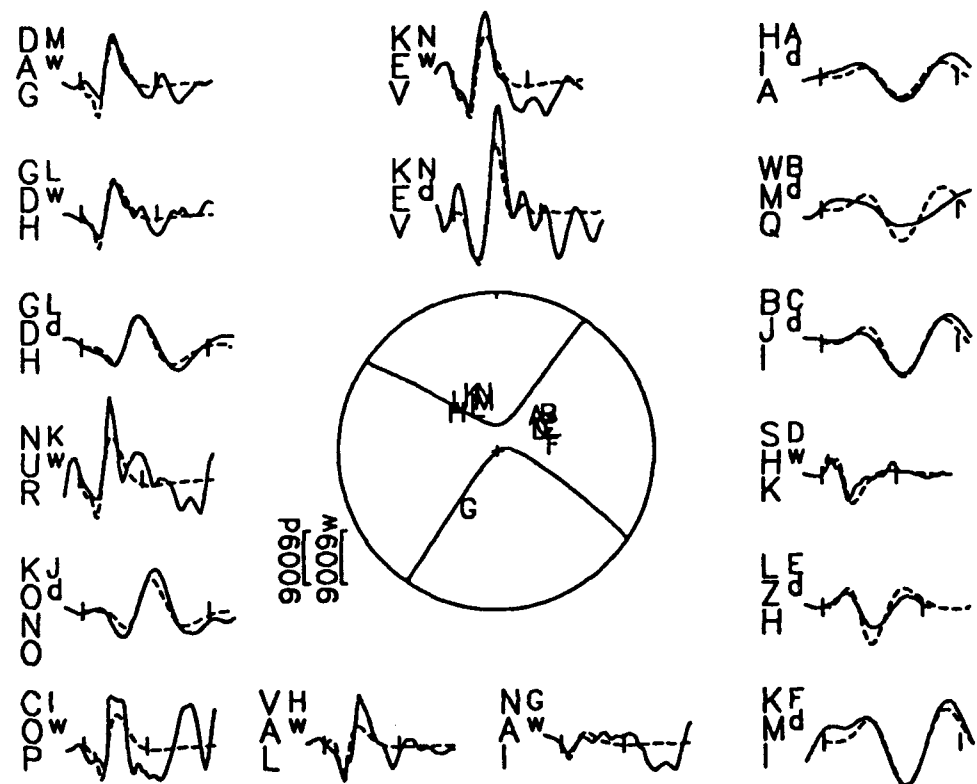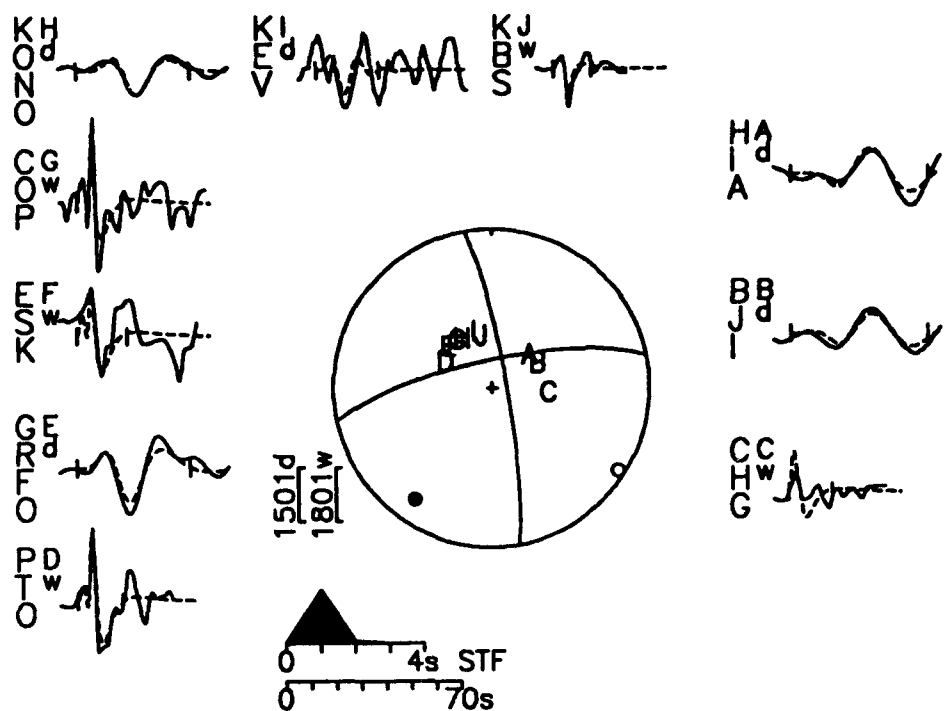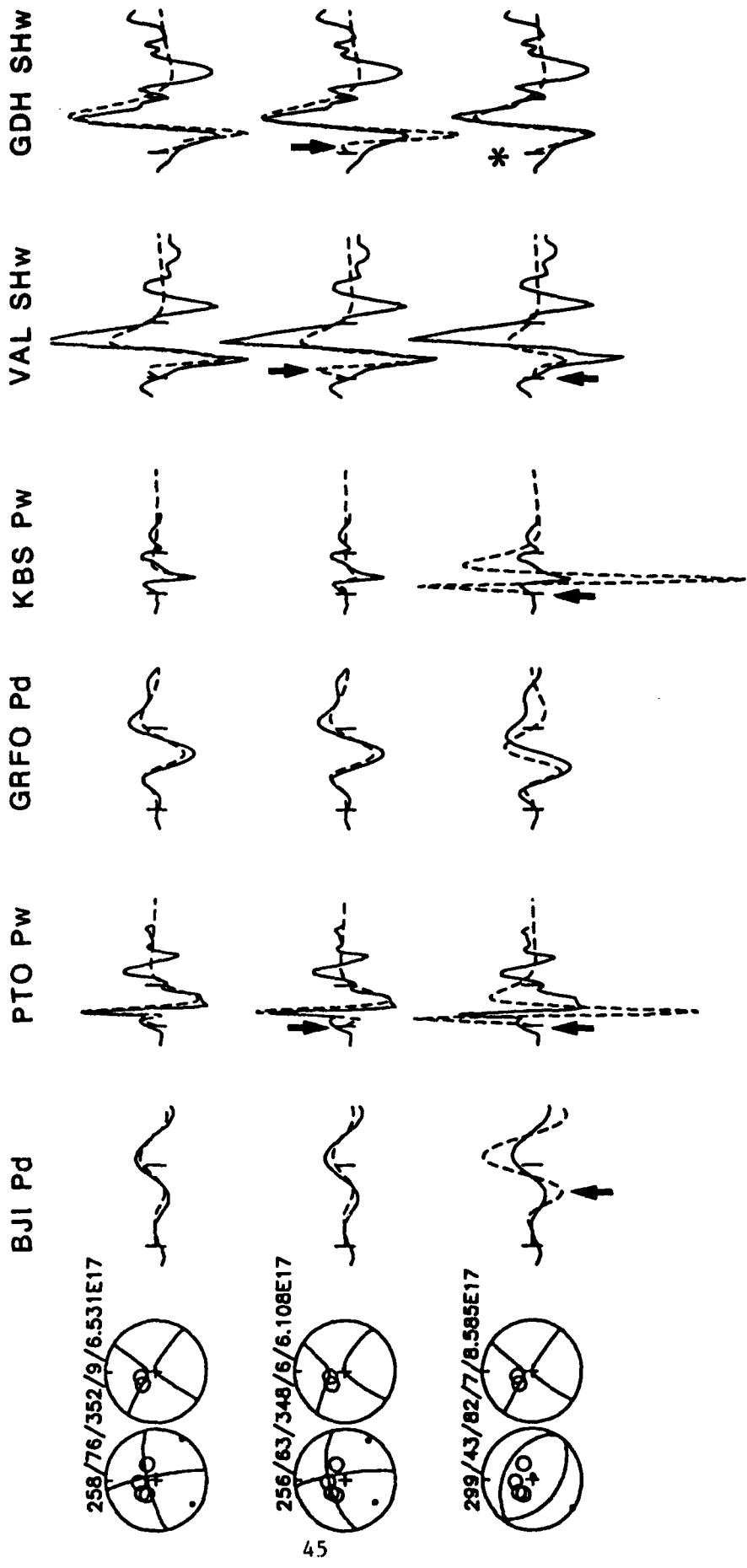
FIGURE A14

UPPER MANTLE VELOCITY STRUCTURE BENEATH THE SIBERIAN PLATFORM

Keith Priestley

Bullard Laboratories, University of Cambridge, Cambridge CB3 0EZ, UK

John Cipar

PL/GPEH, Hanscom AFB, Ma 01730, USA

1. INTRODUCTION

It is becoming increasingly clear that the upper mantle holds the key to a better understanding of the diversity of geologic processes observed at the Earth's surface, and that many of the important, unresolved questions concerning surface dynamics will be answered only when a more detailed picture of the upper mantle velocity structure and its lateral variations is obtained. For example, the continental lithosphere is much thicker than oceanic lithosphere, but the question of how thick a section of continent translates coherently during continental drift compared to oceanic lithosphere is still in question. The bottom of the low velocity zone is usually considered to coincide with the bottom of the athenosphere and it has been assumed that coherent translation of both old continental and oceanic plates takes place above about 200 km. However, this basic assumption of plate tectonics is contrary to ideas proposed by other studies [e.g., Lerner-Lam & Jordan, 1987] which suggest that the structure of the continents extends to upper mantle depths (400 km) implying that the continental lithosphere does not passively drift on the low-velocity athenosphere. In this paper, we investigate the velocity structure of the upper mantle beneath the Siberian Platform with emphasis on the nature of the mantle transition zone.

Understanding of the general features of the upper mantle has evolved over the past seventy years, but the details of upper mantle structure are still very much in question. Byerly [1926, 1935] first noted changes in slope of the P-wave travel time curve near 20° implying zones of more rapid velocity increase or velocity discontinuities in the upper mantle. Jeffreys [1936] determined the depth of the upper mantle velocity structure causing the 20° discontinuity to be 483±17 km. Niazi & Anderson [1965] suggested that the two discontinuities observed near 20° in the western North American travel time curve resulted from two upper mantle second-order velocity discontinuities at depths of 320 and 640 km. Regions of high velocity gradients near 400 km and 650 km depth are now universal features of upper mantle velocity models. The 400-km depth transition is thought to result from either the olivine-spinel phase transition [Ringwood, 1975] or from a chemical change from lherzolite to picritic eclogite [Anderson & Bass, 1986]. The 650-km depth transition is thought to result from the spinel-perovskite plus magnesiowustite transition [Ito & Takahashi, 1989].

Other velocity discontinuities or regions of strong velocity gradient in the upper mantle have been proposed. In 1917 Galitizin proposed a discontinuity at 232 km depth and studies by Lehmann [1959, 1962, 1964] indicated the presence of a discontinuity under North America and Europe near 215 – 220 km. There are no important phase changes in the mantle near this depth [Ringwood, 1975]. This, in addition to the sharpness of the discontinuity, suggests that it may result from a chemical change, and Anderson [1979] suggested that it may be the boundary between depleted and fertile lherzolite or between perdotite and eclogite. The question of whether an additional discontinuity or zone of high

gradient is required near 520 km depth is an issue of current debate [Shearer, 1991; Cummins et al, 1992; Jones et al, 1992]. Seismic evidence for a 520-km discontinuity was found in several regional studies in the early 1970's [e.g., Helmberger & Wiggins, 1971; Simpson et al, 1974]. More recent regional studies, however, do not require this structure [e.g., Gomberg et al, 1989; Bowman & Kennett, 1990]. The notable exception is the study of Shearer [1991] which found global evidence for a 520-km depth feature. The 520 discontinuity, if it exists, may correspond to the $\beta - \gamma$ olivine transition [Bina, 1991] but high pressure experiments [Weidner et al, 1984] suggest that this transition occurs over a broad depth range and would not create the velocity contrast required to explain the seismic data. Ita & Stixrude [1992] suggest that it may result from the dissolution of garnet to Ca-perovskite. The variety of evidence for and against the 200 and 520 km discontinuities may result from both of them being regional features.

Seismic data is the only means by which one can map the lateral extent of the upper mantle discontinuities and examine their depth and thickness variation. Most models of upper mantle velocity structure are derived from studying earthquake travel times and waveforms. A variety of source time functions are used in earthquake body wave studies and this requires comparing different waveforms or solving for the earthquake source, both resulting in possible ambiguities between velocity structure and earthquake source mechanism. Most of these studies analyze long-period body waves or surface wave data which results in decreased resolution. In addition, analysis of earthquake data does not lead to a uniform sampling of distance. It is difficult with such data to examine the width of the transition zone discontinuities to a precision required to discriminate between the competing petrologic models.

During the past 30 years, the Soviet Ministry of Geology (now the Center for Regional Geophysical and Geoecological Research) has conducted an extensive seismic exploration program of the Eurasian crust and upper mantle using explosion sources. Many of these profiles use nuclear explosions as seismic sources for recording long distance profiles (up to about 4000 km) and chemical explosives for recording shorter distance profiles (up to about 750 km) [Scheimer & Borg, 1984; Benz et al., 1992]. The energetic sources used on several DSS profiles have permitted interpretation of velocity structure to upper mantle depths. Yegorkin et al. [1977] describe a forward modelling procedure by which travel times are computed for successively deeper penetrating rays and the theoretical travel times for a proposed structure are compared with the observed travel times until they fit to within prescribed error limits (about 0.3 - 0.5 sec). Russian seismologists have considered wave amplitudes by comparing observed seismic amplitudes with the density of computed rays. Results for only a few of these profiles are discussed in the western literature [e.g., Yegorkin & Pavlenkova, 1981; Pavlenkova & Yegorkin, 1983; Egorkin et al., 1984; Mechie et al, 1993] and until recently, none of these data have been available to western seismologists. In this paper we discuss the analysis of one profile recorded across the Siberian Platform.

.. THE RIFT PROFILE

The 1982 "RIFT" profile extends 2600 km across the Archean-Proterozoic Siberian Platform from the Yamal Peninsula in NW Noril'sk to the Mongolian border SE of Lake Baikal (Fig. 1). Seismic data were recorded from three nuclear explosions and thirty-four chemical explosions along this profile. The northernmost portion of the profile crosses the West Siberian rift which developed during the initial breakup of Pangea in Triassic time

(235 – 215 my) [Aplonov, 1988]. Following the cessation of extension, the rift was buried beneath approximately 15 km of sediment. Geochemical analysis of the basalts within the rift indicates that they have a chemical composition similar to ocean tholeiites. The central section of the profile extends across the Tunguska Basin, the site of the Siberian Traps flood basalts. These flows possibly represent the largest Mesozoic occurrence of continental flood basalt, and now cover an area of about $3.4 \times 10^5 km^2$. They had a probable original volume in excess of $1.5 \times 10^6 km^3$ [Zolotukhin & Al'Mukhamedov, 1988]. The period over which this outpouring occurred is an issue of current debate. Baksi & Farrar [1991] argue from $^{40}Ar/^{39}Ar$ incremental-heating studies that volcanism occurred over a 5 to 10 million year duration, much longer than the duration of the Deccan Traps or Columbia River flood basalts and inconsistent with a mantle plume origin. On the other hand, Renne & Basu [1991] argue from laser-heating $^{40}Ar/^{39}Ar$ data that the basalts were erupted over a time interval of 900,000±800,000 years, which is similar to the duration of better dated flood basalts, thus giving eruption rates consistent with a plume origin. There is no evidence for crustal rifting prior to the initiation of volcanism [Marenko, 1977] as has been observed in other areas of continental flood basalts [White & McKenzie, 1989] nor is there a clear connection between the Siberian Traps and a mantle hot spot although Morgan [1981] has suggested an association with the Jan Mayen hot spot. If the Siberian Traps were associated with a mantle plume, it has long since passed. The southern portion of the profile crosses the presently active Baikal rift [Golenetsky & Misharina, 1978; Doser, 1991a,b] which follows the suture zone between the Siberian platform and the Saiyan-Baikal fold belt to the southeast. The Baikal Rift occurs within a broad, recent regional uplift and is characterized by high heat flow and a low velocity upper mantle [Belousov et al, 1991].

The northernmost nuclear shot (SP245 – Fig. 1.) is located within the West Siberian rift (latitude 69.206°N, longitude 81.647°E). We discuss data only from SP245 in this study. Data for this shot was recorded to more than 2400 km distance to the SE, and 165 km to the NW. The central nuclear shot point (SP173 – Fig. 1) is in western Tura within the Tunguska Basin, approximately 700 km southeast of SP245. Recordings from this shot extend 560 km northwest reversing a section of the profile from SP245 and 1700 km southeast across the Baikal rift. The southernmost nuclear shot point (SP35 – Fig. 1) is located 250 km NW of Lake Baikal. Recordings from this shot extend 325 km to the south across the Baikal rift and nearly 2200 km to the north reversing both SP245 and SP173. Body wave magnitudes for the three nuclear explosions range from 5.0 to 5.2 and are observable on low-noise, high gain teleseismic stations. In addition to the nuclear explosions, a detailed system of crustal observations was made using chemical explosions (3000 – 5000 Kg each) detonated at approximately 70 to 100 km intervals along the profile. The length of the reversed profiles from the chemical explosion recordings is about 300 km. The data from the chemical explosions and from SP173 and SP35 will be the subject of a future study.

SP245 was recorded at 182 sites each equipped with the "Taiga" seismic system [Chichinin et al., 1969]. These instruments record six analogue data channels and a radio time signal. Three components were recorded, but only the vertical component is available and discussed here. Each channel is recorded at high and low gain to increase the dynamic range. The sensors used have a natural frequency of 1.5 Hz and the recording system has a usable bandwidth between 0.5 – 20 Hz. Data for these profiles were obtained in the form of large paper record sections (25 mm/sec × 2.5 mm/km) with station locations accurate to 0.1 km. This is lower than the accuracy of station locations for most modern crustal refraction studies but because the source location is accurately known, the source – receiver distances are much more accurate than in most mantle studies using earthquake data. The

paper record sections were plotted using the high gain channel for the first arrival and, if necessary, the low-gain channel for the remainder of the seismogram. An overlap of 1-3 seconds allowed most traces to be rescaled with proper relative amplitude. The traces were commercially digitized and corrected for amplitude scaling to produce trace normalized record sections. The record section for SP245 is shown in Fig. 2.

Crustal phases are prominent at near distance ranges. The large, low velocity phase observed to about 180 km distance is the Rg phase. Pg is a prominent first arrival to about 200 km distance and large amplitude second arrival to about 280 km distance. The mantle phase Pn becomes the first arrival at an epicentral distance of about 190 km. It appears as a weak arrival in Fig. 2 but is clearly seen in the digital data. The apparent upper mantle velocity is 8.25 kms^{-1} based on fitting a straight line to first arrivals in the 200 600 km range. At longer ranges, the first arrivals appear to have variable amplitudes and arrival times. We believe that some of these reflect real variations in the lithospheric structure since they can be correlated over several hundred kilometers. A strong second arrival about three seconds after the low-amplitude first arrival appears at about 750 km distance. This phase is particularly prominent between 800 and 1000 km distance and becomes a first arrival by about 1200 km distance. Another high amplitude second arrival begins about three seconds after the first arrival at 1100 km, progressively moves forward and becomes the first arrival at about 1500 km. Their apparent velocities vary between 7.5 and 9.5 kms^{-1}. This shingling pattern is consistent with reflected phases from high velocity layers, indicating complex layering within the upper mantle [Hirn et al, 1973]. At least some of these observations may be due to lateral variations in structure.

Arrivals from the mantle transition zone can be observed at longer ranges. From 1600 to 2400 km a strong phase follows the first arrivals by 10 seconds at the shortest distance ranges and becomes the first arrival at the end of the record section. This phase is particularly prominent starting at about 1700 km range and is associated with a discontinuity or zone of high gradient near 400 km depth. There is another strong second arrival following the first arrival by about 12 seconds beginning at about 2100 km range. This is a reflection from the 660-km discontinuity. There is no clear evidence of the 520-km discontinuity described by Shearer [1991], although the seismograms in the corresponding distance range (< 2100 km) are complex and arrivals from a weak discontinuity in this depth range may be lurking within the record section.

3. DEVELOPMENT OF THE UPPER MANTLE VELOCITY MODEL

There is clear evidence in Fig. 2 for the presence of significant structure within the upper mantle and some of this structure may be 3-D. However, we have constructed a 1-D velocity model that fits the major travel time and amplitude features of Fig. 2 using a combination of travel time and synthetic seismogram modelling. Our objective is to produce a representative velocity structure for the mantle beneath the stable Siberian Platform that we can compare with upper mantle models from other stable regions, use as a reference model in future studies of the lateral variations in mantle structure, and eventually test the transition zone predictions from high pressure experimental petrology.

We previously read first and prominent later arrival times for the data from shot point SP245 from the original record section, and these data are discussed in the preliminary study of Cipar et al [1993]. Their velocity model (here designated Model A) from travel time modelling is taken as the starting model in this study. In constructing our new model

49

we first computed reflectivity [Fuchs & Muller, 1971] synthetic seismograms for the starting model and compared these with the broad features correlated across a number of observed seismograms. We then perturbed the model from the top down, starting with the structure at about 100 km depth, and through a process of trial and error fitting of the travel times and amplitudes, progressively worked our way down through the upper mantle. We have attempted to maintain as smooth a model as possible which produced synthetic seismograms consistent with the major features of the data. The attenuation model used in computing the synthetic seismograms was adapted from Der et al. [1986].

The results of this analysis is shown in Figs. 3, 4, and 5. Fig. 3 displays our new upper mantle model (Model T, Table 1) derived for SP245 on the left (panel a); on the right (panel b), the observed arrival times are shown superimposed on the calculated travel time curves for Model T. The letters serve as a guide as to what part of the velocity-depth function produces a given branch of the travel time curve. Observed (upper panel) and Model T synthetic (lower panel) record sections are shown in Fig. 4. Superimposed on both record sections are the observed arrival times (small dots) and theoretical travel time curves. The observed and theoretical seismograms have been bandpass filtered between 0.2 to 1.25 Hz to suppress scattered noise. The synthetics were computed as the delta function response of the medium and convolved with an Von Seggren-Blandford explosion source time function using k = 3, and b = 3 [Von Seggren & Blandford, 1972]. Fig. 5 shows an enlargement of the distant part of the record section along with synthetics and travel time curves for Model A [Cipar et al, 1993]. In the discussion that follows, we will refer to Figs. 3 and 4 together to illustrate the salient features of Model T.

The crustal velocity structure is taken from an unpublished study of refraction data recorded from chemical explosions in the vicinity of SP245. From these studies, we know that the crustal structure varies laterally along the profile. SP245 was detonated in a large sedimentary basin. Russian models for the crust along this profile are complex, but the crystalline crust can be divided roughly into three layers with P-wave velocities ranging from 6.1 to 6.4 kms^{-1} in the upper layer, 6.5 to 6.8 kms^{-1} in the intermediate layer, and 6.8 to 7.3 kms^{-1} in the lower layer. The lateral variations of the thickness of the crystalline crust are mostly due to variations in the thickness of the intermediate and lower layers. If the low velocity material at the surface of Model T is replaced with 6.0 kms^{-1} material, the travel times would be advanced by approximately 0.75 s. Therefore, this is the amount of variation in arrival time which might be expected from lateral variations in crustal structure along the profile. Variations in crustal structure will affect the depth estimates of mantle features but will not affect the form of these features.

The sub-Moho velocity determined from the first arrivals in the 200 – 600 km distance range is 8.25 kms^{-1}. The weak gradient from the Moho to 108 km depth is required to produce the weak first arrivals along the a-b branch (Fig. 3). The gradient is zero between 108 and 117 km depth in order to terminate the a-b branch by 1900 km. Between 117 and 123 km depth, the P-wave velocity increases sharply from 8.30 to 8.53 kms^{-1} This velocity increase produces the back branch of the triplication (b-c branch, Fig. 3). A reduced velocity gradient extends from 123 km (8.53 kms^{-1}) to 136 km (8.55 kms^{-1}) producing the forward branch c-d. The c-d branch is terminated by a velocity inversion from 136 km depth to 210 km depth. The sharpness of the velocity inversion is required to snuff out significant synthetic waveform energy which occurs after the end of the ray-theoretic travel time curve.

There is a second velocity increase between 233 and 235 km depth of 8.63 to 8.80 kms^{-1} This feature produces the second arrivals first observed at 1270 km distance and 11 sec

reduced time (f-g and g-h branches), and the first arrivals from about 1520 to 2400 km distance (h-i branch). This feature in the model is the top of a high velocity layer extending from 233 to 253 km depth, below which there is a broad low-velocity zone extending to 400 km depth. Arrivals from the earlier travel time branch from this feature become the first arrival at about 1520 km distance but terminate at about 1750 km distance. The strong velocity decrease between 253 and 260 km depth is required to terminate this branch (h-i branch). The weak first arrivals between 1760 and about 2400 km distance are the later branch (g-h) of the triplication due to this structure.

The second arrival starting at about 1600 km distance and 16 sec reduced time (Fig. 3) implies a significant velocity increase near 400 km depth. To model the strength and position of this arrival, we have included a velocity increase between 400 and 435 km depth of 8.64 to 9.45 kms^{-1} This phase is not observed at distances less than 1580 km. The model velocities above the 400 km transition zone are controlled by the travel times (j-k branch), and the velocity below the transition zone is controlled by the apparent velocity of the arrivals in the distance range 2000 - 2300 km (k-l branch). The relatively abrupt onset of this phase at 1580 km distance controls the thickness of the transition zone. The low amplitude arrivals at distances less than 1580 km seen in the synthetic record section would be masked by scattering due to lateral variations in the velocity structure on and above the transition zone.

The later arrival starting at about 2100 km distance and 13 - 14 sec reduced time are modeled as rays turning within a strong velocity gradient near 660 km depth. The depth of this feature in the velocity model is controlled by the differential travel time between this phase and the phase from the 400-km discontinuity, and the thickness of the 660-km transition zone is controlled by the extent of the phase to near distances.

Although the synthetic seismograms for Model T adequately fit the observed data, this alone does not provide insight into how well the major features of the velocity model are constrained. To estimate how well the model is constrained, we perturbed the depth and velocity of the major features until there was a noticeable degradation in the fit between the synthetic seismograms or travel times and thus placed bounds on these features. An example of this is shown in Fig. 5 which compares data to synthetics for Model A and Model T. As discussed above, we do not observe the "410" branch at ranges less than 1580 km (upper panel). The wide gradient zone of Model T (middle panel) between 400 and 435 km depth reproduces the strong arrival around 1800 - 2000 km range (9 - 18 sec reduced time). Our starting Model A, which has a first order discontinuity at 420 km depth predicts strong arrivals at ranges considerably less than 1580 km (lower panel), contrary to the observations.

We have assumed in this study that the upper mantle velocity structure is vertically stratified between the source and receiver, although we know this is not the case. For long-period body wave and surface wave studies this is a good approximation but the resolving power of long-period studies is limited by the relatively long wavelengths employed. Short period data increases the resolving power but is more susceptible to lateral heterogeneity and some of the increased complexity of upper mantle velocity models derived from short period data may result from mapping lateral heterogeneity into 1-D velocity models [Kennett & Bowman, 1990].

4. COMPARISON WITH OTHER TECTONICALLY STABLE REGIONS

Fig. 6 compares the P-wave velocity model for the upper mantle beneath the Siberian Platform with P-wave velocity models for several other tectonically stable regions. These models have been derived from analysis of waveform data, with the exception of the IASP91 model (panel a, dotted line) [Kennett & Engdahl, 1991] which is derived from the analysis of global travel time data. Model S25 (panel a, hatched line) was derived by LeFevre & Helmberger [1989] for the Canadian Shield using long-period body wave data recorded at WWSSN and Canadian network stations. Given & Helmberger [1980] developed model K8 (panel a, checked line) using observations of Soviet nuclear tests recorded primarily at European WWSSN stations. In panel b, Model T is compared to two recent models derived for the DSS QUARTZ profile by Mechie et al (1993). This profile is subparallel to the RIFT profile, approximately 1000 km to the west, and somewhat longer. Mechie at al., [1993] present models for two PNE's, referred to by them as the southern and northern shot points. Two velocity models for the Australian Shield are shown in Fig. 6. panel c. The NWB-1 model (hatched line in panel c) is from Bowman & Kennett [1990], and the CAPRI model (checked line in panel c) is from Leven [1985]. Both models were derived from modelling short period waveform data recorded along profiles across the Australian Shield from earthquakes in the Indonesian arc. Both similarities and differences can be seen in these comparisons. In particular, we will compare model features at depths near 210, 410, 520, and 660 km.

210-km discontinuity

Model T shows a rapid velocity increase starting at 210 km depth, followed by a velocity reversal at 253 km depth. Below this feature there is a low velocity zone extending to the depth of the 400-km discontinuity. A velocity increase near 220 km depth is a common feature in the upper mantle models for the Australian (Fig. 6c) and Asian (Fig. 6b) shield derived from short period (0.3 – 3.0 Hz) data, but is not observed in the upper mantle models for northwestern Eurasia and the Canadian Shield derived from long period (0.05 – 0.2 Hz) data. Goldstein et al. [1992] required a 3% velocity increase at 220 km depth to model broadband regional waveforms observed in Siberia. The velocity increase in their model represents the bottom of an upper mantle low velocity zone and below this there is an uniform velocity increase to the 400-km discontinuity. Upper mantle velocity models from the "QUARTZ" profile [Mechie et al., 1993] show a laminated structure at these depths below which there is a velocity decrease followed by a gradual increase in velocity to the 400-km discontinuity.

In general, upper mantle models derived from the analysis of short period or broadband data show much greater complexity in the 150 – 250 km depth range than do models derived from modelling long period waveform data. Part of this increased complexity may be the result of mapping lateral variations in the velocity structure into an apparent velocity variation with depth, but the similarity of the velocity models in this depth range supports the observed velocity complexity at these depths.

410-km discontinuity

The "410-km" discontinuity in Model T consists of a broad gradient zone from 8.64 to 9.45 kms^{-1} extending from 400 to 435 km depth. This extends to a greater depth than the "410-km" discontinuity in the IASP91 global model (410 km depth, Fig. 6a), for the Canadian Shield (405 km depth, Fig. 6a), and the models for the Australian Shield (400

km depth, Fig. 6c), but is similar in depth to that of the "410-km" discontinuity beneath the QUARTZ profile (420 km depth, Fig. 6b) and beneath K8 northwest Eurasia (420 km, Fig. 6a). King & Calcagnile [1976] found a similar depth for the "410-km" discontinuity beneath northwest Eurasia from modelling travel time data from Soviet PNE's recorded at the NOSAR array in southern Norway. Stangl [1990] estimated the depth of the "410-km" discontinuity to be about 440 km depth beneath the FINNOLORA profile in Sweden. Thus, all five studies find the "410-km" discontinuity to be somewhat deeper ($\approx 420 - 430$) beneath northern Eurasia than the global average.

However, the nature of this discontinuity beneath northern Eurasia differs between the profiles. The salient feature of the "410-km" discontinuity in Model T is that it is a broad high-gradient zone extending over 35 km in depth, rather than being a sharp discontinuity. The gradient is 0.02 km/s/km between 400 and 415 km depth, rising slightly to 0.025 km/s/km between 415 to 435 km depth. As discussed above, we feel that the synthetic seismogram calculations rule out a first order discontinuity because models with such a feature predict prominent arrivals at ranges less than 1580 km which are unobserved in the data. This observation has led us to adopt a broad transition region for the "410". Model K8 has a velocity gradient although of smaller extent than Model T, while the other models all have a first order discontinuity for the "410-km" discontinuity. Further analysis is required to ascertain whether this is the result of regional variation, or an artifact of the analysis.

520-km discontinuity

Shearer [1991] stacked long-period global digital seismograph network data and these showed evidence for arrivals between those coming from the 410-km and 660-km discontinuities. He suggested that these arrivals were reflections from a velocity discontinuity at 520 ± 4 km depth which had about half the velocity contrast of the 410-km discontinuity. The universality of this feature is a current issue of debate [i.e., Cummins et al, 1992; Jones et al, 1992]. Of the models shown in Fig. 6, only those of Mechie et al [1993] (QUARTZ profiles) shows a discontinuity in this depth range. On the other hand, Benz [personal communication] finds evidence for a 520-km discontinuity in only one of the shots of the QUARTZ profile but not the other. The lateral separation for the rays turning at these depths for the two shots of the QUARTZ profile is about 400 km, indicating that a 520 km deep feature may vary significantly over that distance range. Egorkin et al [1987] interpret travel time observations from two long DSS profiles in Siberia, one (RUBIN) perpendicular to the RIFT profile and passing south of shot point SP245, and one (METEOR) subparallel to the RIFT profile and approximately 500 km to the east. The velocity model for the RUBIN profile has a gradient from 9.66 to 9.91 km s^{-1} extending from 500 to 520 km depth. This is steeper than the gradient at depths above and below this range. The velocity model derived from travel time data recorded along the METEOR profile shows a smooth gradient extending between about 400 and 630 km depth. There is no compelling evidence from the RIFT profile data for a discontinuity in the depth range 500 to 550 km. This agrees with the travel time analysis results for the METEOR profile data [Egorkin et al, 1987] to the east of the RIFT profile but disagrees with waveform analysis results for the QUARTZ profile data [Mechie et al, 1993] to the west of the RIFT profile. Reflections from a discontinuity near 520 km depth would produce arrivals between the reflections from the 410-km and 660-km discontinuities, at distance ranges greater than about 1900 km, and would not be a clear first arrival within the distance range of our data. Seismograms in this

53

distance range along the RIFT profile are complex and arrivals from a weak discontinuity may be lurking within the record section.

660-km discontinuity

The 660-km discontinuity in Model T consists of a 3.5% velocity increase over the depth range 655 – 659 km. The velocity increase in Model T is somewhat smaller than in most other upper mantle models for tectonically stable regions. The depth of this feature is similar to that of many other models. Two notable exceptions are the Australian models (Fig. 6c). NWB-1 has a zone of strong gradient around 610 – 630 km depth with a 3.5% velocity increase. The CAPRI model exhibits significant complexity with two zones of high gradient; one at 610 – 625 km and a second at 690 – 720 km depth, separated by a low gradient zone. Variations in the structure of the 660-km discontinuity among these models may reflect differences in interpretational methods, as well as real differences in Earth structure.

5. CONCLUSIONS

We present a new 1-D compressional velocity model for the upper mantle beneath the Siberian Platform that is derived from modelling the observed travel times and relative amplitudes from the deep seismic sounding data recorded along the "RIFT" profile. The model should be regarded as preliminary since we have not included the effects of the known lateral variations in the velocity structure of the crust, nor have we made a comprehensive study of the data from the two southern shotpoints. As a result, it is possible that some of the fine details of the new model may result from mapping lateral velocity variations in the velocity structure into apparent velocity variations with depth [Kennett & Bowman, 1990].

The major features of our model are: (1) a sharp increase in velocity gradient between 210 and 235 km depth; (2) a broad high-gradient zone from 400 to 435 km depth; and (3) a narrow high-gradient zone between 655 and 659 km depth. The high-gradient zone between 210 and 235 km is clearly seen as a marked change in slope of the first arrival travel time curve and corresponds to the discontinuity first described by Lehmann (1959, 1962, 1964) which has been observed in many, but not all, continental regions. The regional occurrence of this feature suggests that it is related to large-scale, but geographically limited compositional changes and/or changes in rock fabric and not to a global-scale minerologic phase changes. The existence of high-gradient zones near 410-km and 660-km depth is well established on a global basis from a variety of studies. We observe a broad high-gradient zone at the "410 discontinuity" in comparison to first-order discontinuities or narrow zones of high-velocity gradient seen in other studies. Our primary evidence for the wide, high-gradient zone is the observed end of the "410-km" travel time branch at about 1580 km range. Models with first-order discontinuities predict that this branch should be observable to shorter ranges. Note in this context that the close station spacing of the DSS profiles (10 –15 km) allow a more precise measurement of the position of this and other travel time branches compared to the wide station spacing used in other studies. The "660-km discontinuity" of our model is in good agreement in depth, width and velocity contrast to other published models. Variations among the models probably reflect as much differences in interpretation technique as true variation within the Earth. Our model for the central Siberian platform do not have any feature corresponding to a classic low-velocity zone between 100 to 200 km depth. We infer several zones of lower velocity and/or reduced

54

gradient as a way of terminating high phase velocity travel time branches, but the data do not require a deep LVZ found in other models. Nor do the data require a discontinuity near 520 km depth. Like previous Earth models using DSS data, we observe and model considerably greater complexity in the lithosphere above 250 km depth than models derived from long-period, widely-spaced data sets.

In this study we have analyzed travel time and relative amplitude data from one shot point of the "RIFT" profile. From these data we have constructed a 1-D velocity-depth model which explains the dominant characteristics of the observations. The model also has features similar to those proposed in other upper mantle velocity models for tectonically stable regions. We intend to use this as a new reference model for further studies of lateral variations in the velocity structure of the lithosphere and upper mantle of Central Asia.

ACKNOWLEDGMENTS

REFERENCES

Anderson, D.L., 1979. The Deep Structure of Continents, *J. geophys. Res.*, **84**, 7555 – 7560.

Anderson, D.L., & Bass, J.D., 1986. Transition region of the Earth's upper mantle, *Nature*, **320**, 321 – 328.

Aplonov, S., 1988. An aborted Triassic ocean in west Siberia, *Tectonics*, **7**, 1103 – 1122.

Baksi, A.K., & Farrar, E., 1991. $^{40}Ar/^{39}Ar$ dating of the Siberian Traps, USSR: Evaluation of the ages of the two major extinction events relative to episodes of flood-basalt volcanism in the USSR and the Deccan Traps, India, *Geology*, **19**, 461 – 464.

Belousov, B., Pavlenkova, N.I., & Kvyatkovskaya, G.N., 1991. Crustal structure of the territory of the USSR (in Russian), Nauka, Moscow.

Benz, H.M., Unger, J.D., Leith, W.S., Mooney, W.D., Solodilov, L., Egorkin, A.V., & Ryaboy, V.Z., 1992. Deep Seismic Sounding in Northern Eurasia, *EoS*, **73**, 297 – 300.

Bina, C.R., 1991. Mantle discontinuities, *Reviews of Geophysics, supplement*, 29 783 – 793.

Bowman, J.R., & Kennett, B.L.N., 1990. An investigation of the upper mantle beneath northwestern Australia using a hybrid seismograph array, *Geophys. J. Int.*, **101**, 411 – 424.

Byerly, P., 1926. The Montana earthquake of June 28, 1925, *Bull. seism. Soc. Am.*, **16**, 209 – 265.

Byerly, P., 1935. The first preliminary waves of the Nevada earthquake of December 20,

1932, *Bull. seism. Soc. Am.*, **25**, 62 – 80.

Chichinin, I. S., Yegorov, G.V., Yemelianov, A.V., & Bochanov. A.J., 1969. Portable Telemonitored Seismic Equipment "Taiga," *Methods of Seismic Research*, Nauka, Moscow, 95 – 119.

Cipar, J.J, Priestley, K.F., Egorkin, A.V., & Pavlenkova, N.I., 1993. From rift to rift: The Yamal Peninsula - Lake Baikal deep seismic sounding profile, *Geophys. Res. Lett.*, **20**, 1631 – 1634.

Cummins, P.R., Kennett, B.L.N., Bowman, J.R., & Bostock, M.G., 1992. The 520 km discontinuity?, *Bull. seism. Soc. Am.*, **82**, 323 – 336.

Der, Z., Lees, A., & Cormier, V., 1986. Frequency dependence of Q in the mantle underlying the shield areas of Eurasia, Part III: The Q model, *Geophys. J. R. astr. Soc.*, **87**, 1103 – 1112.

Doser, D.I., 1991a. Faulting within the western Baikal rifts characterized by earthquake studies, *Tectonophysics*, **196**, 87 – 107.

Doser, D.I., 1991b. Faulting within the eastern Baikal rifts characterized by earthquake studies, *Tectonophysics*, **196**, 109 – 139.

Egorkin (Yegorkin), A.V., Ziuganov, S.K., & Chernyshev, N.M., 1984. The Upper Mantle of Siberia, *Proceeding of the 27th International Geological Congress*, **8**, 29 – 56.

Fuchs, K., & Muller, G., 1971. Computations of synthetic seismograms with the reflectivity method and comparison with observations, *Geophys. J. R. astr. Soc.*, **23**, 417 – 433.

Given, J.W., & Helmberger, D.V, 1980. Upper Mantle Structure of Northwestern Eurasia, *J. geophys. Res.*, **85**, 7183 – 7194.

Goldstein, P., Walter, W.R., & Zandt, G., 1992. Upper mantle structure beneath central Eurasia using a source array of nuclear explosions and waveforms at regional distance, *J. geophys. Res.*, **97**, 14097 – 14113.

Golenetsky, S.I., & Misharina, L.A., 1978. Seismicity and earthquake focal mechanisms in the Baikal rift zone, *Tectonophysics*, **45**, 71 – 85.

Gomberg, J.S., Priestley, K.F., & Brune, J.N., 1989. The compressional velocity structure of the crust and upper mantle of northern Mexico and the border region, *Bull. seism. Soc. Am.*, **78**, 1496 – 1519.

Helmberger, D.V., & Wiggins, R.A., 1971. Upper mantle structure of the midwestern United States, *J. geophys. Res.*, **76**, 3229 – 3245.

Hirn, A., Steinmetz, L., Kind, R., Fuchs, K., 1973. Long range profiles in Western Europe II-Fine structure of the lower lithosphere in France (Southern Bretagne), *J. Geophys.*, **39**, 363 – 384.

Ita, J., & Stixrude, L., 1992. Petrology, elasticity, and composition of the mantle transition

zone, *J. geophys, Res.*, **97**, 6849 – 6866.

Ito, E, & Takahashi, E., 1989. Postspinel transformations in the system Mg$_2$SiO$_4$-Fe$_2$SiO$_4$ and some geophysical implications, *J .geophys. Res.*, **94**, 10637 – 10646.

Jeffreys, H., 1936. The structure of the Earth down to the 20° discontinuity, *Mon. Not R. astr. Soc. Geophys. Suppl.*, **4**, 401 – 422.

Jones, L.E, Mori, J., & Helmberger, D.V., 1992. Short period constraints on the proposed transition zone discontinuity, *J. geophys. Res.*, **97**, 8765 – 8774.

Kennett, B.L.N., & Bowman, J.R., 1990. The velocity structure and heterogeneity of the upper mantle, *Phys. Earth planet. Inter.*, **59**, 134 – 144.

Kennett, B.L.N., & Engdahl, E.R., 1991. Traveltimes for global earthquake location and phase identification, *Geophys. J. Int.*, **105**, 429 – 465.

King, D. W. & Calcagnile, G., 1976. P-wave Velocities in the Upper Mantle Beneath Fennoscandia and Western Russia, *Geophys. J. R. astr. Soc.*, **46**, 407 – 432.

LeFevre, L.V., & Helmberger, D.V., 1989. Upper mantle P-velocity structure of the Canadian shield, *J. geophys. Res.*, **94**, 17749 – 17766.

Lehmann, I, 1959. Velocities of longitudinal waves in the upper part of the Earth's mantle, *Ann. Geophys.*, **15**, 93 – 118.

Lehmann, I., 1962. The travel times of the longitudinal waves of the Logan and Blanca atomic explosions and their velocities in the upper mantle, *Bull. seism. Soc. Am.*, **52**, 519 – 526.

Lehmann I., 1964. On the travel times of P as determined from nuclear explosions, *Bull. seism. Soc. Am.*, **54**, 123 – 139.

Lerner-Lam, Arthur L. & Jordan, T.H., 1987. How thick are the continents?, *J. geophys. Res.*, **92**, 14007 – 14026.

Leven, J.H., 1985. The application of synthetic seismograms to the interpretation of the upper mantle P-wave velocity structure in northern Australia, *Phys. Earth planet. Inter.*, **38**, 9 – 27.

Marenko, G.F., 1977. The epoch of Triassic trap magmatism in Siberia, *Int. Geol. Rev.*, **19**, 1089 – 1100.

Mechie, J., Egorkin, A.V., Fuchs, K., Ryberg, T., Solodilov, L., & Wenzel, F., 1993. P-wave mantle velocity structure beneath northern Eurasia from long-range recordings along the profile Quartz, *Phys. Earth planet. Inter.*, **79**, 269 – 286.

Morgan, W.J., 1981. Hotspot tracks and the opening of the Atlantic and Indian Oceans, in *The Sea*, C. Emiliani, Ed., Wiley-Interscience, New York, 443 – 487.

Niazi, M., & Anderson, D.L., 1965. Upper mantle structure of western North America from

apparent velocities of P waves, *J. geophys. Res.*, **70**, 4633 – 4640.

Pavlenkova, N.I. & Yegorkin, A.V., 1983. Upper Mantle Heterogeneity in the Northern Part of Eurasia, *Phys. Earth planet. Int.*, **33**, 180 – 193.

Renne, P.R., & Basu, A.R., 1991. Rapid eruption of the Siberian Traps flood basalts at the Permo-Triassic boundary, *Science*, **253**, 176 – 179.

Ringwood, A.E., 1975. *Composition and Petrology of the Earth's Mantle*, 604pp, McGraw-Hill, New York.

Scheimer, J.F. & Borg, I.Y., 1984. Deep seismic sounding with nuclear explosives in the Soviet Union, *Science*, **226**, 787 – 792.

Shearer, P.M., 1991. Constraints on upper mantle discontinuities from observations of long-period reflected and converted phases, *J. geophys. Res.*, **96**, 18147 – 18182.

Simpson, D.W., Mereu, R.F., & King, D.W., 1974. An array study of P-wave velocities in the upper mantle transition zone beneath northeastern Australia, *Bull. seism. Soc. Am.*, **64**, 1745 – 1788.

Von Seggren, D., & Blandford, R., 1972. Source time functions and spectra for underground nuclear explosions, *Geophys. J. R. astr. Soc.*, **31**, 83 – 97.

Weidner, D.J., Sawamoto, H., Sasaki, S., & Kurnazawa, M., 1984. Single-crystalelastic properties of the spinel phase of Mg_2SiO_4, *J. geophys. Res.*, **89**, 7852 – 7860.

White, R.S., & McKenzie, D.P., 1989. Magmatism at rift zones: The generation of volcanic continental margins ans flood basalts, *J. geophys. Res.*, **94**, 7685 – 7729.

Yegorkin, A.V., Ryaboy, V.Z., Starobinets, L.P., & Druzhinin, V.S., 1977. Velocity Cross Sections of the Upper Mantle from DSS Data on Land, *Izvestiya, Earth Physics*, **13**, 467 – 477.

Yegorkin, A.V. & Pavlenkova, N.I., 1981. Studies of Mantle Structure of U.S.S.R. Territory on Long-range Seismic Profiles, *Phys. Earth planet. Inter.*, **25**, 12 – 26.

Zolotukhin, V.V., & Al'Mukhamedov, A.I., 1988. Traps of the Siberian Platform, in *Continental Flood Basalts*, J.D. Macdougall, Ed. Kluwer Academic Publishers, Dordrecht, Netherlands, 273 – 310.

Table 1. Central Siberian Model T

Depth (km)	P-wave Velocity (kms^{-1}	Depth (km)	P-wave Velocity (kms^{-1}
0.0	3.50	233.0	8.63
11.0	5.10	235.0	8.80
11.0	6.35	253.0	8.85
19.8	6.35	260.0	8.62
19.8	6.60	295.0	8.62
24.8	6.60	330.0	8.63
24.8	7.30	370.0	8.63
44.0	7.30	400.0	8.64
44.0	8.25	415.0	8.95
50.0	8.26	435.0	9.45
75.0	8.27	542.5	9.75
108.0	8.30	655.0	10.25
117.0	8.30	659.0	10.62
123.0	8.53	800.0	10.98
136.0	8.55	900.0	11.15
145.0	8.50	1000.0	11.40
210.0	8.51		

FIGURE CAPTIONS

Figure 1. Simplified tectonic map of Central Asia. The "RIFT" profile is marked by the heavy solid line and large solid dots denote the locations of the three nuclear explosions detonated along the profile. Only seismograms from the SP245 explosion (the northernmost shot point) are discussed in this study.

Figure 2. Observed, unfiltered SP245 record section plotted at a 8.2 kms^{-1} reduction velocity. Seismograms are trace normalized.

Figure 3. (a) P-wave velocity depth function for SP245 Model T. (b) Theoretical travel time curves for Model T superimposed on observed SP245 arrival times. In both panels, small letters indicate travel time curve branches and corresponding segments of the velocity depth function.

Figure 4. (a) Record-section of the data recorded SE along the "RIFT" profile from SP245. The time has been reduced by $\Delta/8.2$ seconds. The seismograms have been bandpass filtered between 0.2 and 1.25 Hz, and the amplitudes are trace normalized. (b) Reflectivity synthetic seismogram record-section of for the Siberian Platform upper mantle Model T. The travel time data are indicated (open circles first arrivals; triangles secondary arrivals). Solid lines on both panels are travel time curves computed for Model T.

Figure 5. Enlargement of Fig. 4 in the 1200 – 2400 km distance range.

Figure 6. Comparison of the Siberian Platform upper mantle compressional wave velocity model derived from the data of Fig. 2, with upper mantle compressional wave velocity models for several other tectonically stable regions derived from modelling waveform data. (a) Comparison of Model T (solid line) and models K8 (checkered line) [Given & Helmberger, 1980] for northwest Eurasia, S25 (hatchered line) [LeFevre & Helmberger, 1989] for the Canadian Shield, and the global model IASP91 (dotted line) [Kennett & Engdahl, 1991]. K8 and S25 were both derived from waveform modelling primarily long-period records from a dispersed array of stations for nuclear explosions (K8) or earthquakes (S25) and thus average mantle structure over broad regions. IASP91 is derived from global travel time data. (b) Comparison of Model T (solid line) with models QUARTZ-n (dashed line) and QUARTZ-s (dotted line)for northern Eurasia [Mechie et al, 1993]. These models are derived from data similar to that recorded for the RIFT profile, but are recorded along a subparallel profile about 1000 km to the west. (c) Comparison of Model T (solid line) with models CAPRI (dashed line) [Leven, 1985] and NWB-1 (dotted line) [Bowman & Kennett, 1990] for the Australian Shield. Both Australian models were derived from modelling short period waveform data recorded along profiles across the A stralian Shield from earthquakes in the Indonesian arc.
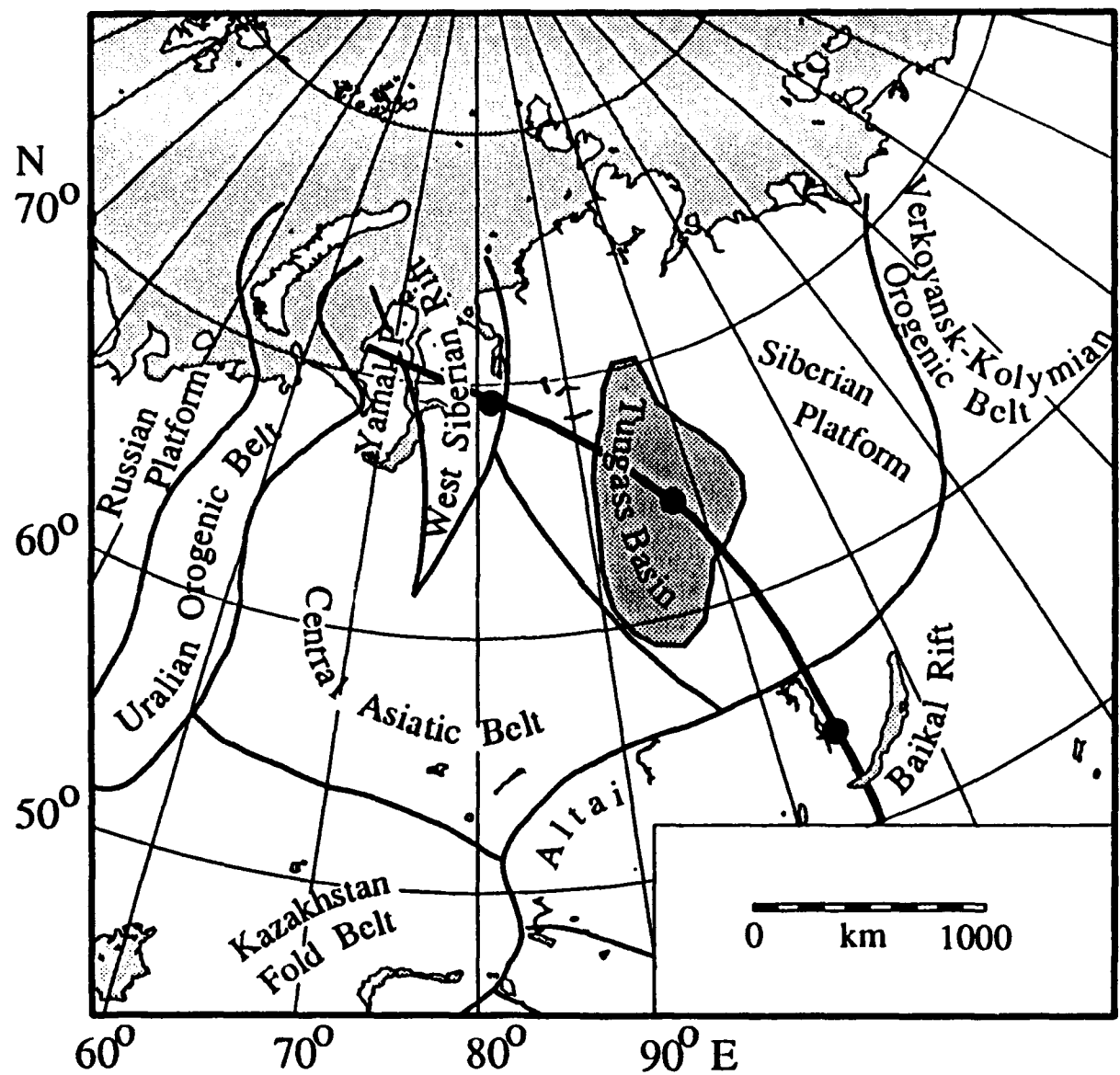
FIGURE 1
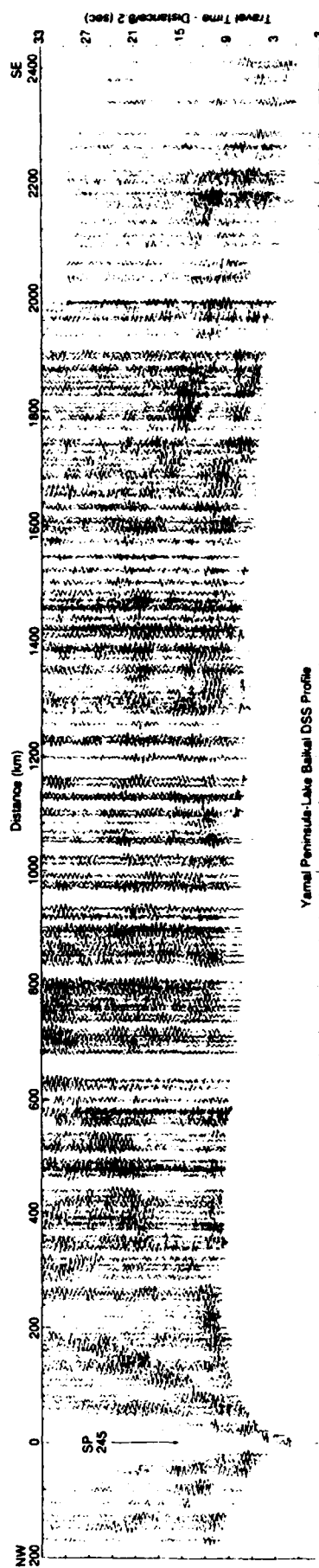
Yamal Peninsula-Lake Baikal DSS Profile

FIGURE 2

SP245 - Model T Travel Times

(b)

SP245 Model T

(a)

FIGURE 3

63

FIGURE 4.

FIGURE 5

65

(a) Upper Mantle Models

SP245-T
IASP91
S25
K8

(b) DSS Upper Mantle Models

SP245-T
Quartz-N
Quartz-S

(c) Australian Shield Models

SP245-T
NWB-1
CAPRI

Depth (km)

P-Wave Velocity (km/sec)
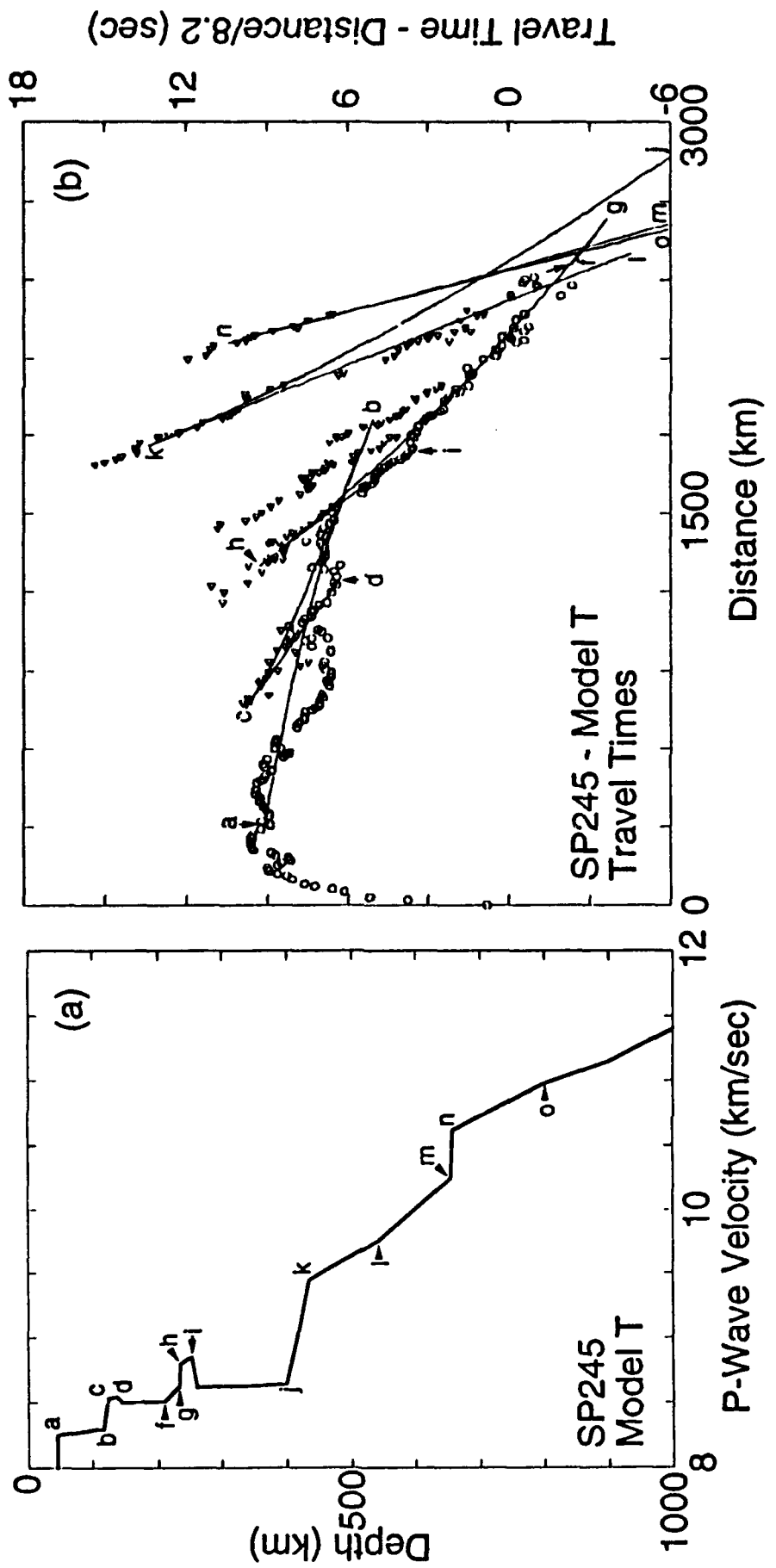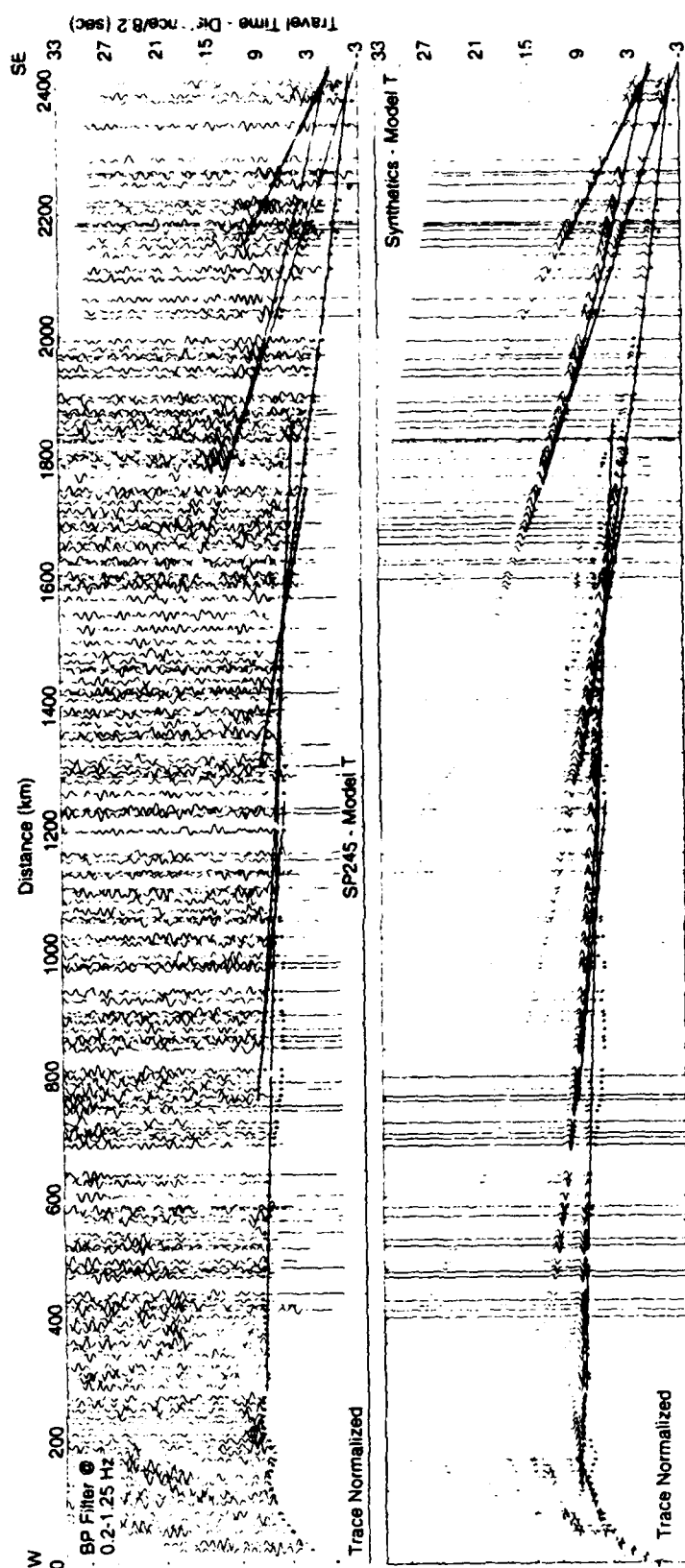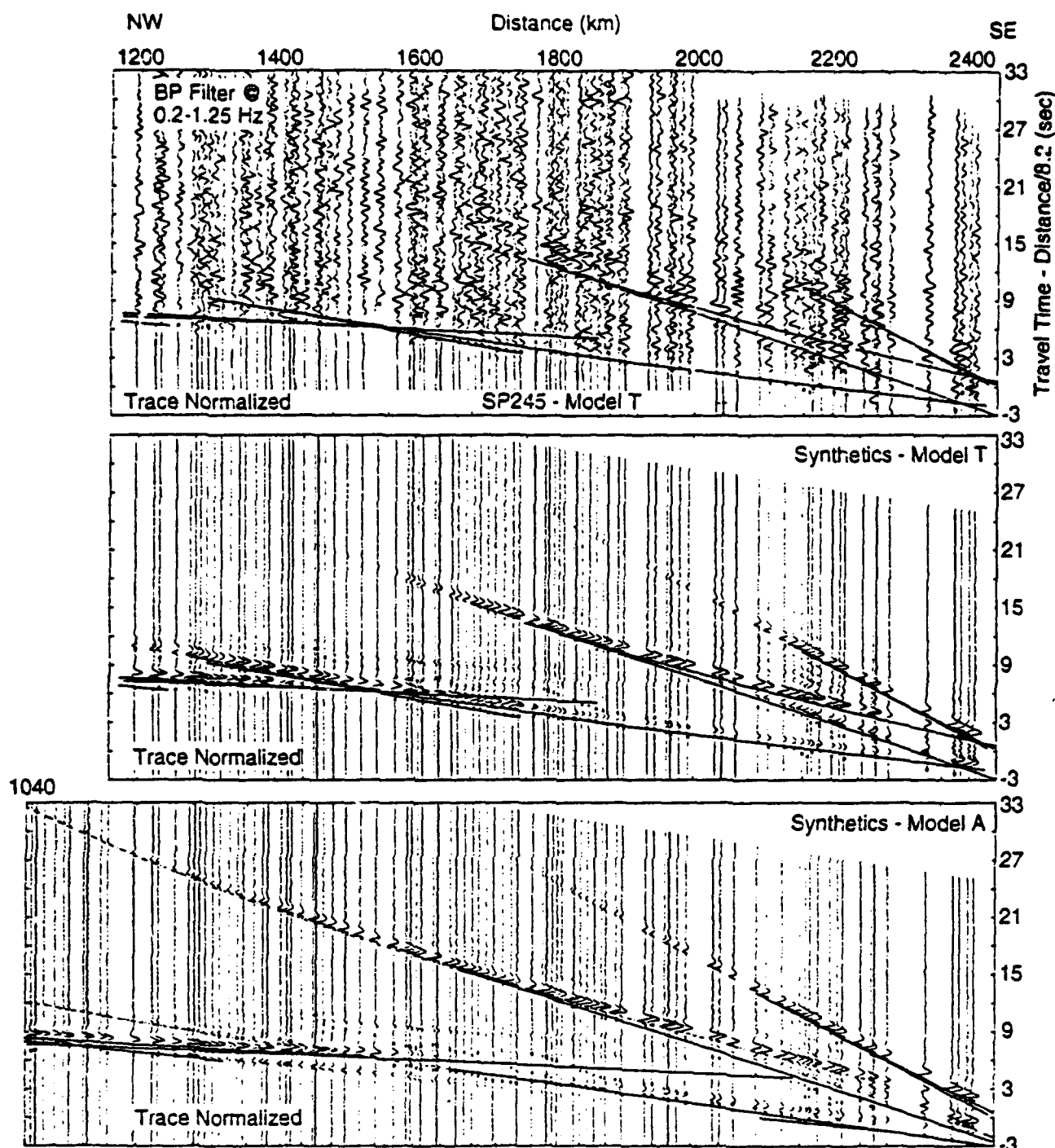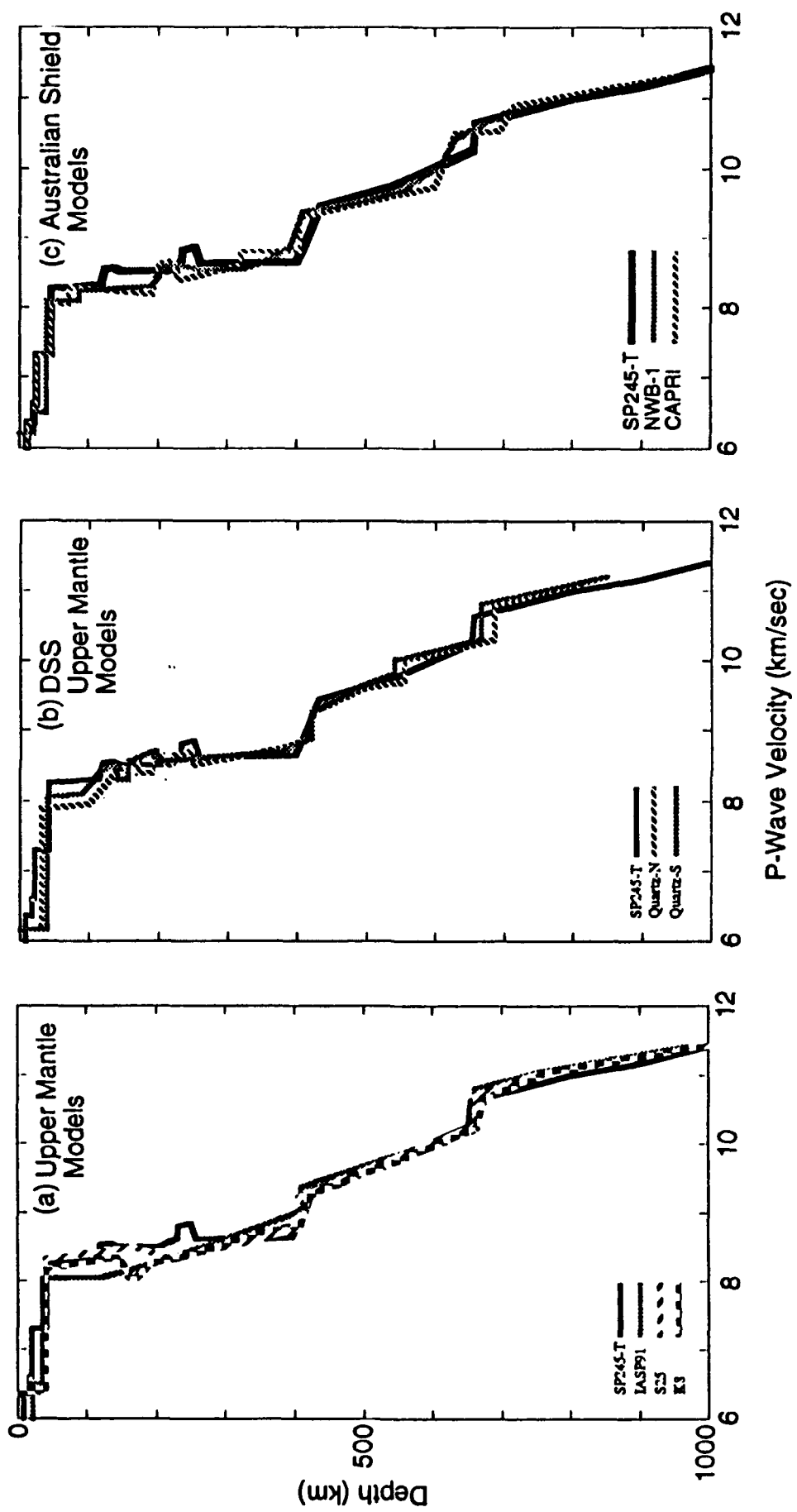
FIGURE 6

Prof. Thomas Ahrens
Seismological Lab, 252-21
Division of Geological & Planetary Sciences
California Institute of Technology
Pasadena, CA 91125

Prof. Keiiti Aki
Center for Earth Sciences
University of Southern California
University Park
Los Angeles, CA 90089-0741

Prof. Shelton Alexander
Geosciences Department
403 Deike Building
The Pennsylvania State University
University Park, PA 16802

Prof. Charles B. Archambeau
CIRES
University of Colorado
Boulder, CO 80309

Dr. Thomas C. Bache, Jr.
Science Applications Int'l Corp.
10260 Campus Point Drive
San Diego, CA 92121 (2 copies)

Prof. Muawia Barazangi
Institute for the Study of the Continent
Cornell University
Ithaca, NY 14853

Dr. Jeff Barker
Department of Geological Sciences
State University of New York
 at Binghamton
Vestal, NY 13901

Dr. Douglas R. Baumgardt
ENSCO, Inc
5400 Port Royal Road
Springfield, VA 22151-2388

Dr. Susan Beck
Department of Geosciences
Building #77
University of Arizona
Tuscon, AZ 85721

Dr. T.J. Bennett
S-CUBED
A Division of Maxwell Laboratories
11800 Sunrise Valley Drive, Suite 1212
Reston, VA 22091

Dr. Robert Blandford
AFTAC/TT, Center for Seismic Studies
1300 North 17th Street
Suite 1450
Arlington, VA 22209-2308

Dr. Stephen Bratt
ARPA/NMRO
3701 North Fairfax Drive
Arlington, VA 22203-1714

Dr. Lawrence Burdick
IGPP, A-025
Scripps Institute of Oceanography
University of California, San Diego
La Jolla, CA 92093

Dr. Robert Burridge
Schlumberger-Doll Research Center
Old Quarry Road
Ridgefield, CT 06877

Dr. Jerry Carter
Center for Seismic Studies
1300 North 17th Street
Suite 1450
Arlington, VA 22209-2308

Dr. Eric Chael
Division 9241
Sandia Laboratory
Albuquerque, NM 87185

Dr. Martin Chapman
Department of Geological Sciences
Virginia Polytechnical Institute
21044 Derring Hall
Blacksburg, VA 24061

Mr Robert Cockerham
Arms Control & Disarmament Agency
320 21st Street North West
Room 5741
Washington, DC 20451,

Prof. Vernon F. Cormier
Department of Geology & Geophysics
U-45, Room 207
University of Connecticut
Storrs, CT 06268

Prof. Steven Day
Department of Geological Sciences
San Diego State University
San Diego, CA 92182

1

Marvin Denny
U.S. Department of Energy
Office of Arms Control
Washington, DC 20585

Dr. Cliff Frolich
Institute of Geophysics
8701 North Mopac
Austin, TX 78759

Dr. Zoltan Der
ENSCO, Inc.
5400 Port Royal Road
Springfield, VA 22151-2388

Dr. Holly Given
IGPP, A-025
Scripps Institute of Oceanography
University of California, San Diego
La Jolla, CA 92093

Prof. Adam Dziewonski
Hoffman Laboratory, Harvard University
Dept. of Earth Atmos. & Planetary Sciences
20 Oxford Street
Cambridge, MA 02138

Dr. Jeffrey W. Given
SAIC
10260 Campus Point Drive
San Diego, CA 92121

Prof. John Ebel
Department of Geology & Geophysics
Boston College
Chestnut Hill, MA 02167

Dr. Dale Glover
Defense Intelligence Agency
ATTN: ODT-1B
Washington, DC 20301

Eric Fielding
SNEE Hall
INSTOC
Cornell University
Ithaca, NY 14853

Dan N. Hagedon
Pacific Northwest Laboratories
Battelle Boulevard
Richland, WA 99352

Dr. Petr Firbas
Institute of Physics of the Earth
Masaryk University Brno
Jecna 29a
612 46 Brno, Czech Republic

Dr. James Hannon
Lawrence Livermore National Laboratory
P.O. Box 808
L-205
Livermore, CA 94550

Dr. Mark D. Fisk
Mission Research Corporation
735 State Street
P.O. Drawer 719
Santa Barbara, CA 93102

Prof. David G. Harkrider
Seismological Laboratory
Division of Geological & Planetary Sciences
California Institute of Technology
Pasadena, CA 91125

Prof Stanley Flatte
Applied Sciences Building
University of California, Santa Cruz
Santa Cruz, CA 95064

Prof. Danny Harvey
CIRES
University of Colorado
Boulder, CO 80309

Prof. Donald Forsyth
Department of Geological Sciences
Brown University
Providence, RI 02912

Prof. Donald V. Helmberger
Seismological Laboratory
Division of Geological & Planetary Sciences
California Institute of Technology
Pasadena, CA 91125

Dr. Art Frankel
U.S. Geological Survey
922 National Center
Reston, VA 22092

Prof. Eugene Herrin
Institute for the Study of Earth and Man
Geophysical Laboratory
Southern Methodist University
Dallas, TX 75275

Prof. Robert B. Herrmann
Department of Earth & Atmospheric Sciences
St. Louis University
St. Louis, MO 63156

Jim Lawson, Chief Geophysicist
Oklahoma Geological Survey
Oklahoma Geophysical Observatory
P.O. Box 8
Leonard, OK 74043-0008

Prof. Lane R. Johnson
Seismographic Station
University of California
Berkeley, CA 94720

Prof. Thorne Lay
Institute of Tectonics
Earth Science Board
University of California, Santa Cruz
Santa Cruz, CA 95064

Prof. Thomas H. Jordan
Department of Earth, Atmospheric &
  Planetary Sciences
Massachusetts Institute of Technology
Cambridge, MA 02139

Dr. William Leith
U.S. Geological Survey
Mail Stop 928
Reston, VA 22092

Prof. Alan Kafka
Department of Geology & Geophysics
Boston College
Chestnut Hill, MA 02167

Mr. James F. Lewkowicz
Phillips Laboratory/GPEH
29 Randolph Road
Hanscom AFB, MA 01731-3010(2 copies)

Robert C. Kemerait
ENSCO, Inc.
445 Pineda Court
Melbourne, FL 32940

Mr. Alfred Lieberman
ACDA/VI-OA State Department Building
Room 5726
320-21st Street, NW
Washington, DC 20451

Dr. Karl Koch
Institute for the Study of Earth and Man
Geophysical Laboratory
Southern Methodist University
Dallas, Tx 75275

Prof. L. Timothy Long
School of Geophysical Sciences
Georgia Institute of Technology
Atlanta, GA 30332

Dr. Max Koontz
U.S. Dept. of Energy/DP 5
Forrestal Building
1000 Independence Avenue
Washington, DC 20585

Dr. Randolph Martin, III
New England Research, Inc.
76 Olcott Drive
White River Junction, VT 05001

Dr. Richard LaCoss
MIT Lincoln Laboratory, M-200B
P.O. Box 73
Lexington, MA 02173-0073

Dr. Robert Masse
Denver Federal Building
Box 25046, Mail Stop 967
Denver, CO 80225

Dr. Fred K. Lamb
University of Illinois at Urbana-Champaign
Department of Physics
1110 West Green Street
Urbana, IL 61801

Dr. Gary McCartor
Department of Physics
Southern Methodist University
Dallas, TX 75275

Prof. Charles A. Langston
Geosciences Department
403 Deike Building
The Pennsylvania State University
University Park, PA 16802

Prof. Thomas V. McEvilly
Seismographic Station
University of California
Berkeley, CA 94720

3

Dr. Art McGarr
U.S. Geological Survey
Mail Stop 977
U.S. Geological Survey
Menlo Park, CA 94025

Dr. Keith L. McLaughlin
S-CUBED
A Division of Maxwell Laboratory
P.O. Box 1620
La Jolla, CA 92038-1620

Stephen Miller & Dr. Alexander Florence
SRI International
333 Ravenswood Avenue
Box AF 116
Menlo Park, CA 94025-3493

Prof. Bernard Minster
IGPP, A-025
Scripps Institute of Oceanography
University of California, San Diego
La Jolla, CA 92093

Prof. Brian J. Mitchell
Department of Earth & Atmospheric Sciences
St. Louis University
St. Louis, MO 63156

Mr. Jack Murphy
S-CUBED
A Division of Maxwell Laboratory
11800 Sunrise Valley Drive, Suite 1212
Reston, VA 22091 (2 Copies)

Dr. Keith K. Nakanishi
Lawrence Livermore National Laboratory
L-025
P.O. Box 808
Livermore, CA 94550

Prof. John A. Orcutt
IGPP, A-025
Scripps Institute of Oceanography
University of California, San Diego
La Jolla, CA 92093

Prof. Jeffrey Park
Kline Geology Laboratory
P.O. Box 6666
New Haven, CT 06511-8130

Dr. Howard Patton
Lawrence Livermore National Laboratory
L-025
P.O. Box 808
Livermore, CA 94550

Dr. Frank Pilotte
HQ AFTAC/TT
1030 South Highway A1A
Patrick AFB, FL 32925-3002

Dr. Jay J. Pulli
Radix Systems, Inc.
201 Perry Parkway
Gaithersburg, MD 20877

Dr. Robert Reinke
ATTN: FCTVTD
Field Command
Defense Nuclear Agency
Kirtland AFB, NM 87115

Prof. Paul G. Richards
Lamont-Doherty Geological Observatory
of Columbia University
Palisades, NY 10964

Mr. Wilmer Rivers
Teledyne Geotech
314 Montgomery Street
Alexandria, VA 22314

Dr. Alan S. Ryall, Jr.
ARPA/NMRO
3701 North Fairfax Drive
Arlington, VA 22203-1714

Dr. Richard Sailor
TASC, Inc.
55 Walkers Brook Drive
Reading, MA 01867

Prof. Charles G. Sammis
Center for Earth Sciences
University of Southern California
University Park
Los Angeles, CA 90089-0741

Prof. Christopher H. Scholz
Lamont-Doherty Geological Observatory
of Columbia University
Palisades, NY 10964

Dr. Susan Schwartz
Institute of Tectonics
1156 High Street
Santa Cruz, CA 95064

Secretary of the Air Force
(SAFRD)
Washington, DC 20330

Office of the Secretary of Defense
DDR&E
Washington, DC 20330

Thomas J. Sereno, Jr.
Science Application Int'l Corp.
10260 Campus Point Drive
San Diego, CA 92121

Dr. Michael Shore
Defense Nuclear Agency/SPSS
6801 Telegraph Road
Alexandria, VA 22310

Dr. Robert Shumway
University of California Davis
Division of Statistics
Davis, CA 95616

Dr. Matthew Sibol
Virginia Tech
Seismological Observatory
4044 Derring Hall
Blacksburg, VA 24061-0420

Prof. David G. Simpson
IRIS, Inc.
1616 North Fort Myer Drive
Suite 1050
Arlington, VA 22209

Donald L. Springer
Lawrence Livermore National Laboratory
L-025
P.O. Box 808
Livermore, CA 94550

Dr. Jeffrey Stevens
S-CUBED
A Division of Maxwell Laboratory
P.O. Box 1620
La Jolla, CA 92038-1620

Lt. Col. Jim Stobie
ATTN: AFOSR/NL
110 Duncan Avenue
Bolling AFB
Washington, DC 20332-0001

Prof. Brian Stump
Institute for the Study of Earth & Man
Geophysical Laboratory
Southern Methodist University
Dallas, TX 75275

Prof. Jeremiah Sullivan
University of Illinois at Urbana-Champaign
Department of Physics
1110 West Green Street
Urbana, IL 61801

Prof. L. Sykes
Lamont-Doherty Geological Observatory
 of Columbia University
Palisades, NY 10964

Dr. David Taylor
ENSCO, Inc.
445 Pineda Court
Melbourne, FL 32940

Dr. Steven R. Taylor
Los Alamos National Laboratory
P.O. Box 1663
Mail Stop C335
Los Alamos, NM 87545

Prof. Clifford Thurber
University of Wisconsin-Madison
Department of Geology & Geophysics
1215 West Dayton Street
Madison, WS 53706

Prof. M. Nafi Toksoz
Earth Resources Lab
Massachusetts Institute of Technology
42 Carleton Street
Cambridge, MA 02142

Dr. Larry Turnbull
CIA-OSWR/NED
Washington, DC 20505

Dr. Gregory van der Vink
IRIS, Inc.
1616 North Fort Myer Drive
Suite 1050
Arlington, VA 22209

Dr. Karl Veith
EG&G
5211 Auth Road
Suite 240
Suitland, MD 20746

Prof. Terry C. Wallace
Department of Geosciences
Building #77
University of Arizona
Tuscon, AZ 85721

Phillips Laboratory
ATTN: XPG
29 Randolph Road
Hanscom AFB, MA 01731-3010

Dr. Thomas Weaver
Los Alamos National Laboratory
P.O. Box 1663
Mail Stop C335
Los Alamos, NM 87545

Phillips Laboratory
ATTN: GPE
29 Randolph Road
Hanscom AFB, MA 01731-3010

Dr. William Wortman
Mission Research Corporation
8560 Cinderbed Road
Suite 700
Newington, VA 22122

Phillips Laboratory
ATTN: TSML
5 Wright Street
Hanscom AFB, MA 01731-3004

Prof. Francis T. Wu
Department of Geological Sciences
State University of New York
 at Binghamton
Vestal, NY 13901

Phillips Laboratory
ATTN: PL/SUL
3550 Aberdeen Ave SE
Kirtland, NM 87117-5776 (2 copies)

Prof Ru-Shan Wu
University of California, Santa Cruz
Earth Sciences Department
Santa Cruz
, CA 95064

Dr. Michel Bouchon
I.R.I.G.M.-B.P. 68
38402 St. Martin D'Heres
Cedex, FRANCE

ARPA, OASB/Library
3701 North Fairfax Drive
Arlington, VA 22203-1714

Dr. Michel Campillo
Observatoire de Grenoble
I.R.I.G.M.-B.P. 53
38041 Grenoble, FRANCE

HQ DNA
ATTN: Technical Library
Washington, DC 20305

Dr. Kin Yip Chun
Geophysics Division
Physics Department
University of Toronto
Ontario, CANADA

Defense Intelligence Agency
Directorate for Scientific & Technical Intelligence
ATTN: DTIB
Washington, DC 20340-6158

Prof. Hans-Peter Harjes
Institute for Geophysic
Ruhr University/Bochum
P.O. Box 102148
4630 Bochum 1, GERMANY

Defense Technical Information Center
Cameron Station
Alexandria, VA 22314 (2 Copies)

Prof. Eystein Husebye
NTNF/NORSAR
P.O. Box 51
N-2007 Kjeller, NORWAY

TACTEC
Battelle Memorial Institute
505 King Avenue
Columbus, OH 43201 (Final Report)

6

David Jepsen
Acting Head, Nuclear Monitoring Section
Bureau of Mineral Resources
Geology and Geophysics
G.P.O. Box 378, Canberra, AUSTRALIA

Ms. Eva Johannisson
Senior Research Officer
FOA
S-172 90 Sundbyberg, SWEDEN

Dr. Peter Marshall
Procurement Executive
Ministry of Defense
Blacknest, Brimpton
Reading FG7-FRS, UNITED KINGDOM

Dr. Bernard Massinon, Dr. Pierre Mechler
Societe Radiomana
27 rue Claude Bernard
75005 Paris, FRANCE (2 Copies)

Dr. Svein Mykkeltveit
NTNT/NORSAR
P.O. Box 51
N-2007 Kjeller, NORWAY (3 Copies)

Prof. Keith Priestley
University of Cambridge
Bullard Labs, Dept. of Earth Sciences
Madingley Rise, Madingley Road
Cambridge CB3 OEZ, ENGLAND

Dr. Jorg Schlittenhardt
Federal Institute for Geosciences & Nat'l Res.
Postfach 510153
D-30631 Hannover , GERMANY

Dr. Johannes Schweitzer
Institute of Geophysics
Ruhr University/Bochum
P.O. Box 1102148
4360 Bochum 1, GERMANY

Trust & Verify
VERTIC
Carrara House
20 Embankment Place
London WC2N 6NN, ENGLAND